Title

Electrochemical Microenvironments Enable Low-Overpotential CO_2 Reduction

ISBN

9798189276125

Author

Shan, Yu

Publication Date

2026-05-01

Peer reviewed|Thesis/dissertation

Electrochemical Microenvironments Enable Low-Overpotential CO_2 Reduction

By

Yu Shan

A dissertation submitted in partial satisfaction of the

requirements for the degree of

Doctor of Philosophy

in

Engineering– Materials Science and Engineering

in the

Graduate Division

of the

University of California, Berkeley

Committee in charge:

Professor Peidong Yang, Chair

Professor Bryan Mccloskey

Professor Junqiao Wu

Spring 2026

Abstract

Electrochemical Microenvironments Enable Low-Overpotential CO_2 Reduction

by

Yu Shan

Doctor of Philosophy in Engineering – Materials Science and Engineering

University of California, Berkeley

Professor Peidong Yang, Chair

The electrochemical reduction of carbon dioxide (CO_2R) offers a promising route for converting renewable electricity into carbon-neutral fuels and chemical feedstocks. However, most CO_2 reduction reactions require large overpotentials, limiting energy efficiency and hindering integration with renewable energy systems. While significant efforts have focused on engineering catalyst surfaces to improve activity and selectivity at low overpotentials, increasing evidence suggests that the electrochemical microenvironment at the catalyst–electrolyte interface plays an equally critical role in governing reaction energetics and intermediate stabilization. Understanding how ions, solvent molecules, and adsorbates interact within this dynamic interfacial region is therefore essential for developing efficient electrocatalytic systems.

This dissertation investigates how electrochemical microenvironments influence CO_2 reduction using a combination of *in situ* vibrational and electronic spectroscopy. Two representative catalytic systems are examined to elucidate distinct mechanisms through which microenvironmental effects regulate catalytic activity.

The first part of this work focuses on nanoparticle-ordered ligand interlayer (NOLI) catalysts, which exhibit unusually low overpotentials for CO_2 reduction. Using *in situ* nano-FTIR spectroscopy, ligand dynamics during electrochemical operation are directly visualized with nanometer spatial resolution, revealing that ligand detachment and nanoparticle coarsening lead to the formation of a confined interfacial architecture. Within this ligand-defined pocket, *in situ* SEIRAS and total electron yield X-ray absorption spectroscopy show that electrolyte cations undergo partial desolvation and stabilize intermediates through partial covalent interaction. These observations support a mechanistic model in which ligand-modulated cation desolvation facilitates cation-coupled electron transfer, thereby lowering the activation barrier for CO_2 activation and enabling low-overpotential CO_2 reduction.

The second part of this dissertation investigates the electrochemical microenvironment of copper catalysts, which uniquely produce multi-carbon products during CO_2 reduction. *In situ* nano-FTIR measurements reveal nanoscale heterogeneity in ion distributions and interfacial water structures near evolving Cu surfaces. Complementary SERS and SEIRAS measurements on Cu nanograin

catalysts show that carbonate-derived species, oxygen-containing co-adsorbates, and CO intermediates coexist at the catalytic interface. The spectral evolution of CO adsorption further indicates that dipole–dipole interactions, adsorbate coverage, and local electric fields collectively influence the stability and vibrational signatures of intermediates. These findings demonstrate that CO_2 reduction on Cu occurs within a dynamically evolving interfacial environment shaped by electrolyte species, catalyst morphology, and adsorbate interactions.

Together, these studies establish the electrochemical microenvironment as a key determinant of catalytic behavior in CO_2 reduction. By revealing how confined interfacial structures, ion solvation, and adsorbate interactions influence reaction energetics, this thesis provides new mechanistic insight into the role of electrolyte–surface interactions in electrocatalysis. More broadly, the concepts and experimental approaches developed here offer a framework for engineering interfacial microenvironments to enable low-overpotential electrochemical reactions, advancing the design of efficient catalysts for sustainable energy conversion.

Dedicated to my family, for their love and support.

Table of Contents

Acknowledgement

First and foremost, I would like to express my deepest gratitude to Professor Peidong Yang for his guidance, mentorship, and unwavering support throughout my PhD journey. When I joined his group, I had only a limited background in electrochemistry. Under his mentorship, however, I was trained to become a capable scientific researcher and materials scientist, and I learned to approach scientific questions with rigor and curiosity. In his group, I was taught to uphold high standards of academic integrity and research safety, to think critically about scientific problems, and to identify questions that are both fundamentally important and worth pursuing. Perhaps most importantly, he showed me how to elevate experimental observations into generalizable scientific insights. I am deeply grateful for the safe, professional, and inspiring research environment he created, as well as for the resources and opportunities that allowed me to grow as a scientist and broaden my perspective throughout my PhD. I also sincerely appreciate the many conversations we had about my career development and life beyond research. Working under a mentor like Professor Yang has been a privilege, and this experience will remain one of the most meaningful parts of my academic journey.

I would also like to thank my early mentors in the group—Prof. Sunmoon Yu, Dr. Shouping Chen, and Dr. Xiao Zhao—who helped me get started when I first joined the lab and guided me through the initial stages of my research. Their patience, advice, and willingness to share their experience were invaluable in helping me transition into a new research field. I am also grateful to Professor Yao Yang, whose diligence and enthusiasm in science set an excellent example during my first three years in the group.

My sincere thanks also go to my cohort and colleagues who shared this journey with me: Maria Fonseca Guzman, Julian Feijóo, Nathan Soland, Arifin Luthfi Maulana, Yuxin Jiang, and Libby Lineberry. I am grateful for the discussions, collaborations, and the many moments we experienced together along the way. I would also like to thank several Yang Group alumni and colleagues, including Dr. Cheng Zhu, Dr. Jianbo Jin, Dr. Inwhan Roh, Dr. Chubai Chen, Dr. Jia-An Lin, and Prof. Sheena Louisia and Prof. Jie Luo, for their friendship, scientific discussions, and support during different stages of my PhD. These interactions made the research environment both stimulating and enjoyable.

I am especially thankful to my mentees, Alex Sachelarie and Tianle Wang, for their enthusiasm, hard work, and contributions. Mentoring them has been a rewarding experience, and I wish them all the best in the continuation of their studies and research. I would also like to thank Lissette Garcia and Crystal Garcia for their invaluable administrative support, which helped keep many aspects of our research activities running smoothly.

Many of the projects presented in this dissertation would not have been possible without the help of outstanding collaborators and facility staff. I would like to express my sincere gratitude to Prof. Miquel Salmeron, Prof. Philippe Sautet, Dr. Hans Bechtel, Dr. Stephanie Gilbert Corder, Dr. Jinghua Guo, Dr. Maximillian Jaugstetter, Dr. Evan Carlson, Dr. Helen Zeng, Dr. Jin Qian, Dr. Yani Guan, Dr. Asmita Jana, Dr. Honghe Ding, Dr. Jialu Li, Dr. Virginia Altoe, Dr. Ka Chon Ng,

Dr. Cooper Citek, and Lihini Jayasinghe. Their expertise, professionalism, and willingness to collaborate played a crucial role in advancing all of my projects. I am also deeply grateful for the opportunity to conduct experiments at world-class research facilities, including the Advanced Light Source (ALS), the Molecular Foundry, and Diamond Light Source. Access to these facilities enabled many of the experiments that made this research possible.

I would also like to acknowledge the financial support that made my PhD studies possible. My research funding was supported by the U.S. Department of Energy. I am also grateful for the fellowship from the University of Chinese Academy of Sciences and the fellowship from Department of Materials Science and Engineering at UC Berkeley, the Kavli Energy Nanoscience Fellowship, and the H_2H_8 Fellowship, all of which provided valuable support during my graduate studies.

Finally, I would like to thank my family and loved ones. My deepest gratitude goes to my girlfriend, Yuye Zhou, who has accompanied me through most of my PhD journey and shared with me both the challenges and joys of graduate school and life. This journey would have been far less meaningful and memorable without her support and companionship. I am also profoundly grateful to my mother, father, and grandparents, whose love and unconditional support have guided me throughout my life. Although some of them are no longer with us, their encouragement and belief in me made it possible for me to pursue this path and ultimately complete this PhD.

Chapter 1 Introduction

1.1 CO_2 emissions and motivation for CO_2 conversion

The rapid increase of atmospheric carbon dioxide (CO_2) is widely recognized as one of the most pressing environmental challenges of the twenty-first century. Since the beginning of the industrial revolution, large-scale combustion of fossil fuels for electricity generation, transportation, and industrial production has dramatically increased anthropogenic CO_2 emissions. Global fossil CO_2 emissions now exceed 37 gigatons per year[1,2], contributing to a steady rise in atmospheric CO_2 concentration to levels unprecedented in modern human history. The accumulation of greenhouse gases in the atmosphere enhances radiative forcing and is widely considered the primary driver of global climate change, leading to rising global temperatures, ocean acidification, and increasingly frequent extreme weather events[3]. Addressing the growth of atmospheric CO_2 has therefore become a central objective for both scientific research and international climate policy.

In response to these challenges, many countries and industries have adopted strategies aimed at achieving carbon neutrality, in which net carbon emissions are reduced to zero by balancing emissions with carbon removal or recycling processes. While significant progress is being made toward decarbonizing energy systems through renewable electricity generation, eliminating carbon emissions entirely remains difficult because modern economies rely heavily on carbon-based fuels and chemical feedstocks. As a result, increasing attention has been directed toward carbon capture and utilization (CCU) strategies that transform CO_2 from a waste product into a useful carbon resource[4,5]. By treating CO_2 as a recyclable feedstock, CCU approaches aim to partially close the anthropogenic carbon cycle while reducing the environmental burden associated with carbon emissions.

Transforming CO_2 into value-added chemicals and fuels is particularly attractive because it simultaneously addresses both environmental and energy challenges[4,5]. Carbon-based products such as carbon monoxide, hydrocarbons, and alcohols serve as essential building blocks for the chemical industry and global energy infrastructure[6]. Conventional production of these molecules relies primarily on fossil resources, resulting in additional carbon emissions. In contrast, converting captured CO_2 into these products provides a pathway for producing chemicals and fuels while recycling existing carbon rather than extracting new fossil carbon from the Earth. Moreover, many of these chemical transformations store significant amounts of energy in chemical bonds, allowing CO_2-derived fuels and chemicals to function as energy carriers. This capability offers a potential route for storing intermittent renewable energy in chemical form, thereby enabling long-term energy storage, and facilitating deeper integration of renewable power sources such as solar and wind.

Among the various technologies proposed for CO_2 utilization, electrochemical CO_2 reduction (CO_2R) has emerged as a particularly promising strategy. In electrochemical systems, electrical energy can be used to drive catalytic reactions at electrode surfaces that convert CO_2 into a range of chemical products. When powered by renewable electricity, electrochemical CO_2 conversion provides a direct route for coupling carbon recycling with sustainable energy generation, as shown in Figure 1.1. These features have stimulated extensive research into electrocatalysts, reaction

mechanisms, and system designs capable of enabling efficient CO_2 electroreduction. The following section introduces the fundamental principles and key metrics of electrochemical CO_2 reduction.

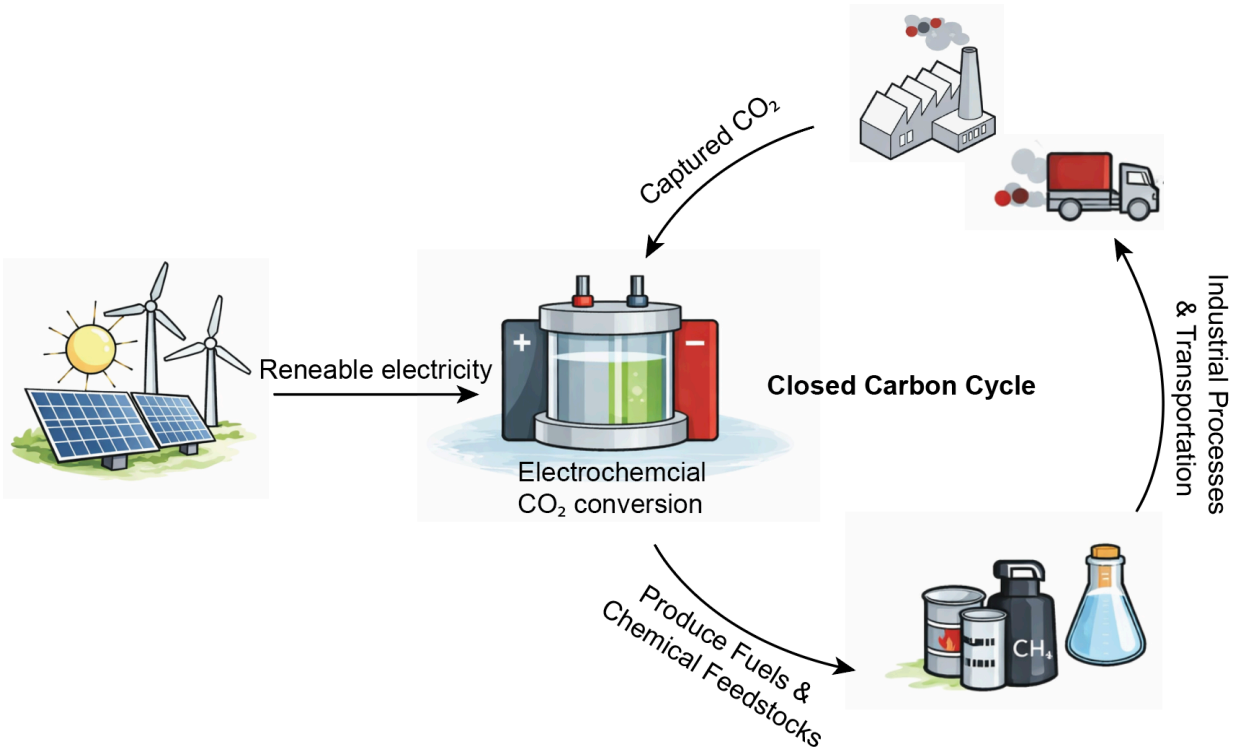

Figure 1.1. Electrochemical CO_2 reduction as a pathway toward a closed carbon cycle. Renewable electricity generated from sources such as solar and wind power can drive electrochemical reactions that convert captured carbon dioxide into fuels and chemical feedstocks. These carbon-based products can be used in industrial processes or transportation systems, where their utilization ultimately produces CO_2 emissions. By capturing and recycling this emitted CO_2 as the input for electrochemical conversion, a closed carbon cycle can be established, enabling the sustainable production of fuels and chemicals while reducing reliance on fossil carbon resources.

1.2 Fundamentals of CO_2 electroreduction

Electrochemical CO_2 reduction (CO_2R) converts carbon dioxide into reduced carbon products through electrochemical reactions occurring at the electrode–electrolyte interface[6,7]. In a typical CO_2R electrolyzer, as illustrated in Figure 1.2, CO_2 is supplied to the cathode, where it undergoes reduction via a series of proton and electron transfer steps that transform the thermodynamically stable CO_2 molecule into reduced products with higher energy content. The reaction can be expressed in a general form as

$$xCO_2 + nH^+ + ne^- \rightarrow \text{product} + yH_2O \quad (1)$$

To maintain charge balance within the electrochemical system, a complementary oxidation reaction—most commonly the oxygen evolution reaction (OER) involving water oxidation—occurs at the anode (Figure 1.2).

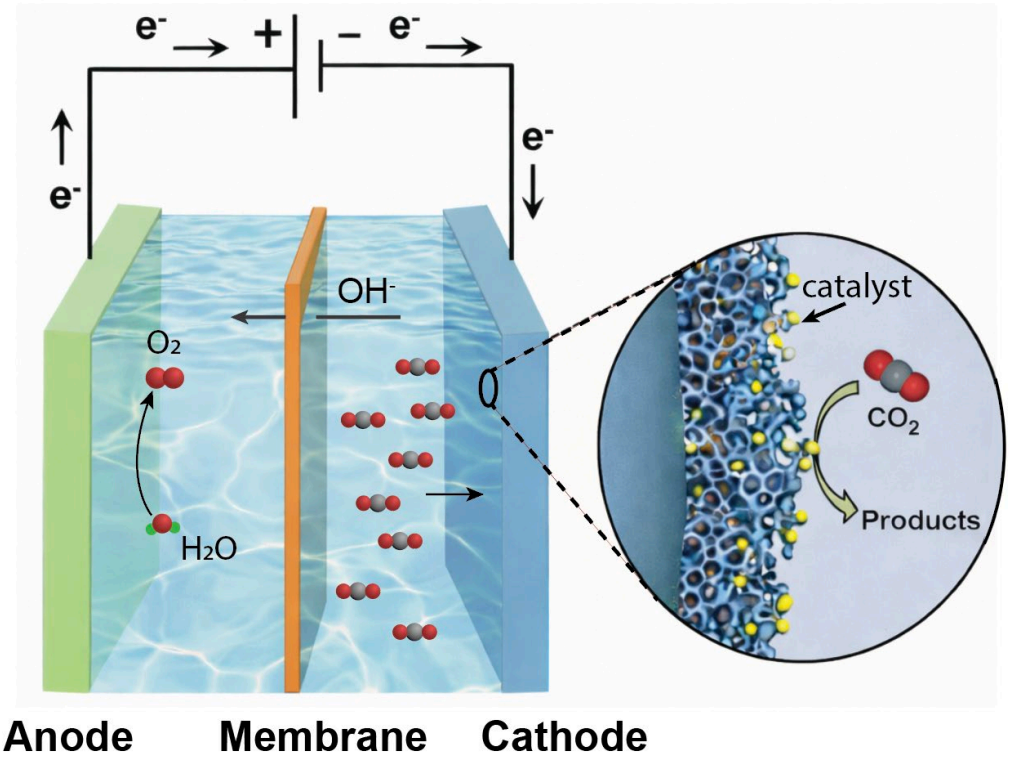

Figure 1.2. Schematic illustration of an H-type CO_2 electrolysis cell. A typical electrochemical CO_2 reduction system consists of two compartments separated by an anion exchange membrane. At the cathode, dissolved CO_2 molecules are reduced on the catalyst surface to form carbon-based products through multi-electron and proton-coupled reactions. Simultaneously, water oxidation occurs at the anode, producing O_2 to maintain charge balance in the cell. Electrons flow through the external circuit from the anode to the cathode, while ionic species are transported across the membrane to complete the electrochemical circuit.

Depending on the catalyst material and reaction conditions, CO_2R can produce a wide range of chemicals and fuels, making it an attractive strategy for transforming waste carbon into valuable commodities[8]. Table 1.1 summarizes the thermodynamic equilibrium potentials, industrial relevance, and approximate market prices of several commonly reported CO_2R products. Approximate market prices were compiled from published techno-economic analyses of CO_2 electrolysis systems and industrial chemical databases[8-10]. These values are intended to illustrate the relative economic value of different CO_2R products rather than precise market quotations. Two-electron products such as carbon monoxide (CO) and formate are among the most readily produced species and serve as important platform chemicals. CO is a key component of syngas and is widely used in Fischer–Tropsch synthesis and methanol production[7], whereas formate and formic acid are

widely used in chemical manufacturing and have also been proposed as potential liquid hydrogen carriers[11]. More deeply reduced products, including methane and methanol, possess high energy density and can function directly as fuels or fuel intermediates[11]. Multi-carbon (C_2+) products such as ethylene, ethanol, and propanol are particularly attractive targets due to their higher economic value and large global markets[8,12]. For instance, ethylene is one of the most widely produced chemicals worldwide and serves as a primary feedstock for polyethylene and other polymer materials[10].

Table 1.1 Thermodynamics and industrial relevance of major CO_2R products

Reaction	E^0 (V vs. RHE)	Market relevance	Market price (USD/ kg)
$CO_2 + 2H^+ + 2e^- \rightarrow CO + H_2O$	-0.11	Syngas, Fischer–Tropsch feedstock	0.6-1
$CO_2 + 2H^+ + 2e^- \rightarrow HCOOH$ (aq.)	-0.20	Chemical feedstock, hydrogen carrier	0.6-1.2
$CO_2 + 8H^+ + 8e^- \rightarrow CH_4 + 2H_2O$	0.17	Fuel, natural gas substitute	0.2-0.4
$CO_2 + 6H^+ + 6e^- \rightarrow CH_3OH + H_2O$	0.03	Fuel, solvent, chemical feedstock	0.4-0.6
$2CO_2 + 12H^+ + 12e^- \rightarrow C_2H_4 + 4H_2O$	0.08	Polymer precursor (polyethylene)	1-1.3
$2CO_2 + 12H^+ + 12e^- \rightarrow C_2H_5OH + 3H_2O$	0.09	Fuel additive, solvents	0.8-1.2
$2CO_2 + 8H^+ + 8e^- \rightarrow CH_3COOH + 2H_2O$	0.11	Chemical feedstock (vinyl acetate, solvents)	0.6-0.9
$3CO_2 + 18H^+ + 18e^- \rightarrow C_3H_7OH + 5H_2O$	0.10	Solvent, specialty chemicals	1.5-2.5
$2CO_2 + 10H^+ + 10e^- \rightarrow CH_3CHO + 3H_2O$	0.17	Chemical intermediate	1.2-1.8

Despite the diversity of possible products, practical CO_2R systems are typically evaluated using several key performance metrics. The first is **activity**, commonly quantified by the current density associated with CO_2 reduction products. In particular, the specific current density normalized to the electrochemically active surface area (ECSA) reflects the intrinsic catalytic capability for

converting CO_2 into a given product. Higher current densities correspond to faster reaction rates and are essential for achieving industrially relevant production rates. The second important metric is **selectivity**, typically expressed as the faradaic efficiency (FE) for a specific product, which represents the fraction of electrons contributing to the formation of that product relative to all electrochemical reactions occurring at the electrode. Selectivity is influenced not only by the competing hydrogen evolution reaction (HER), which occurs simultaneously at the cathode, but also by competing CO_2R pathways leading to different products. High selectivity is desirable because it minimizes the need for additional, often energy-intensive, product separation processes. A third important performance metric is **stability**, which refers to the ability of the catalyst to maintain its activity and selectivity over extended operation times. Improved stability reduces catalyst replacement frequency, maintenance costs, and operational downtime, and therefore plays a critical role in enabling the practical scale-up of CO_2 electrolysis technologies. Finally, **energy efficiency**, defined as the ratio between the energy stored in the desired product and the total electrical energy input required for its formation[8,12], represents a key parameter determining the overall viability of CO_2 electrolysis systems. Higher energy efficiencies correspond to smaller energy penalties for producing chemical products from CO_2.

Together, these metrics define the primary performance targets for CO_2 electroreduction catalysts: high activity, high selectivity toward valuable products, long operational stability, and high energy efficiency. These performance parameters are strongly influenced by the applied electrochemical potential, which governs reaction kinetics, catalytic pathways, and the interfacial electrochemical environment. Achieving these goals therefore requires a detailed understanding of how the applied potential modulates reaction mechanisms, catalyst structures, and the local electrochemical microenvironment at the catalyst surface.

1.3 Overpotential and catalytic efficiency

As shown in Table 1.1, the thermodynamic potentials of many CO_2 reduction reactions lie relatively close to that of the hydrogen evolution reaction (HER), which occurs at 0 V versus the reversible hydrogen electrode (RHE). At first glance, this proximity may suggest that CO_2 reduction should occur as readily as HER. In practice, however, CO_2 electroreduction typically requires significantly more negative applied potentials to achieve appreciable reaction rates. The difference between the applied potential and the thermodynamic equilibrium potential is defined as the **overpotential (η)**.

Overpotential represents the additional energy required to overcome kinetic barriers associated with electrochemical reactions. In the case of CO_2 reduction, these barriers arise from several factors, including the activation of the linear and chemically stable CO_2 molecule, the formation and transformation of surface-bound intermediates, and competition with parallel reactions such as HER. Consequently, the magnitude of the overpotential required for a given reaction provides an important indicator of catalytic efficiency.

From the perspective of classical Gouy-Chapman-Stern (GCS) theory, the driving force for interfacial charge transfer originates from the electric field within the electrical double layer (EDL),

particularly across the Stern layer[13,14] (Figure 1.3). The interfacial electric field within the Stern layer can be expressed as

$$\varepsilon = \frac{E_M - E_{OHL}}{d_H} = \frac{\mu + E^0 - E_{OHL}}{d_H} \quad (2)$$

Where E_M is the applied potential of the metal electrode, while E_{OHL} is potential of outer Helmholtz layer (OHL). E^0 is thermodynamical equilibrium potential. d_H is the thickness of Helmholtz layer, which typically has a thickness of less than one nanometer under aqueous electrochemical conditions. From Eq. 2, one can easily conclude that the applied overpotential largely determines the magnitude of the interfacial electric field and thus the driving force for electrochemical charge-transfer reactions.

Because of its direct influence on interfacial charge transfer, overpotential strongly affects the key catalytic performance metrics introduced in Section 1.2. In general, increasing the applied potential increases the reaction driving force, which leads to higher reaction rates and higher current densities when the system is not limited by mass transport. At the same time, the applied potential can significantly influence product selectivity. In CO_2 electroreduction, a certain minimum overpotential is required to activate the chemically stable CO_2 molecule. If the applied overpotential is too small, the competing hydrogen evolution reaction tends to dominate due to its lower kinetic barrier. In addition, as the overpotential increases, the adsorption energies and surface coverages of reaction intermediates can change, thereby altering reaction pathways and product distributions. For example, at relatively low overpotentials, CO binding on many catalysts is weak, favoring rapid desorption of CO and resulting in high Faradaic efficiency (FE) toward CO formation. At higher overpotentials, stronger CO adsorption can increase the lifetime of adsorbed CO intermediates, facilitating C–C coupling processes and enabling the formation of multi-carbon (C_{2+}) products on catalysts such as copper[6].

Besides activity and selectivity, notably, overpotential also plays a critical role in determining the energy efficiency (EE) of electrochemical CO_2 conversion systems, which, by definition, can be expressed as

$$EE = \frac{E^0 \cdot FE(\eta)}{E^0 + \eta} \quad (3)$$

Where E^0 is the thermodynamic equilibrium potential of the desired product-forming reaction, *FE* is the Faradaic efficiency toward that product, and η is the total applied cell overpotential (the combination of overpotential on both the anode and cathode). This expression highlights the trade-off between catalytic activity and energy input: although higher overpotentials often increase reaction rates, they simultaneously increase the electrical energy required to drive the reaction.

A comparison between electrochemical CO_2 conversion and traditional thermochemical routes further illustrates the pivotal role of overpotential in electrochemical CO_2R. Conventional thermochemical processes such as the reverse water–gas shift (RWGS) reaction and methanol synthesis typically achieve energy efficiencies exceeding 60%[5,8]. In contrast, the energy efficiency of most current electrochemical CO_2 reduction systems remain below 50%[6,9]. To make electrochemical CO_2 reduction competitive with traditional thermochemical routes, it is therefore necessary to minimize the energy losses associated with the reaction. While improvements in reactor design and cell engineering can partially mitigate energy losses, achieving high energy

efficiency ultimately requires catalysts capable of delivering high activity and selectivity at low overpotentials.

Another important motivation for minimizing overpotential is the potential integration of CO_2 electroreduction with photo-driven energy conversion systems. In photoelectrochemical (PEC) or photovoltaic-assisted electrochemical systems, the available photovoltage generated by semiconductor absorbers is fundamentally limited by the material bandgap and device architecture. Typical single-absorber photoelectrodes generate photovoltages on the order of several hundred millivolts to one volt[15,16]. If the electrochemical reaction requires a large overpotential, the photovoltage produced by the light absorber may be insufficient to drive the reaction efficiently. Therefore, catalysts that operate at low overpotential are essential for enabling CO_2 reduction to proceed using the limited photovoltage available from semiconductor photoelectrodes, thereby improving the feasibility of integrated solar-to-fuel systems.

In summary, overpotential is a central parameter governing the performance of electrochemical CO_2 reduction systems. It determines the driving force for interfacial charge transfer, strongly influences reaction rates and product selectivity, and directly impacts the overall energy efficiency of the electrochemical process. Furthermore, minimizing overpotential is essential for enabling the integration of CO_2 electroreduction with photo-driven energy conversion technologies. Consequently, the development of catalysts capable of converting CO_2 at high reaction rates and high FE while operating at low overpotential remains a critical objective in the field of electrochemical CO_2 conversion.

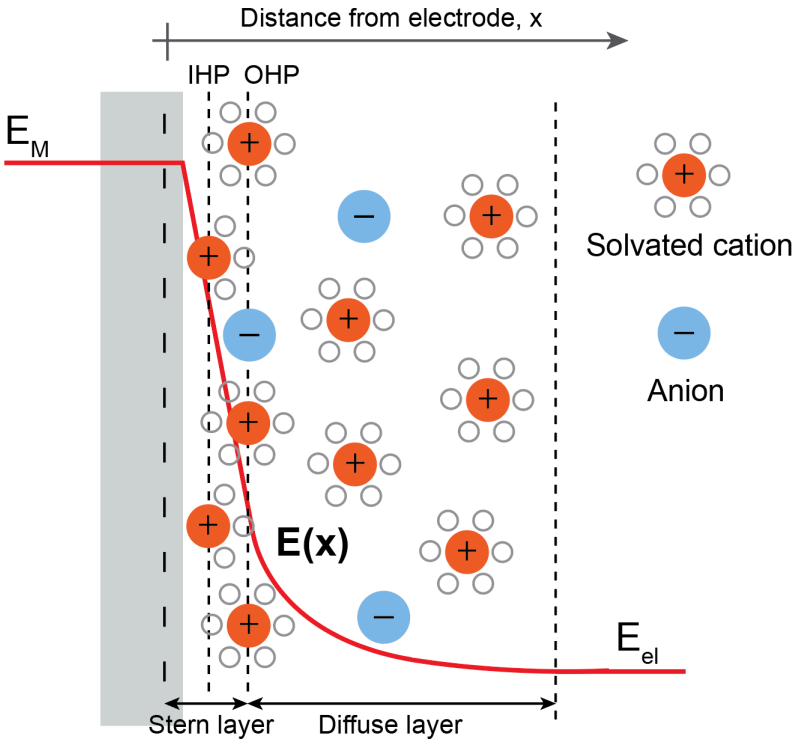

Figure 1.3. Schematic illustration of the electrical double layer (EDL) at an electrochemical interface. The EDL consists of the compact Stern layer and the diffuse layer. The majority of the electrostatic potential drop occurs across the Stern layer, which typically has a thickness of less than one nanometer. The applied overpotential largely determines the electric field within this

region, which drives interfacial charge-transfer reactions during electrochemical processes such as CO_2 reduction.

1.4 Strategies for lowering overpotential in CO_2R

Section 1.3 highlighted the central role of overpotential in determining catalytic activity, selectivity, and overall energy efficiency in electrochemical CO_2 reduction. Although higher applied potentials can increase reaction rates, the large overpotentials typically required to drive CO_2R at industrially relevant rates significantly limit the energy efficiency of the process and hinder its compatibility with photo-driven energy conversion systems. Consequently, a major objective in CO_2 electrocatalysis is the development of catalysts capable of achieving high activity and selectivity at substantially reduced overpotentials.

To address this challenge, the electrocatalysis community has developed a diverse set of catalyst design strategies aimed at lowering the kinetic barriers associated with CO_2 activation and intermediate transformations. At the atomic level, an effective CO_2R catalyst must stabilize key reaction intermediates while simultaneously suppressing competing reactions such as the hydrogen evolution reaction (HER). Many of these approaches rely on tuning the geometric and electronic structure of catalytic active sites to optimize the adsorption energetics of intermediates involved in CO_2 reduction pathways.

This section summarizes several major catalyst design principles that have been widely explored to improve CO_2R performance. Specifically, we focus on facet engineering, strain engineering, and defect engineering, which aim to modify the local atomic configuration and electronic structure of catalytic surfaces. These strategies seek to regulate intermediate binding energies and facilitate key steps such as CO_2 activation and C–C coupling. Importantly, this discussion focuses on the intrinsic structural properties of catalysts, whereas modifications to the electrochemical microenvironment will be discussed separately in Section 1.5 to distinguish catalyst design from interfacial environment engineering.

The development of CO_2R catalysts has evolved significantly from the early classification of metals according to their primary reaction products. Pioneering studies by Hori and co-workers categorized metals into several groups based on their selectivity: CO-producing metals (e.g., Au, Ag, Zn), formate-producing metals (e.g., Sn, Bi, Pb, In), and copper, which uniquely enables the formation of deeply reduced hydrocarbons and oxygenates[6]. However, achieving high selectivity and activity at low overpotentials requires moving beyond these simple groupings.

A central challenge in catalyst optimization arises from the presence of scaling relationships that link the adsorption energies of key reaction intermediates[17]. For many transition-metal catalysts, the binding energies of intermediates such as *COOH and *CO are linearly correlated, meaning that stabilizing one intermediate often leads to the over-stabilization of another. This coupling creates intrinsic limits in catalytic performance, often described as “volcano relationships”[18]. To overcome these limitations, researchers employ geometric and electronic tuning strategies designed to partially decouple intermediate adsorption energies and thereby improve catalytic

activity at lower overpotentials. These approaches can be broadly categorized based on the nature of the structural or electronic modification, as summarized in Table 1.2.

Table 1.2 Catalyst design strategies for lowering overpotential in electrochemical CO_2 reduction through geometric and electronic tuning

Design Strategy	Primary Mechanism	Target Objective	Key Example(s)
Facet Engineering	Geometric arrangement of surface atoms	Stabilization of specific transition states (e.g., C-C coupling)	Cu (100) for ethylene formation[19]
Strain Engineering	Mechanical distortion of the lattice	Modulation of d-band center to tune intermediate adsorption	Tensile strain in oxide-derived Cu catalysts[20]
Defect Engineering	Symmetry breaking at high-energy sites	Enhanced CO_2 activation and intermediate stabilization at undercoordinated sites	Grain-boundary-rich Cu nanostructures[21]
Bimetallic Alloying	Electronic and ligand effects	Synergistic tuning of adsorption energetics	Cu-Pd or Cu-Au binary alloys[22]
Single/Dual-Atom Sites	Well-defined active sites	Controlled coordination environments for intermediate stabilization	M-N-C (M=Ni, Co, Fe) SACs[23]

1.4.1 Crystallographic facet engineering: surface symmetry as a selective filter

Facet engineering exploits the structural sensitivity of electrochemical CO_2 reduction reactions, in which the atomic arrangement of surface atoms strongly influences the stabilization of reaction intermediates and thus determines catalytic selectivity and activity. Because different crystallographic facets expose distinct surface geometries and coordination environments, they can stabilize reaction intermediates with different binding strengths. This structural dependence provides a powerful means of tuning catalytic performance through precise control of surface structure.

Early research on Cu single crystals established that low-index facets— (111), (100), and (110)— possess distinct catalytic identities. The Cu (111) facet, being the most closely packed and thermodynamically stable, is predominantly selective toward methane (CH_4)[6,24]. This is attributed to the high barrier for C–C coupling on the (111) surface, which favors the further protonation of *CO to *CHO and eventually to CH_4. In contrast, the Cu (100) facet, exhibits a marked preference for C_{2+} products, specifically ethylene (C_2H_4)[19]. The coordination environment of (100) facet provides a geometric configuration that stabilizes the dimerization of *CO intermediates—a step widely recognized as the rate-determining step for multicarbon formation[19]. The Cu (110) facet, though less stable, has been reported to enable the formation of oxygenates like acetic acid, which

are rarely produced on the (111) or (100) surfaces. This suggests that the open structure of the (110) facet allows for unique orientations of oxygen-bound intermediates[25].

While low-index facets provide a baseline for understanding structure-performance relationships, high-index facets—characterized by periodic steps, kinks, and edges—often exhibit higher intrinsic activity[26]. These undercoordinated sites possess a higher local charge density and can more effectively activate CO_2 and stabilize coupled species[24]. For instance, stepped facets like Cu (211) and Cu (711) have been shown to facilitate the dimerization of *CO at lower overpotentials than flat (100) terraces. The ability to stabilize the *OCCO dimer transition state at these stepped sites is a critical design principle for lowering the energy barrier for ethylene and ethanol production[19].

A significant advancement in facet engineering is the realization that the surface morphology can be shaped *in situ* by the reaction environment. Sargent and co-workers demonstrated that CO_2R intermediates can act similarly to capping agents used in colloidal synthesis[19]. By ensuring the presence of *CO and *H during the electrodeposition of copper, the proportion of Cu (100) facets can be increased by 70%. This "intermediate-favored" synthesis resulted in a 90% Faradaic efficiency for C_{2+} products at a partial current density of 520 mA/cm², demonstrating that engineering the growth conditions to favor specific facets is a viable strategy for achieving high-rate, selective conversion[19].

1.4.2 Mechanical modulation via strain engineering

Strain engineering provides another powerful approach for tuning the catalytic properties of CO_2R catalysts. By introducing tensile or compressive strain into a catalyst lattice, the electronic structure of surface atoms can be modified, thereby altering the adsorption energies of reaction intermediates. In transition-metal catalysts, lattice strain can shift the center of the d-band relative to the Fermi level, which in turn changes the strength of interactions between the catalyst surface and adsorbed species[27]. For copper-based catalysts, theoretical and experimental studies have demonstrated that lattice strain can significantly influence the binding energies of key intermediates such as *CO and *COOH. Tensile strain typically increases the d-band center, strengthening the adsorption of intermediates, whereas compressive strain lowers the d-band center and weakens adsorption[17,20,27,28]. Because catalytic activity often depends on achieving an optimal balance between intermediate stabilization and desorption, mechanically tuning these adsorption energies provides an effective strategy for reducing reaction overpotentials.

A practical application of strain engineering is found in "derived" Cu catalysts, which are formed by the *in situ* reduction of oxidized precursors[20]. During the electrochemical reduction of Cu oxides, hydroxides, or carbonates, the rapid removal of oxygen atoms and the subsequent restructuring of the metallic phase induce significant residual lattice strain. *Operando* XRD characterization has revealed that Cu catalysts derived from $Cu(OH)_2$ and $Cu_2(OH)_2CO_3$ retain considerable tensile strain, which is directly correlated with their high C_{2+} Faradaic efficiency compared to strain-free CuO-derived Cu[20].

Although strain engineering can modify intermediate binding energies and improve catalytic performance, controlling strain in electrocatalysts under operating conditions remains challenging. Electrochemical environments often induce structural reconstruction and relaxation of strained

lattices, which can complicate the interpretation of strain–activity relationships. Nevertheless, strain engineering remains an important strategy for tuning catalyst electronic structure and optimizing catalytic activity.

1.4.3 active site engineering: grain boundaries and defect motifs

Defect engineering focuses on introducing structural imperfections—such as vacancies, step edges, dislocations, and grain boundaries—into catalyst surfaces to create highly active reaction sites. Compared with atoms located on ideal crystalline terraces, atoms at defect sites are typically undercoordinated and possess higher surface energies. These characteristics often lead to enhanced adsorption of reactants and intermediates, thereby facilitating key reaction steps in CO_2 reduction[21,29,30].

A hallmark example of active site engineering is the development of copper nanoparticle ensembles, often referred to as "Cu NOLI" (Nanoparticle-Ordered Ligand Interface) by Yang and co-workers[21]. In this system, densely packed Cu nanoparticles undergo an *in situ* structural transformation during electrolysis into active catalysts consisting rich nanograins[29]. This Cu NP-derived nanograins selectively generate multicarbon products—ethylene, ethanol, and n-propanol—at significantly lower overpotentials than previously reported for polycrystalline Cu. Specifically, in neutral pH aqueous media (0.1 M $KHCO_3$), the C_2–C_3 FE reached 50% at a potential of only -0.75 V vs. RHE[21]. The origin of this enhanced activity is proposed to be the high density of undercoordinated sites and grain boundaries formed during the nanoparticle coalescence[29]. The aggregated Cu nanoparticle consisting of nanograins rich in grain boundaries provide unique geometric and electronic environments that stabilize the dimerization of *CO, effectively lowering the overpotential for deep reduction pathways.

Beyond Cu, defect engineering has been applied to other metals like Bi and Sn to enhance formate production. For instance, high-angle grain boundaries in SnS nanoplates have been shown to lower the barriers for *OCHO stabilization while suppressing competitive *H adsorption[31]. This demonstrates that the specific "twisting angle" and coordination of the grain boundary are critical parameters in catalyst design, moving the field toward a more granular understanding of how imperfections in the lattice can be leveraged for high selectivity.

1.4.4 Bimetallic and high-entropy systems: breaking scaling relationships

Alloying and the development of high-entropy alloys (HEAs) provide further dimensions for electronic tuning. Bimetallic systems can leverage both "ligand effects" (electronic interaction between different metals) and "geometric effects" (arrangement of atoms) to break the linear scaling relations of single metals[22].

HEAs, typically composed of five or more principal elements, offer a "site-occupancy disorder" that creates a nearly continuous distribution of adsorption energies[32]. This allows for the selection of specific sites with optimal adsorption strengths for multiple intermediates simultaneously.[33] Statistical analysis of thousands of binding sites on $(FeCoNiCuMo)_{55}$ clusters revealed that HEAs

can break the established scaling relationships of pure metals, although they often face a trade-off between activity and selectivity due to the diverse site distribution[34]. Nonetheless, the high structural stability and tunable electronic structure of HEAs make them an active research direction for developing robust multi-step CO_2 reduction catalysts[32].

The reduction of catalysts to the atomic scale represents the ultimate limit of active site engineering. Single-atom catalysts (SACs), particularly M-N-C materials (M = Ni, Co, Fe), have demonstrated near-unity Faradaic efficiency for CO production[35]. However, for multicarbon formation, dual-atom catalysts (DACs) are required to provide adjacent sites for C–C coupling[36]. Theoretical screenings indicate that homonuclear DACs like Cu_2 or Ni_2 prefer an asymmetric coupling mechanism (e.g., *CO +*CHO), further highlighting the importance of managing intermediate hydrogenation steps at the atomic level[37].

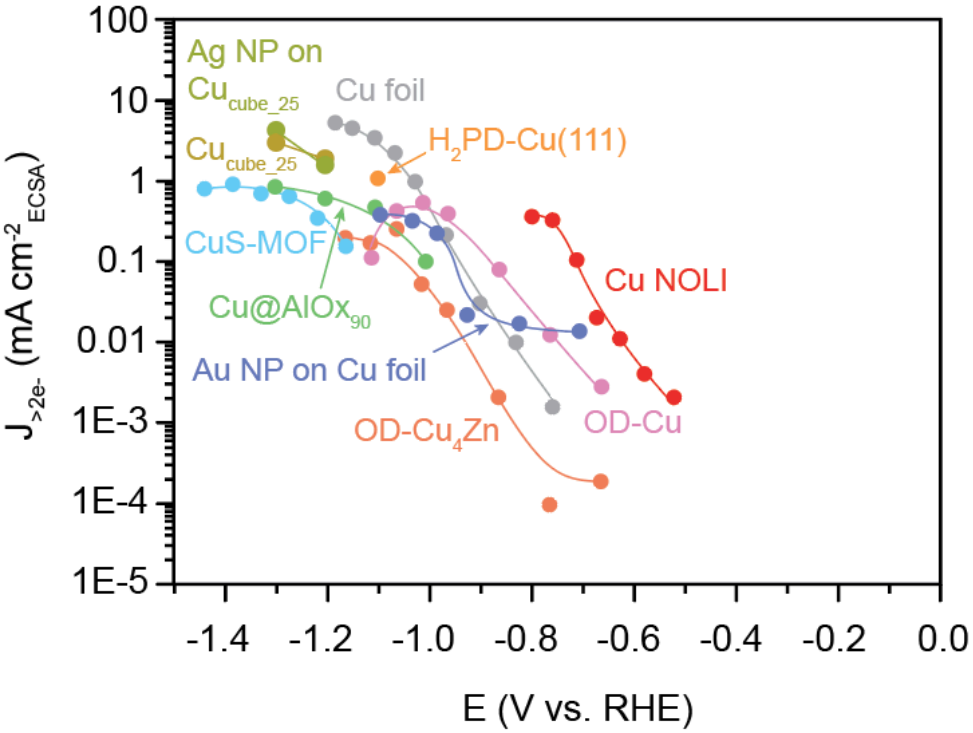

Figure 1.4 Intrinsic activity of representative Cu-based electrocatalysts toward deeply reduced CO_2R products (>2e$^-$) as a function of applied potential. The plotted current densities are normalized by the electrochemically active surface area (ECSA) to reflect intrinsic catalytic activity. All data were extracted from studies conducted in H-cell configurations under near-neutral electrolyte conditions. Representative catalysts included in the comparison are Cu_{Cube_25}[38]; Ag NP on Cu_{Cube_25}[38]; Cu foil[39]; CuS-MOF[40]; Cu@AlOx$_{90}$[41]; Au NP on Cu foil[42]; OD-Cu_4Zn[43]; OD-Cu[43]; H_2PD-Cu(111)[44]; Cu NOLI[21].

The catalyst design strategies discussed above—from facet and strain engineering to defect creation and multimetallic architectures—illustrate the substantial progress made in improving CO_2R performance. As summarized in Figure 1.4, which compares the intrinsic activity of

representative Cu-based electrocatalysts normalized by their electrochemically active surface area (ECSA), these approaches have significantly expanded the accessible design space for copper catalysts.

Nevertheless, an important trend emerges: despite extensive efforts to engineer catalyst morphology, composition, and electronic structure, the majority of Cu-based catalysts still require potentials more negative than −1.0 V vs. RHE to achieve appreciable intrinsic activity toward deeply reduced products. This observation suggests that modifications to the catalyst surface alone may not fully account for the limitations in catalytic performance.

This "activity ceiling" suggests that the intrinsic properties of the catalyst surface are not the only determinant of catalytic performance. The Cu NOLI catalyst, for instance, appears as an outlier in Figure 1.4, exhibiting a distinct overpotential shift in its activity profile. While its high density of grain boundaries is a vital factor, increasing evidence suggests that its performance is also facilitated by the local electrochemical environment. Such strategies demonstrate that "catalyst design" must evolve into "interface design," where the catalyst and its immediate environment are engineered as a synergistic unit. The following section therefore examines how the electrochemical microenvironment, including interfacial ions, solvent structure, and local electric fields, influences catalytic activity and enables CO_2 reduction at significantly lower overpotentials.

1.5 Electrochemical microenvironment effects in CO_2 reduction

Electrochemical CO_2 reduction is governed not only by intrinsic adsorption energetics at the catalyst surface but also by the **electrochemical microenvironment**—the spatially confined reaction zone where local pH, ion concentration, solvent structure, and reactant/product activities can deviate dramatically from bulk electrolyte values[45]. This microenvironment is established by the electrical double layer and continuously reshaped under operating conditions by interfacial electric fields, specific adsorption of electrolyte ions, and local consumption/production of CO_2, H^+/OH^-, and reaction intermediates[45,46].

Building on the preceding discussion of the importance of transferring ‘catalyst design’ to ‘interfacial design’, microenvironment engineering can be viewed as a complementary strategy to catalyst composition/structure tuning: rather than changing only the binding energies of adsorbates on a static surface, microenvironment control targets the effective reaction thermodynamics and kinetics at the interface—including stabilization of charged intermediates, modulation of PCET barriers, and suppression of HER—thereby lowering the cathodic potential needed to reach target rates/selectivities[46]. In this section, we review how (i) ligands and organic modifiers, (ii) cation identity and interfacial availability, (iii) interfacial water structure, and (iv) anion identity and hydrolysis/adsorption behavior influence CO_2R activity, selectivity, and apparent overpotential.

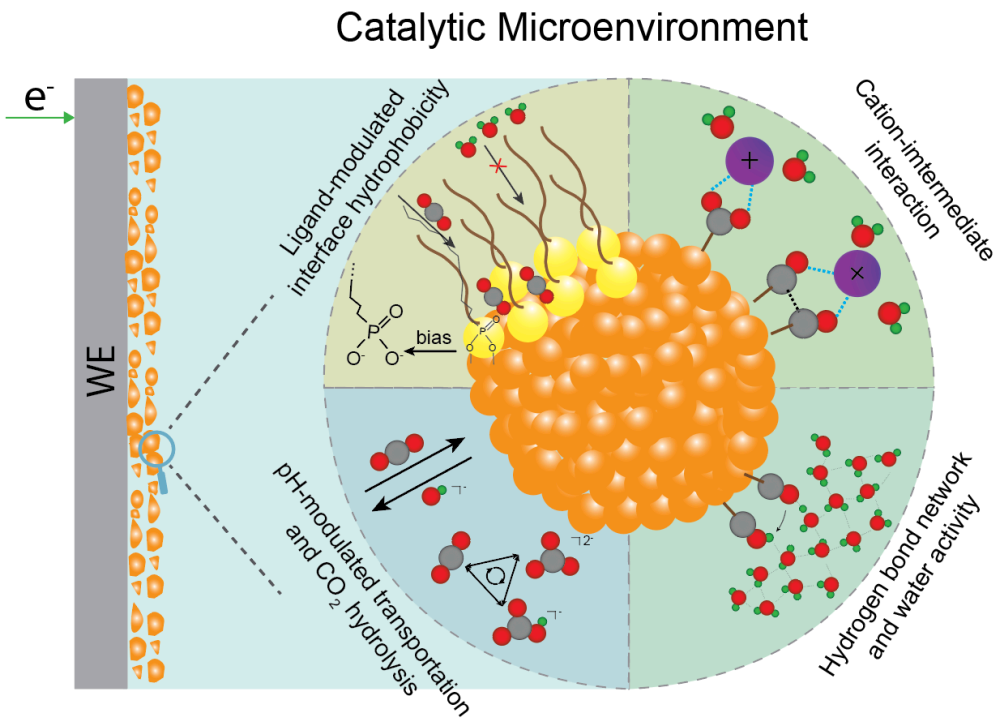

Figure 1.5 Schematic illustration of the electrocatalytic microenvironment at the electrode–electrolyte interface. The catalytic activity and selectivity of CO_2 electroreduction are strongly governed by the nanoscale chemical environment surrounding the catalyst surface. Several key microenvironmental factors collectively influence reaction pathways. (i) Ligand or organic modifier layers. (ii) Electrolyte cations accumulate within the electrical double layer (iii) Interfacial water structure and hydrogen-bond networks (iv) Electrolyte anions. Together, these factors define the catalytic microenvironment that determines the kinetics, activity, and product selectivity of CO_2 electroreduction reactions.

1.5.1 Ligands and organic modifiers

Organic functionalization of catalyst surfaces has emerged as a versatile strategy for engineering the electrochemical microenvironment in CO_2 reduction. Molecular modifiers can be introduced through covalent grafting, weak adsorption of additives or surfactants, porous molecular films, polymer overlayers, or ionomer coatings[47]. Unlike traditional catalyst design strategies that focus solely on modifying the electronic structure of the metal surface, organic modifiers provide additional control over the **local chemical environment at the electrode–electrolyte interface**. Through this approach, the overpotential and selectivity of CO_2R can be tuned via several overlapping mechanisms, including (i) electronic interactions that modify adsorption energetics of reaction intermediates, (ii) regulation of interfacial mass transport and local chemical activities, and (iii) restructuring of the electrical double layer that alters the interfacial electric field and ion solvation structure[47,48]. These mechanisms collectively illustrate how hybrid organic–inorganic interfaces can regulate catalytic behavior beyond the limitations of bare metal surfaces.

One important mechanism by which molecular modifiers enhance CO_2R performance is through **electronic interactions with the catalyst surface**, which alter the adsorption energetics of key intermediates. For example, Sargent and co-workers functionalized Cu electrodes with an electro-derived organic thin film generated from aryl pyridinium precursors[49]. In this system, ethylene Faradaic efficiencies of 72% were achieved with a partial current density of 230 mA cm^{-2} at −0.83 V vs. RHE in a neutral-flow electrolyzer configuration. Furthermore, the catalyst maintained stable operation for approximately 190 hours in a membrane-electrode assembly (MEA) with a full-cell energy efficiency of about 20%[49]. Mechanistic analysis suggests that the organic film stabilizes *CO intermediates that serve as precursors for C–C coupling, effectively lowering the potential required to drive multicarbon product formation and improving catalytic performance under practical operating conditions[49].

Organic modifiers can also influence CO_2R through regulation of **interfacial mass transport and local chemical activities**, particularly by controlling the accessibility of CO_2, H_2O, and local pH at the reaction interface. Polymer and ionomer coatings provide a powerful platform for engineering these transport properties. For instance, hybrid Cu–polymer electrodes have been reported to achieve ethylene Faradaic efficiencies of approximately 87% at −0.47 V vs RHE with a full-cell energy efficiency of about 50%[50]. Spectroscopic studies indicate that the polyamine layer increases the interfacial pH while enriching surface-bound CO intermediates relative to unmodified Cu electrodes. These effects promote C_2 product formation while reducing the operating potential required for high activity[50]. More broadly, thin polymer coatings can also manipulate the local activity ratio of H_2O to CO_2 at the interface. Chen and co-workers demonstrated that polymer gas permeability and water uptake properties strongly influence catalytic performance[48]. Under optimized conditions, the system achieved over 87% Faradaic efficiency toward multicarbon products at current densities exceeding 2 A cm^{-2}, with cathodic energy efficiencies above 50% and operational stability exceeding 150 hours[48]. These results highlight how control of interfacial transport and reactant availability can directly reduce the cathodic potential required to sustain industrially relevant reaction rates.

A third mechanism involves **reconfiguration of the electrical double layer and local electric field through charged organic modifiers**. Cationic surfactants and polyelectrolytes, which contain positively charged functional groups within organic frameworks, are particularly effective in this context. When immobilized on negatively polarized catalyst surfaces, these modifiers create a confined interfacial region in which the ionic groups concentrate the local electric field while the hydrophobic organic framework regulates CO_2 diffusion and water accessibility. This strategy has also enabled efficient CO_2 reduction in acidic electrolytes, where the hydrogen evolution reaction typically dominates. The charged polymer layers suppress proton transport while maintaining strong interfacial electric fields that facilitate CO_2 activation. For example, Li et al. reported a silver catalyst functionalized with the cationic polyelectrolyte poly(diallyldimethylammonium) (PDDA) immobilized on graphene oxide[51]. The high density of cationic sites suppressed proton transport and modulated the interfacial electric field without requiring alkali metal cations in the electrolyte. As a result, the system achieved approximately 85% Faradaic efficiency for CO and a carbon efficiency of 93% at 100 mA cm^{-2} in acidic conditions, with a cathodic energy efficiency of around 35%[51]. Similarly, Sargent and co-workers demonstrated that copper catalysts functionalized with immobilized benzimidazolium groups within ionomer coatings enabled over 150 hours of energy-efficient CO_2 reduction in acidic media, achieving 80% Faradaic efficiency toward C_2+ products[52]. In this case, the cationic groups regulate water and proton transport,

allowing operation at a modest cell voltage of 3.3 V while maintaining a mildly alkaline local environment that favors C_2+ formation[52].

Together, these studies demonstrate that ligand and organic modifier engineering provides a versatile framework for tuning the electrochemical microenvironment through electronic interactions, transport regulation, and electric field modulation. By integrating these effects, molecularly modified interfaces can significantly reduce the overpotential required for CO_2 reduction while simultaneously improving activity and selectivity toward valuable multicarbon products.

1.5.2 Cation effects

Cations accumulate within the electrical double layer (EDL) of negatively polarized electrodes and can exert a profound influence on both the activity and product distribution of electrochemical reactions[46,53-55]. In the context of CO_2 electroreduction (CO_2R), the role of electrolyte cations has been extensively investigated, and several general trends have emerged across a wide range of catalysts and electrochemical configurations. First, the presence of cations is essential for the occurrence of CO_2R, particularly in aqueous H-cell systems[56,57]. Second, the catalytic activity of CO_2R commonly correlates with the identity of the alkali metal cation, typically following the trend $Cs^+ > K^+ > Na^+ > Li^+$ on many metal catalysts including Au, Ag, and Cu[46,53-56]. Notably, this trend has been observed largely independent of catalyst morphology or cell configuration, highlighting the fundamental role of electrolyte cations in shaping the reaction environment[55].

Despite the clear experimental evidence for cation-dependent activity trends, the mechanistic origin of this phenomenon remains an active subject of debate. As summarized in Figure. 1.6, three primary mechanistic frameworks have been proposed to explain how cations influence CO_2R. First, cations can modulate the structure and dynamics of interfacial water, thereby influencing proton transfer kinetics and local pH[58,59]. Second, cations can stabilize reaction intermediates and transition states through electrostatic interactions, either through collective electric-field effects within the EDL (mean-field mechanisms)[60,61] or through specific short-range interactions with adsorbed species[56,62]. Third, recent studies suggest that cations may directly participate in elementary reaction steps through cation-coupled electron transfer (CCET) processes, thereby influencing the kinetics of electron transfer[54,63]. Together, these mechanisms highlight the multifaceted role of electrolyte cations in controlling interfacial reactivity.

Regulation of Interfacial Water Structure and Proton Transfer

Solvated cations can behave as weak proton acids due to the hydrolysis of coordinated water molecules[58]:

$$M^{m+}(H_2O)_n \rightleftharpoons M^{m+}(H_2O)_{n-1}OH^- + H^+ \qquad (3)$$

where *m* denotes the charge of the cation and *n* represents the number of water molecules in its solvation shell. When the local pH exceeds the pKa of the hydrated cation complex, partial dissociation of coordinated water molecules releases protons into the interfacial region.

Consequently, solvated cations can act as buffers that moderate local pH fluctuations near the electrode surface.

Beyond their buffering capability, cations strongly influence the organization of surrounding solvent molecules and therefore the structure of interfacial water. Smaller alkali metal cations such as Li^+ possess stronger cation–water interactions and more rigid hydration shells than larger cations such as Cs^+[54,55]. As a result, Li^+ tends to impose a more ordered interfacial water structure, whereas larger cations generate a more weakly coordinated and dynamically disordered interfacial solvent environment[54,55]. The structure of interfacial water has important kinetic consequences for electrochemical reactions. Variations in solvent organization can influence parameters such as activation entropy and solvent reorganization energy[64,65]. For example, increasing $NaClO_4$ concentration has been shown to disrupt the hydrogen-bond network at the electrode interface, increasing the apparent activation entropy and resulting in an approximately 18-fold increase in the current density toward C_2^+ products during CO_2R on Cu electrodes[65]. Moreover, the local concentration, orientation, and hydrogen-bond structure of proton donors exhibit pronounced cation dependence, indicating that cations play a critical role in regulating proton-transfer kinetics at the interface.

The impact of cations on proton transfer can also lead to deviations from the conventional cation activity trend. For instance, during CO_2 reduction to methanol on cobalt phthalocyanine (CoPc) catalysts, the rate-determining step involves proton transfer to the *CHO intermediate[66]. In this case, smaller and more strongly hydrated cations such as Li^+ can polarize coordinated water molecules and weaken the O–H bond, thereby facilitating proton transfer. As a result, the methanol production rate follows an inverse trend of $Li^+ > Na^+ > K^+ > Cs^+$[66]. In contrast, proton transfer is not believed to be involved in the rate-determining step of C_2^+ product formation on Cu surfaces, where the conventional cation activity trend is generally observed.

Electrostatic stabilization of reaction intermediates

Cations can also influence CO_2R by modifying the energetics of reaction intermediates and transition states through electrostatic interactions[56]. Two primary interpretations have been proposed to describe this effect (Figure 1.6b).

The first interpretation attributes the cation effect to the interfacial electric field generated by the collective accumulation of cations within the EDL under cathodic biases. In this mean-field description, the identity and concentration of electrolyte cations determine the strength of the electric field near the electrode surface[13]. Larger alkali metal cations such as Cs^+ typically accumulate more densely at the interface and therefore generate stronger interfacial electric fields than smaller ions such as Li^+[55]. These fields can stabilize dipolar reaction intermediates such as $*CO_2^-$ and $*OCCO^-$, thereby lowering activation barriers and enhancing catalytic activity. Such electric-field effects have been identified as dominant contributors to activity trends in certain non-aqueous CO_2R systems employing bulky organic cations[60,61].

An alternative interpretation emphasizes specific short-range interactions between cations and adsorbed intermediates within the EDL. In this framework, (partially desolvated) cations interact directly with surface-bound intermediates through Coulombic attraction or partial coordination[56,62]. Hydrated alkali metal cations with softer and more weakly bound hydration shells, such as Cs^+,

can approach the electrode surface more closely and pack more densely within the interfacial region[58]. A higher local concentration of interfacial cations increases the stabilization of key intermediates such as $*CO_2^-$ during CO formation or *OCCO during C–C coupling[56,62]. These stabilization effects are therefore consistent with the experimentally observed activity trend of $Li^+ < Na^+ < K^+ < Cs^+$ for many CO_2R catalysts.

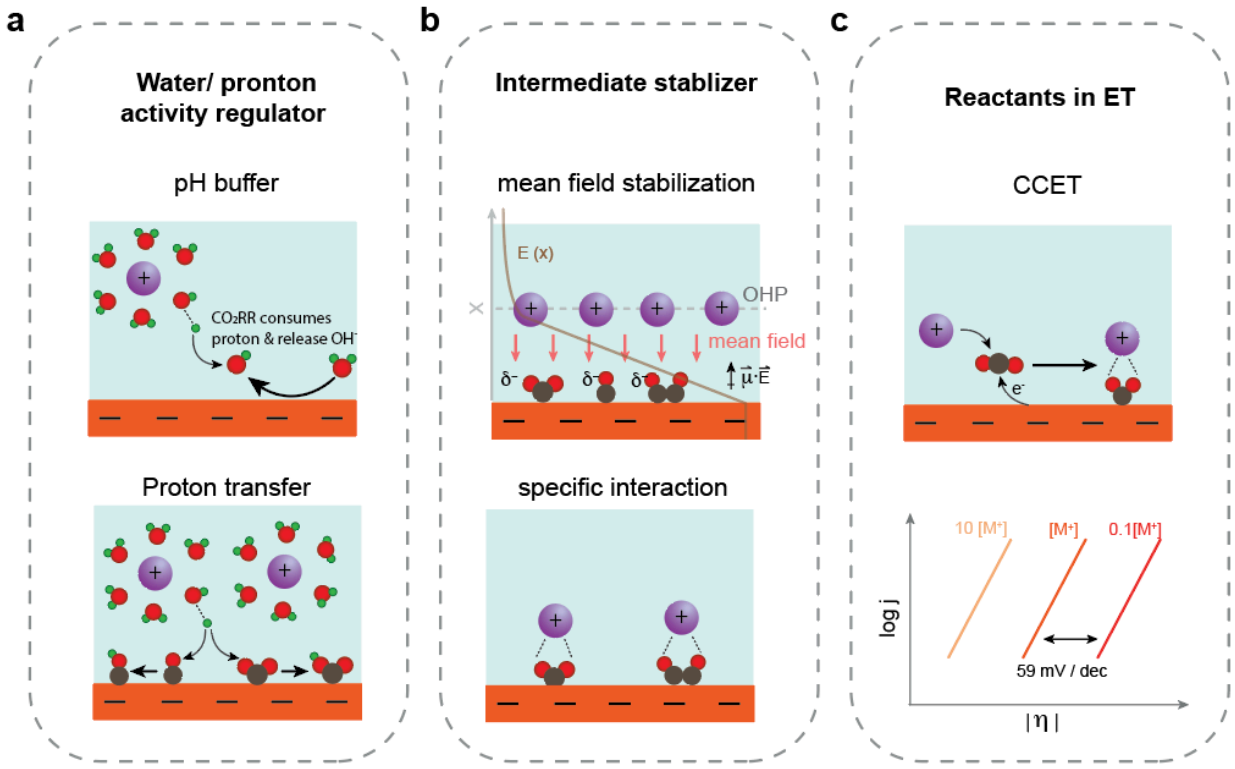

Figure. 1.6. Mechanistic pathways through which electrolyte cations influence CO_2 electroreduction. a, Regulation of interfacial water structure and proton transfer. Cations organize the hydrogen-bond network of surrounding water molecules and can buffer local pH through hydrolysis of hydrated complexes, thereby influencing proton transport and reaction kinetics. **b,** Electrostatic stabilization of intermediates. Accumulated cations at the OHP stabilize reaction intermediates either through collective electric-field effects (mean-field stabilization) or through specific short-range Coulombic interactions with adsorbed species. **c,** Cation-coupled electron transfer (CCET). Cations directly participate in electron-transfer steps by forming complexes with reaction intermediates, resulting in kinetic behavior characterized by a Nernstian shift of approximately 59 mV per decade change in cation concentration. Solvation structures are omitted in panels (**b**) and (**c**) to emphasize the role of cation–intermediate interactions beyond hydration effects. Purple: cation; red: oxygen; brown: carbon; green: hydrogen.

Cation-Coupled Electron Transfer Mechanisms

Beyond modifying the electrostatic environment, increasing evidence suggests that cations may directly participate in elementary reaction steps through cation-coupled electron transfer (CCET)

mechanisms[54,55]. In such processes, cations form transient complexes with reaction intermediates during electron transfer, thereby altering both the thermodynamics and kinetics of the reaction[54].

For example, CO_2 adsorption and C–C coupling during CO_2R have been proposed to proceed via CCET mechanisms[54,55]:

$$* + CO_2 + e^- + M^+ \rightleftharpoons *CO_2 \cdots M^+ \quad (4)$$

$$* + 2CO + e^- + M^+ \rightleftharpoons *OCCO^- \cdots M^+ \quad (5)$$

These elementary steps correspond to key processes in the formation of CO and C_2^+ products, respectively. Within the Butler–Volmer formalism, the reaction rate under a CCET mechanism depends explicitly on the interfacial cation concentration. The current density for CO formation can therefore be expressed as

$$j_{CO} = nFKP_{CO_2}C_{M^+}e^{-\alpha_c F(E-E^0)/RT} \quad (6)$$

where F, R, and T denote the Faraday constant, gas constant, and temperature; n and k represent the number of electrons and the rate constant of the elementary step; P_{CO_2} denotes the CO_2 partial pressure. E^0 is the formal reduction potential of the elementary step reaction (4); α_c is the cathodic charge transfer coefficient; and C_{M^+} is the interfacial cation concentration.

A key implication of this framework is that the current density scales linearly with the interfacial cation concentration. While experimentally quantifying the interfacial cation concentration still imposes a huge challenge, CCET predicts a Nernstian potential shift of approximately 59 mV per decade change in cation concentration on the SHE scale, as illustrated in Figure. 1.6c. Such behavior has been experimentally observed on polycrystalline Ag and Cu electrodes[54]. These findings suggest that cations may function not merely as components of the electrolyte environment but as active participants in the catalytic cycle, fundamentally influencing the kinetics of CO_2 electroreduction.

In summary, electrolyte cations influence CO_2 electroreduction through multiple interconnected mechanisms spanning solvent structure, electrostatic stabilization, and direct participation in electron-transfer processes. By regulating interfacial water organization and proton-transfer kinetics, stabilizing charged intermediates through electric-field and specific interactions, and participating in cation-coupled electron transfer reactions, cations play a central role in controlling both the activity and selectivity of CO_2R. These insights demonstrate that electrolyte composition is not merely a passive component of electrochemical systems but rather a critical element of the catalytic microenvironment. Understanding and engineering cation effects therefore provide an important strategy for tuning reaction pathways and reducing overpotentials in CO_2 electroreduction systems.

1.5.3 Interfacial water structure

As the primary proton source in aqueous electrolytes under neutral and alkaline conditions, water is not merely a solvent in CO_2 electroreduction but an active participant in the multi-electron and multi-proton transfer processes that define the reaction[6]. In recent years, increasing evidence has demonstrated that the structure and dynamics of interfacial water, particularly the topology of the

hydrogen-bond (H-bond) network, play a critical role in determining both catalytic activity and product selectivity[67]. Within the electrical double layer (EDL), water molecules organize into distinct structural motifs that differ substantially from bulk water, and these structures strongly influence proton transport, intermediate stabilization, and reaction energetics[67]. This section discusses the mechanisms through which the interfacial water environment governs the efficiency and selectivity of CO_2R.

Electrocatalytic reactions occur within the EDL, a nanoscale region extending roughly ~1 nm from the electrode surface where electric fields can reach magnitudes on the order of 10^9 V m^{-1}. Such intense fields significantly influence the orientation, polarization, and connectivity of interfacial water molecules[68]. Moreover, interfacial water experiences asymmetric boundary conditions: the solid electrode on one side and the bulk liquid phase on the other. As a result, water molecules within approximately 0.4–1.0 nm of the surface exhibit pronounced structural heterogeneity compared with the tetrahedral hydrogen-bond network characteristic of bulk water[68].

Spectroscopic studies, particularly vibrational spectroscopy probing the O–H stretching region, have resolved three characteristic classes of interfacial water based on their hydrogen-bond environments[57,65,69,70]:

1) **Low-frequency water (LF-w):** Appearing between 3200–3300 cm^{-1}, this band corresponds to strongly hydrogen-bonded water molecules forming an ordered, tetrahedral network reminiscent of ice-like structures.
2) **Middle-frequency water (MF-w):** Located around ~3400 cm^{-1}, this band represents partially hydrogen-bonded water molecules typically participating in two to three hydrogen bonds.
3) **High-frequency water (HF-w):** Observed between 3500–3600 cm^{-1}, this band corresponds to weakly hydrogen-bonded or "free-like" water molecules, often associated with cation-coordinated water or disrupted hydrogen-bond networks.

The relative abundance of these water species is strongly potential-dependent and can serve as a sensitive descriptor of the interfacial microenvironment. As the electrode potential becomes more negative, the interfacial region typically exhibits an initial increase in HF-w populations due to enhanced cation accumulation and coordination. At more negative potentials, increased crowding of hydrated ions, adsorbates, and intermediates can further reorganize the hydrogen-bond network, leading to an increased fraction of MF-w species[69].

The preferred interfacial water structure for CO_2R depends strongly on the rate-determining step (RDS) of the target reaction pathway. When proton transfer is involved in the RDS, a well-connected hydrogen-bond network facilitates efficient proton transport. For example, the formation of methane (CH_4) from CO_2 involves proton transfer in its rate-limiting step; therefore, a higher fraction of LF-w species, which support efficient proton shuttling through extended hydrogen-bond networks, is beneficial for this pathway. In contrast, C–C coupling steps that lead to multicarbon (C_2^+) products generally do not involve proton transfer in their RDS. In these cases, a more disrupted hydrogen-bond network characterized by increased HF-w populations can suppress proton availability at the interface, thereby inhibiting competing hydrogen evolution reactions (HER) and favoring C–C coupling pathways[67].

Manipulating the relative abundance of water species with different hydrogen-bond configurations therefore provides a powerful strategy for tuning CO_2R selectivity. For instance, silver (Ag)

catalysts are traditionally known for their high selectivity toward CO formation. However, engineering the interfacial microenvironment to increase the fraction of HF-w species can shift the reaction pathway toward formate (HCOOH) production[71]. One approach involves introducing polymeric cations such as poly(diallyldimethylammonium chloride) (PDDA), which create a locally hydrophobic environment at the electrode surface[71]. Under these conditions, the hydrogen-bond network becomes significantly disrupted, increasing the proportion of HF-w species[71]. This modified interfacial structure enables an alternative reaction pathway in which CO_2 is directly hydrogenated by surface-adsorbed hydrogen (*H + CO_2), leading to formate formation[71]. In contrast, conventional aqueous electrolytes dominated by strongly hydrogen-bonded LF-w species favor the formation of the *COOH intermediate, resulting primarily in CO production[71]. These observations establish a direct relationship between water structural motifs and specific reaction pathways and demonstrate that nanoscale water organization can override the intrinsic selectivity of a catalyst.

On copper (Cu) catalysts, which uniquely enable efficient C–C coupling, the interfacial water environment plays an especially important role in determining the distribution between C_1 and C_2^+ products. The formation of ethylene (C_2H_4) is widely believed to proceed through the coupling of two adsorbed CO species (*CO + *CO), a step that is largely insensitive to proton availability. In contrast, methane formation involves proton transfer in its rate-determining step and is therefore strongly dependent on local proton flux[6,67,72]. By disrupting the hydrogen-bond network—for example through highly concentrated electrolytes or hydrophobic surface modifiers—the accessibility of water molecules at the interface can be reduced[72]. This restriction decreases the formation of surface *H species and suppresses both the hydrogen evolution reaction and the *CO hydrogenation pathway responsible for C_1 products[72]. As a result, the C–C coupling pathway becomes relatively favored, leading to enhanced selectivity toward multicarbon products[72].

In summary, the structure and dynamics of interfacial water constitute a fundamental descriptor governing the activity and selectivity of CO_2 electroreduction. Over the past decade, growing experimental and theoretical evidence has revealed that the hydrogen-bond network acts not only as a passive solvent environment but also as a dynamic proton-transfer medium and micro-solvation framework that shapes the energetic landscape of catalytic reactions. By engineering the electrode–electrolyte interface through strategies such as cation selection, electrolyte concentration control, incorporation of organic modifiers, and regulation of water activity, it is possible to manipulate interfacial water organization and thereby control proton transport, electric field distribution, and reaction selectivity.

1.5.4 Anion effects

In the electrochemical carbon dioxide reduction reaction (CO_2R), anions were historically regarded as inert supporting electrolyte species. However, recent studies have demonstrated that anions play an active role in shaping the chemical environment at the EDL. Through their influence on local pH, interfacial electric fields, adsorption equilibria, and catalyst surface structure, anions can significantly affect both catalytic activity and product selectivity. Consequently, electrolyte anions are now recognized as critical components of the electrochemical microenvironment that govern reaction pathways in CO_2R[6,73].

One of the most important roles of anions is their ability to regulate the local pH near the electrode surface[6,73]. During CO_2R, the consumption of protons and the generation of hydroxide ions (OH^-) lead to a substantial increase in local alkalinity within the electrical double layer. This local pH shift can suppress CO_2 reduction by decreasing the concentration of dissolved CO_2 and promoting the competing hydrogen evolution reaction (HER). Buffering anions such as bicarbonate (HCO_3^-) and phosphate ($H_2PO_4^-$) mitigate this effect by participating in acid–base equilibria that neutralize the locally generated hydroxide ions. By stabilizing the interfacial pH, these buffering species maintain a higher concentration of dissolved CO_2 near the electrode surface and facilitate the initial proton-coupled electron transfer steps of the reduction reaction. As a result, electrolyte buffering capacity plays an important role in sustaining CO_2R activity under practical operating conditions[73].

Beyond pH regulation, anions can also influence CO_2R by modifying the adsorption energetics of reaction intermediates through interactions within the electrical double layer. Recent studies have proposed the free energy of anion physisorption as an important descriptor for catalytic performance[73,74]. Weakly adsorbing anions, such as propionate or perchlorate, minimally perturb the catalyst surface and often enable more favorable kinetics for the formation of key intermediates[75]. For example, weakly coordinating electrolytes have been reported to enable nearly quantitative FE for CO formation on gold catalysts[75]. In contrast, specifically adsorbing anions—particularly halides such as Cl^-, Br^-, and I^-—can interact directly with the catalyst surface[74]. These anions may donate partial negative charge to the electrode surface or participate in non-covalent interactions with adsorbed intermediates. Such interactions can stabilize reaction intermediates such as *COOH or *OCCO, thereby modifying the energetic landscape of the catalytic pathway and enabling selective promotion of either C_1 hydrogenation reactions or C–C coupling processes depending on the identity and coverage of the anion[74].

Anions can additionally influence CO_2R through dynamic restructuring of the catalyst surface during electrolysis. Under electrochemical conditions, certain anions can induce surface reconstruction processes that modify catalyst morphology and expose new active sites[73]. For instance, studies on silver electrodes have shown that the presence of halide ions in the electrolyte can promote continuous dissolution and redeposition processes, leading to the formation of well-defined crystal facets that exhibit enhanced selectivity for CO production[76]. Similar phenomena have been reported for copper catalysts, where halide ions can induce nanostructuring and surface faceting that increase the density of catalytically active sites[77,78]. These anion-induced structural transformations can significantly alter catalytic performance by modifying surface roughness, coordination environments, and intermediate adsorption properties. Such dynamic restructuring highlights the important role of electrolyte composition in governing catalyst evolution under reaction conditions.

In summary, anions influence CO_2 electroreduction through several interconnected mechanisms, including the regulation of local pH through buffering equilibria, modulation of intermediate adsorption via specific or non-specific interactions within the electrical double layer, and the dynamic restructuring of catalyst surfaces during electrolysis. These findings underscore that electrolyte anions are not passive spectators but active components of the catalytic microenvironment.

1.6 Knowledge gaps and thesis objectives

Section 1.5 demonstrate that the electrochemical microenvironment plays a fundamental role in determining the activity, selectivity, and overpotential of CO_2 electroreduction. Factors such as ligands, electrolyte cations, solvent structure, and anions collectively define the local reaction environment at the electrode–electrolyte interface. By modulating the stabilization of intermediates, proton transfer kinetics, and local electric fields, these microenvironmental components can substantially influence catalytic performance. Despite these advances, a comprehensive understanding of how these factors interact and collectively determine catalytic behavior remains incomplete. Several key knowledge gaps continue to limit the rational design of microenvironment-engineered catalysts for low-overpotential CO_2 reduction.

First, the electrochemical microenvironment is governed by complex and strongly coupled interactions among multiple interfacial species. Modifying one component of the microenvironment often simultaneously perturbs several others. For example, changing the electrolyte cation can alter not only the electric field within the electrical double layer but also the structure of interfacial water and the distribution of anions near the surface. Similarly, the introduction of organic ligands or surface modifiers can influence cation accumulation, solvent organization, and local reactant transport simultaneously. As a result, it remains difficult to isolate which specific parameters directly contribute to lowering overpotential and which effects arise as secondary consequences of broader interfacial restructuring. Many existing studies focus on modifying a single microenvironmental parameter in isolation, making it challenging to identify the dominant factors that should be prioritized in the rational design of catalysts targeting low-overpotential CO_2 electroreduction.

Second, our mechanistic understanding of the electrochemical microenvironment largely relies on indirect evidence. Many proposed mechanisms—including the formation of cation–intermediate complexes or the restructuring of hydration shells near the interface—are inferred from electrochemical kinetic analysis or theoretical simulations rather than directly observed experimentally. A major obstacle arises from the limited availability of experimental tools capable of directly probing the various components of the microenvironment under operating conditions. Different *in situ* techniques typically provide information on only one aspect of the interface. For example, vibrational spectroscopies such as infrared or Raman spectroscopy can probe adsorbed intermediates, ligands, and water structure but are generally insensitive to cation distributions. Conversely, techniques capable of detecting electrolyte ions often provide limited information about molecular adsorbates or solvent structure. Consequently, a comprehensive picture of the microenvironment requires the integration of multiple complementary in situ techniques capable of probing ligands, intermediates, ions, and solvent structure simultaneously.

Third, electrochemical catalysts often undergo dynamic structural evolution during operation, leading to spatially heterogeneous reaction environments. Surface restructuring processes—such as nanoparticle aggregation, formation of grain boundaries, and dynamic changes in surface morphology—can generate nanoscale variations in the electrical double layer and local electrolyte composition. However, most electrochemical measurements and many spectroscopic techniques provide ensemble-averaged information over large surface areas. These approaches obscure the spatial heterogeneity that may play a critical role in catalytic performance. Achieving nanometer-resolved insights into the electrochemical microenvironment therefore represents an important

frontier for understanding how local interfacial environments influence catalytic activity and selectivity.

Addressing these challenges requires experimental strategies capable of directly probing multiple components of the electrochemical microenvironment with high spatial and chemical resolution. The objective of this thesis is to develop such a tool kit and processes using model catalytic systems in which the interactions among ligands, electrolyte ions, solvent molecules, and reaction intermediates can be systematically investigated. Specifically, this work aims to

(i) Establish a group of model catalysts that exhibit well-defined microenvironment interactions.

(ii) Directly track the evolution of key microenvironmental species—including ligands, water, and electrolyte cations—under electrochemical operating conditions using complementary *in situ* spectroscopic techniques.

(iii) Achieve nanometer-resolved characterization of the electrochemical interface to reveal spatial heterogeneity in the reaction environment.

By integrating these experimental approaches, **this thesis seeks to elucidate how interactions within the electrochemical microenvironment influence the kinetics of CO_2 activation and intermediate stabilization, ultimately enabling CO_2 reduction at unusually low overpotentials.** The insights obtained from these studies aim to establish general design principles for engineering electrochemical microenvironments, providing a conceptual framework that links interfacial structure to catalytic performance in CO_2 electroreduction. The following chapters will investigate these questions through detailed mechanistic studies of ligand-modulated catalytic systems and copper-based catalysts, with the goal of revealing how microenvironment engineering can enable efficient CO_2 conversion at reduced energy input.

Chapter 2 Origin of Low Overpotential in Nanoparticle-Ordered Ligand Interlayer (NOLI)

Portions of the content and figures in this chapter are reproduced with permission from:

Yu Shan#, Xiao Zhao#, Maria Fonseca Guzman#, Asmita Jana, Shouping Chen, Sunmoon Yu, Ka Chon Ng, Inwhan Roh, Hao Chen, Virginia Altoe, Stephanie G. Corder, Hans A. Bechtel, Jin Qian, Miquel B. Salmeron, Peidong Yang, *Nanometre-resolved Observation of Electrochemical Microenvironment Formation at the Nanoparticle–Ligand Interface*, Nature Catalysis, 7, 422–431 (2024)[79]

Yu Shan#, Maximilian Jaugstetter#, Julian Feijoo#, Yani Guan#, Tianle Wang, Lorenz J. Falling, Jialu Li, Honghe Ding, Alex Sachelarie, Maria Fonseca Guzman, Xiao Zhao, Robert Michael Kowalski, Slavomír Nemšák, Jinghua Guo, Philippe Sautet, Miquel B. Salmeron, and Peidong Yang, *Desolvated Cation Promotes CO_2 Electroreduction through Partial Covalent Interaction*, (2026, in revision).

2.1 Preface

In Chapter 1, we discussed how the electrochemical microenvironment surrounding a catalytic surface can strongly influence the activity and selectivity of CO_2 electroreduction. However, directly probing these microenvironmental effects remains challenging because the relevant interactions involve multiple components—ligands, ions, solvent molecules, and reaction intermediates—coupled within a dynamic interfacial structure.

The nanoparticle-ordered ligand interlayer (NOLI) system provides a unique model platform in which many of these microenvironmental interactions naturally coexist. In this system, metal nanoparticles capped with organic ligands evolve under electrochemical bias to form a confined interfacial region containing ligands, ions, and structured water. The resulting environment enables unusually efficient CO_2 electroreduction at significantly reduced overpotentials compared with conventional metal electrodes.

In this chapter, we systematically investigate the origin of this low-overpotential behavior in Ag-based NOLI catalysts. Using a combination of *in situ* vibrational spectroscopy and element-specific electronic spectroscopy, we probe the interactions among ligands, cations, water molecules, and reaction intermediates with both chemical and spatial sensitivity. Through these studies, we aim to address two central questions:

1. **How does the NOLI structure form under electrochemical conditions?**
2. **How does the resulting microenvironment promote CO_2 reduction at low overpotential?**

By answering these questions, this chapter establishes a mechanistic understanding of how microenvironmental effects can fundamentally alter electrochemical reaction energetics. The insights obtained here also provide broader design principles for engineering catalytic interfaces that enable low-overpotential CO_2 conversion.

2.2 NOLI architecture and hypothesis

Between 2017 and 2020, the Yang group synthesized a family of colloidal metal nanoparticles capped with organic ligands, where the metal core can be Cu, Au, Ag, or Pd and the surface ligand is tetradecylphosphonic acid (TDPA)[21,80]. These nanoparticles are synthesized with well-controlled size and shape, typically smaller than 10 nm in diameter (Figure 2.1a). When deposited onto conductive substrates, the nanoparticles assemble into closely packed assemblies in which the surface ligands from neighboring nanoparticles interdigitate (Figure 2.1b).

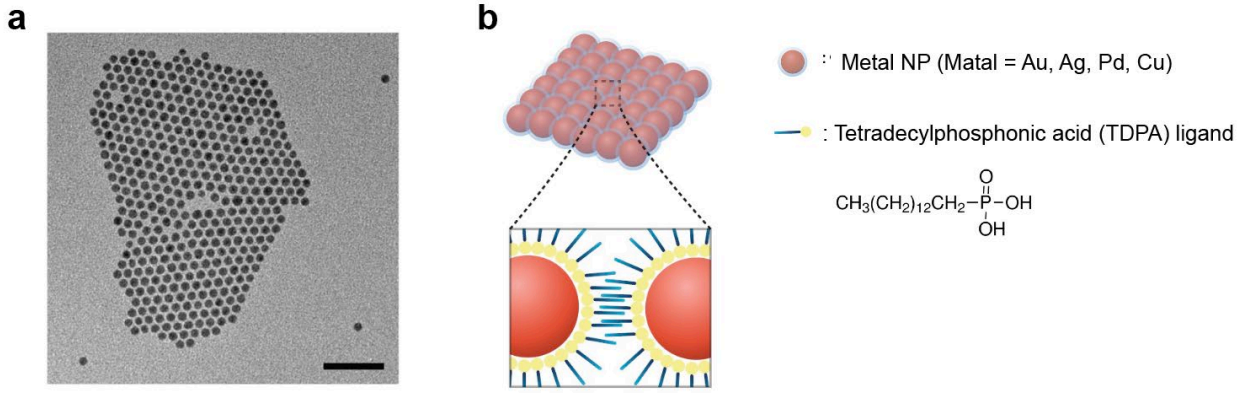

Figure. 2.1. Colloidally synthesized metal nanoparticle assemblies used as pre-catalyst for NOLI catalysts. a, Transmission electron microscopy (TEM) image of as-prepared Ag nanoparticles capped with tetradecylphosphonic acid (TDPA). Scale bar: 50 nm. **b,** Schematic illustration of ligand interdigitation between neighboring nanoparticles within assembled nanoparticle structures. Panel (**a**) reproduced with permission from Ref.[80]. Copyright © 2020 Springer Nature.

Electrochemical measurements reveal that these nanoparticle assemblies exhibit remarkably improved catalytic performance compared with conventional metal electrodes. As shown in Figure 2.2, the FE values for CO production on Au and Ag nanoparticles—and for ethylene production on Cu nanoparticles—display a substantial positive shift in activity of approximately 200 mV relative to their corresponding thin-film or single-crystal electrodes. The fact that this enhancement occurs across multiple metals suggests that the improved performance arises from features common to the nanoparticle assemblies, rather than from a specific metal surface structure. In particular, the presence of surface ligands is likely to play a critical role in shaping the catalytic microenvironment.

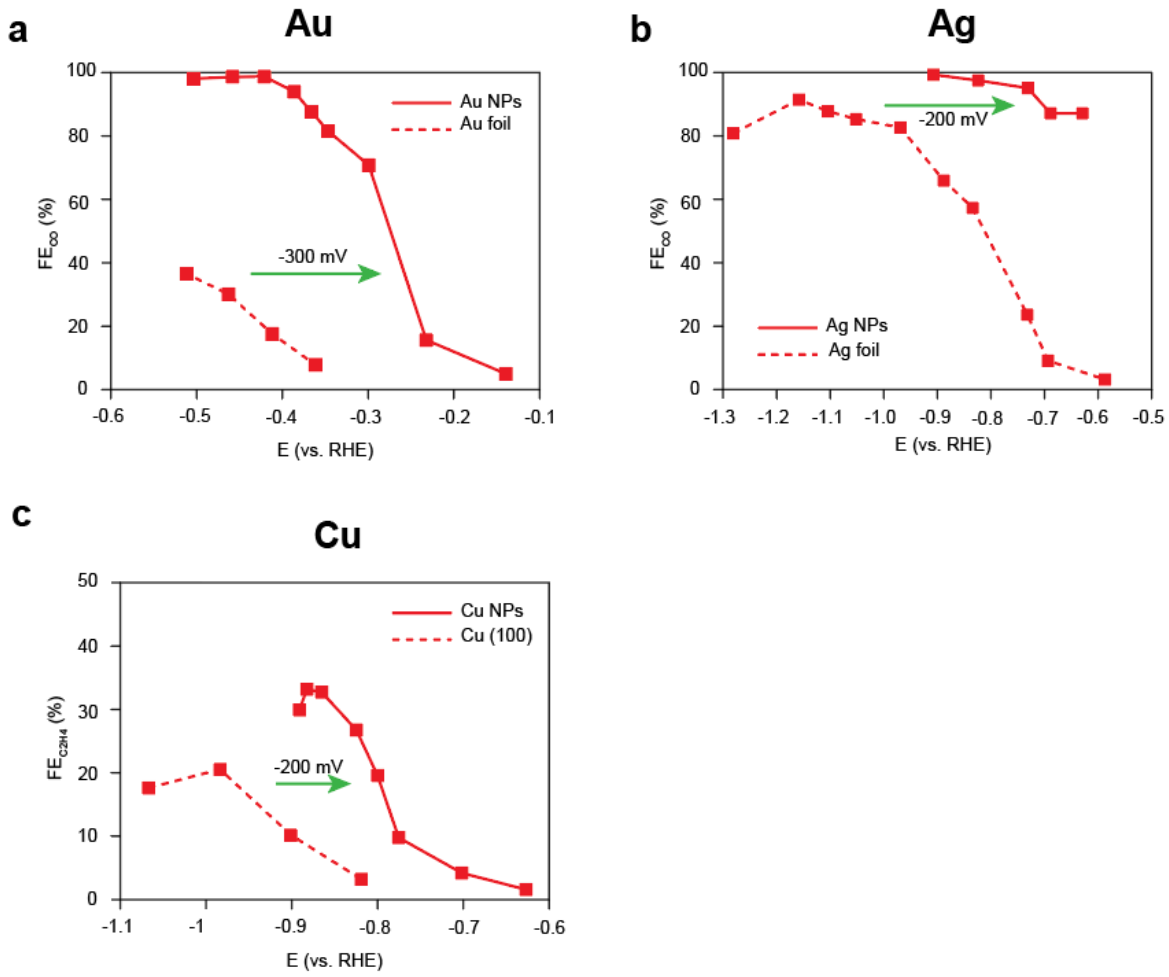

Figure. 2.2. Electrochemical performance comparison between nanoparticle catalysts and conventional metal electrodes. a, b Faradaic efficiency for CO production as a function of applied potential for Au nanoparticles versus Au foil **(a)** and Ag nanoparticles versus Ag foil **(b). c,** Faradaic efficiency for ethylene formation on Cu nanoparticles compared with Cu(100) single-crystal electrodes. Data for Au NP and Ag NP is reproduced from Ref.[80], while data for Cu is reproduced from Ref.[21].

Several key observations further indicate that the enhanced reactivity does not originate from a unique catalytic active site, but rather from the interfacial environment created by the nanoparticle–ligand assembly. First, during electrolysis the initially small nanoparticles undergo significant structural evolution, coarsening into larger particles with average diameters of 30–40 nm (Figure 2.3a). This indicates that the active catalyst under reaction conditions is not the original colloidal nanoparticles, but the evolved metallic particles formed during operation. In addition, removal of the ligands results in a dramatic decrease in catalytic performance, returning activity levels to those comparable to bare Ag foil (Figure 2.3b, c). This observation highlights the essential role of the ligand layer in sustaining the enhanced reactivity. Furthermore, the spatial arrangement of nanoparticles also influences catalytic behavior. Only closely assembled nanoparticle structures

exhibit the boosted activity, whereas isolated nanoparticles distributed on the support show no comparable enhancement (Figure 2.3d, e). When nanoparticles assemble, ligands originating from neighboring particles can interdigitate and form a collective ligand structure that cannot exist around isolated particles.

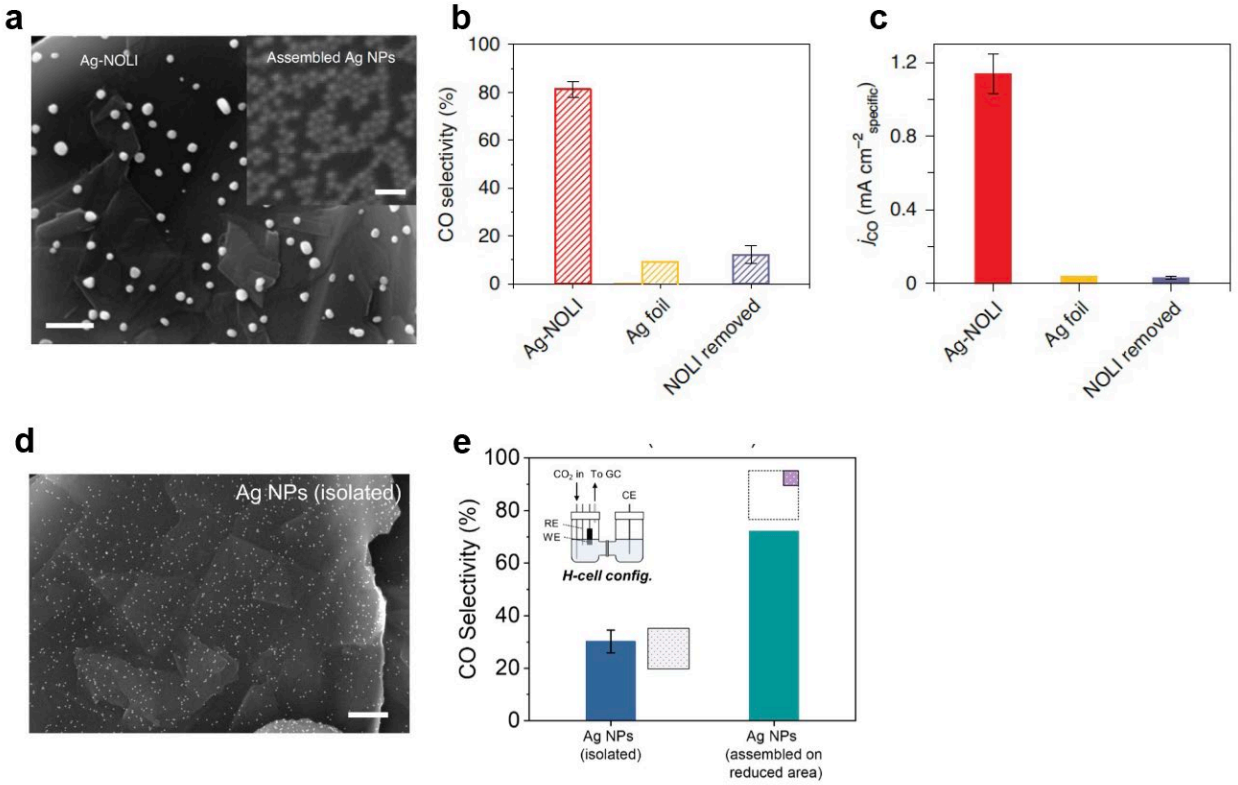

Figure. 2.3 Experimental observations indicating that enhanced NOLI activity does not originate from a unique active site. **a,** SEM images of assembled Ag nanoparticles before electrolysis and evolved Ag particles after NOLI formation. Scale bars: 25 nm (as-prepared assembly) and 200 nm (evolved particles). **b, c** CO selectivity (**b**) and ECSA-normalized CO partial current density (**c**) for Ag NOLI, Ag foil, and a ligand-removed control sample. **d,** SEM image of isolated Ag nanoparticles distributed on carbon paper. Scale bar: 200 nm. **e,** Comparison of CO selectivity for assembled versus isolated nanoparticle distributions. Figures reproduced with permission from Ref.[80] . Copyright © 2020 Springer Nature.

Based on these findings, we propose the following hypothesis for the formation of the nanoparticle-ordered ligand interlayer (NOLI) (Figure 2.4). When ligand-capped nanoparticles assemble on an electrode surface, the ligands on neighboring particles interdigitate to form a cooperative ligand network. Under an applied electrochemical bias, two processes occur simultaneously: the nanoparticles undergo coarsening and fusion, while the ligands detach from the metal surface. Instead of diffusing away into the bulk electrolyte, however, the ligands remain confined near the nanoparticle surface due to their collective interactions. This process leads to the formation of a distinctive interfacial architecture consisting of a metallic nanoparticle core, a confined aqueous layer, and an ordered ligand layer surrounding the particle. The resulting

structure forms the nanoparticle-ordered ligand interlayer (NOLI). Within this confined region, interactions among ligands, ions, and solvent molecules generate a unique electrochemical microenvironment that can facilitate CO_2 reduction at unusually low overpotentials.

Although this hypothesis provides a conceptual framework, it also raises several important questions. It remains unclear how ligands dynamically behave under electrochemical conditions and how the resulting microenvironment modifies the electrical double layer to promote CO_2 reduction. To address these questions, the following sections examine two key aspects of the NOLI system. Section 2.3 investigates the formation mechanism of NOLI by directly probing ligand dynamics at nanometer resolution. Section 2.4 then explores how ligand-modulated cation desolvation alters the energetics of intermediates and enables low-overpotential CO_2 reduction. Ag NOLI system will be chosen as a model system since Ag offers greater stability under applied potentials and features a simpler, better-understood CO_2-to-CO conversion pathway.

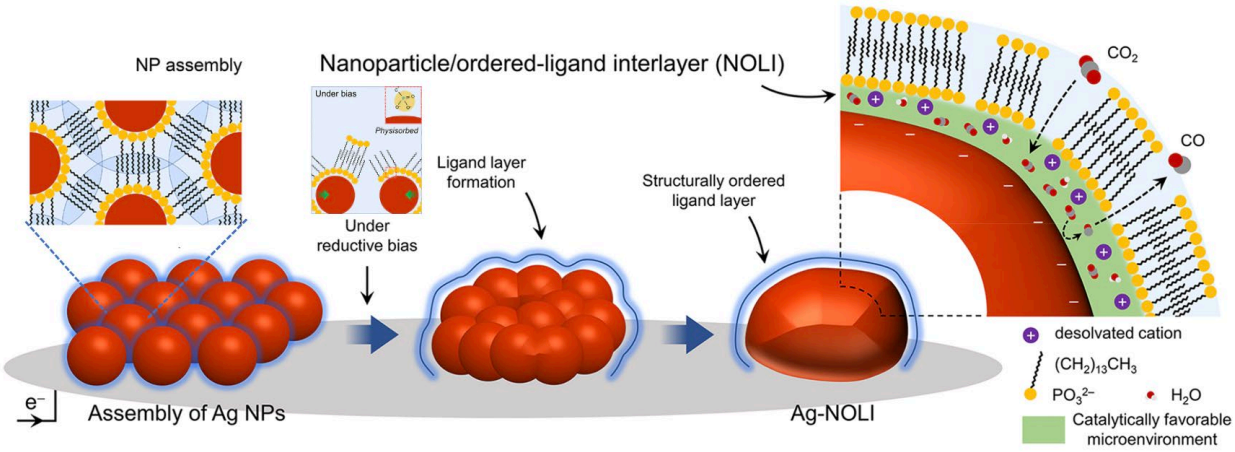

Figure 2.4: Proposed formation mechanism of the nanoparticle-ordered ligand interlayer (NOLI). Ligands (tetradecylphosphonic acid, TDPA) are initially covalently bound to the surfaces of small metal nanoparticles. Under CO_2-reducing electrochemical conditions, the nanoparticles undergo coarsening while the ligands detach from the metal surface and reorganize into an ordered interfacial layer. The resulting structure consists of a metallic nanoparticle core, a confined aqueous region, and an outer ligand layer. Interactions among ligands, ions, and solvent molecules within this confined region create a microenvironment that facilitates low-overpotential CO_2 electroreduction. Figure reproduced with permission from Ref.[81]. Copyright © 2021 American Chemical Society.

2.3 NOLI formation mechanism revealed by nanometer-resolved ligand dynamics

As discussed in Section 2.2, the proposed formation pathway of the NOLI structure critically depends on the behavior of surface-bound ligands under electrochemical bias. Elucidating this

process therefore requires direct observation of ligand configurations as they evolve in response to applied potentials. In addition, the NOLI system exhibits significant structural heterogeneity and undergoes substantial nanoparticle restructuring during electrolysis, particularly following ligand detachment. Capturing these dynamics thus necessitates spatially resolved measurements capable of mapping interfacial changes with nanometer-scale precision. Although experimentally challenging and largely unexplored to date, direct probing of ligand dynamics under electrochemical conditions—with both nanometer spatial resolution comparable to nanoparticle dimensions and sufficient chemical sensitivity—is essential for obtaining molecular-level insight into NOLI formation. Such capabilities are critical for understanding how ligand-mediated microenvironments emerge and, more broadly, for guiding the rational design of nanostructured electrocatalysts.

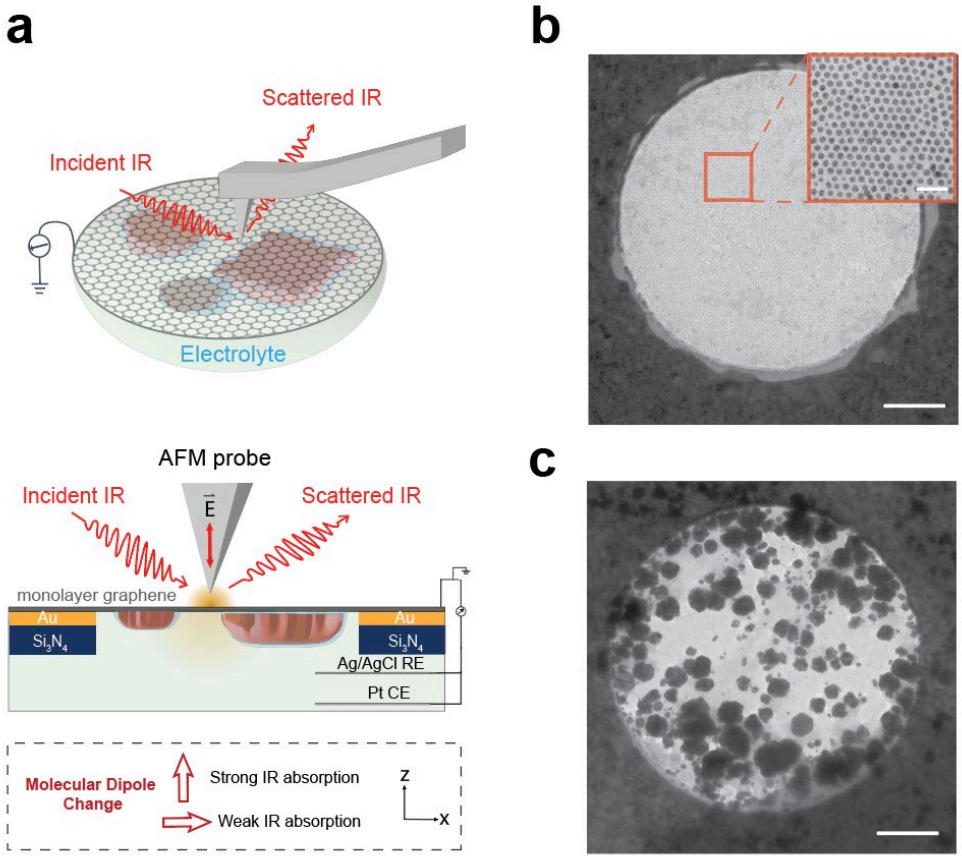

Figure 2.5 *In situ* nano-FTIR setup for probing ligand configuration. a, A schematic of the nano-FTIR experiment. The AFM probe is located over one of the graphene windows suspended across the holes of a perforated 100 nm thick Si_3N_4 membrane (the diameter of the hole is 1 μm and only one hole is shown in this schematic). The single-layer free-standing graphene closing the cell serves both as the working electrode and as the separation between the aqueous environment and the AFM tip, thus preventing tip damage and contamination. The cell is filled with 0.1 M $KHCO_3$ solution saturated with CO_2 and the entire setup is situated in a dry N_2 environment. **b-c,** *Ex situ* transmission electron microscopy (TEM) images of the monolayer Ag NPs drop cast onto the graphene facing the electrolyte (**b**), and their evolved state after the application of negative

bias (**c**). The scale bar is 100 nm in **b** and **c**. The inset in **b** shows the densely packed monolayer particles, with a scale bar of 25 nm.

2.3.1 Nano-FTIR experimental setup

To investigate spatially inhomogeneous chemical processes *in situ* while minimizing radiation damage, vibrational nanospectroscopy with low excitation energy, such as nano-FTIR, are preferable [82-84]. In the experimental setup depicted in Figure. 2.5a, a broadband, spatially coherent synchrotron IR beam is focused onto the metal-coated probe of an atomic force microscope (AFM). The sharp tip acts as an antenna that creates a large enhancement of the IR field near the apex, which decays exponentially with distance, resulting in a high spatial resolution (typically < 20 nm) with surface and chemical sensitivity [82,84]. Furthermore, due to the approximate alignment of the IR near field with the axis of the AFM probe, vibrational modes with dipoles along the same direction are selectively excited. This polarization facilitates the detection of molecular orientation, which can be characterized by changes in the relative peak intensities of vibrational modes [82,85,86]. The recent development of liquid cells with single layer graphene windows that are transparent to photons has facilitated the utilization of nano-FTIR for studying organic molecules under electrochemical conditions [87-90]. In the current experimental configuration, the detection under CO_2 reducing condition and the replication of Ag NP evolution (Figure. 2.5b, c) is achieved, demonstrating the suitability of this platform for investigating the formation of NOLI *in situ*.

2.3.2 Initial binding configuration of ligands probed by *in situ* Nano-FITR

To study the initial binding configuration of ligands, the as-prepared Ag NPs are assembled on the single-layer graphene facing the electrolyte (Figure 2.5b). The corresponding nano-FTIR spectrum under open circuit potential (OCP) is shown in Figure 2.6, revealing multiple peaks around the P-O stretch region that are the IR fingerprint of the tetradecylphosphonic acid (TDPA) ligand used in the synthesis of the NPs. From DFT calculations and previous studies[91-95], the peak around 1039 cm^{-1} can be assigned to the symmetric stretch of P-O ($\boldsymbol{\nu}_s$(P-O)), and the peaks around 1112 cm^{-1} and 1170 cm^{-1} to the asymmetric stretch of P-O ($\boldsymbol{\nu}_{as}$(P-O)) coupled with C-C stretch ($\boldsymbol{\nu}$(C-C)) and with C-H twisting ($\boldsymbol{\tau}$(C-H)), respectively. For simplicity, $\boldsymbol{\nu}_{as}$(P-O) will be used to refer to these two asymmetric modes in the following discussion, while $\boldsymbol{\nu}_s$(P-O) specifically refers to the mode at 1039 cm^{-1}. In addition, the mode at 1305 cm^{-1} belongs to the P=O stretch ($\boldsymbol{\nu}$(P=O)) [92]. The orthogonal vibrations of $\boldsymbol{\nu}_s$(P-O) and $\boldsymbol{\nu}_{as}$ (P-O) are particularly sensitive to the polarization of the IR radiation, which can provide valuable insights into the initial binding structure of the ligand on the Ag surface[96]. Based on the dominant intensities of the $\boldsymbol{\nu}_s$(P-O) mode in the P-O stretch region and the presence of the $\boldsymbol{\nu}$(P=O) mode, it can be concluded that TDPA binds to the Ag surface through a bidentate mode when immersed in the electrolyte. As illustrated in the schematic representation of the modes in Figure 2.6, a bidentate binding structure allows for a dipole moment of the $\boldsymbol{\nu}_s$(P-O) mode along the surface normal, leading to a high nano-FTIR intensity. Under the same configuration, the $\boldsymbol{\nu}_{as}$ (P-O) mode, which has a dipole moment parallel to the surface, exhibits a low intensity. This non-zero intensity comes from the orientation variation of the ligand on the NP surface with large curvature, allowing some coupling with the near field.

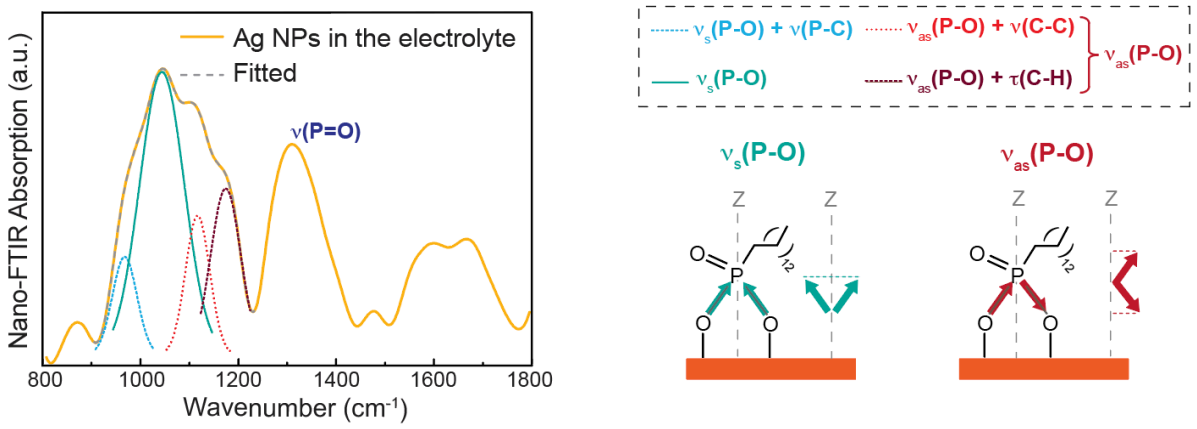

Figure 2.6 Initial binding configuration of ligands on Ag NPs . Nano-FTIR spectrum of Ag NPs inside the cell filled with electrolyte under open circuit condition. The P-O stretch region is composed of four different modes around 962 cm^{-1} (blue, dotted), 1039 cm^{-1} (cyan), 1112 cm^{-1} (red, dotted), and 1170 cm^{-1} (brown, dotted), which correspond to $\boldsymbol{\nu}_s$ (P-O) coupled with $\boldsymbol{\nu}$ (P-C), $\boldsymbol{\nu}_s$ (P-O), $\boldsymbol{\nu}_{as}$ (P-O) coupled with $\boldsymbol{\nu}$ (C-C), and $\boldsymbol{\nu}_{as}$ (P-O) coupled with $\boldsymbol{\tau}$ (C-H), respectively. Schematics of the relative movement of atoms in symmetric and asymmetric modes, as well as the corresponding dipole change projected along the z direction (surface normal) are depicted below the spectrum.

2.3.3 Bias-induced transformation from bidentate to monodentate binding

The structural evolution of ligands on the Ag NPs is revealed by the nano-FTIR line profiles captured under electrochemical conditions (Figure 2.7). Figure. 2.7a displays the image of the integrated near-field IR amplitude scattered from the tip-sample region during scanning over the graphene-covered window and surrounding regions. The corresponding transmission electron microscopy (TEM) image of the same area, acquired after the nano-FTIR experiment, reveals the NP distribution of the evolved state (Figure 2.7 b). While the near-field IR image exhibits a somewhat lower spatial resolution compared to the TEM image, we employ it for localizing the aggregation of nanoparticles during the nano-FTIR experiment. To preserve the integrity and functionality of the TDPA ligand, samples were not exposed to electron beam prior to the nano-FTIR experiments, considering the extreme sensitivity of organic ligands to electron beam radiation [97,98].

Nano-FTIR line profiles under different biases, acquired along the scan direction represented by a red arrow (Figure. 2.7 a, b), are visualized as 3D color maps depicting line scans over which the intensity of nano-FTIR absorption is recorded (Figure 2.7 c-h). All biasing potentials in this section are referenced to the reversible hydrogen electrode (RHE), unless indicated otherwise. At OCP, which is approximately 0.71 V at pH 6.8, the intensity distribution of three P-O stretch modes ($\boldsymbol{\nu}_s$(P-O), $\boldsymbol{\nu}_{as}$(P-O), $\boldsymbol{\nu}$(P=O)) of the phosphonate head group indicates a relatively homogeneous distribution of the as-prepared NPs within the graphene window. When a bias of 0.34 V is applied,

the nano-FTIR line profile (Figure 2.7 d) shows some spatial inhomogeneities, which we attribute to the initial rearrangement of ligands. Interestingly, at -0.06 V, a boost in intensity of the $\boldsymbol{\nu}_{as}$ (P-O) mode is observed, while the spatial inhomogeneity remains similar. At -0.26 V, when the NPs are expected to begin fusing together, the IR line profile becomes highly inhomogeneous, characterized by the augmented localization of the intensity of the $\boldsymbol{\nu}_{as}$ (P-O) mode (Figure 2.7f). Careful comparison between the IR line profile and the TEM image confirms that NPs aggregate and fuse together at positions where the concentrated IR intensity is observed. Upon reduction of the bias, a decay of the $\boldsymbol{\nu}_{as}$ (P-O) mode intensity is observed. To better present the bias-induced intensity change of the $\boldsymbol{\nu}_{as}$(P-O) mode, nano-FTIR spectra taken in a representative position are provided in Figure 2.7i.

The observed changes in the intensities of the $\boldsymbol{\nu}_{as}$ (P-O) mode can be attributed to corresponding structural modifications of TDPA ligands. At a bias of -0.06 V, we propose that the enhanced intensity of the $\boldsymbol{\nu}_{as}$(P-O) mode is attributed to the partial dissociation of Ag-O bonds, indicating a transition from bidentate to monodentate binding configuration of the ligand head group. This structural transformation accounts for the boost in the intensity of $\boldsymbol{\nu}_{as}$(P-O) mode in two ways. Firstly, this transformation releases one O atom with partial negative charges from the surface, drastically augmenting the overall dipole moment of the $\boldsymbol{\nu}_{as}$ (P-O) mode. Secondly, as depicted in Figure 2.7 j, the lifted O atom reorients the ligand structure, increasing the dipole moment projection of $\boldsymbol{\nu}_{as}$ (P-O) mode along the surface normal direction. It is crucial to highlight that alternative factors that might account for the augmented intensity of the $\boldsymbol{\nu}_{as}$ (P-O) mode, such as Localized Surface Plasmon Resonance (LSPR) or an increased concentration of ligands, can be discounted. This is because if these factors were the primary drivers, one would expect a uniform increase in intensity across a broad wavenumber range. However, we only observe the increased intensity exclusively in the $\boldsymbol{\nu}_{as}$ (P-O) mode.

Once the monodentate configuration is formed, the electrostatic interaction between the detached O atom and the negatively charged Ag surface dictates a highly sensitive and dynamic response of the ligand structure to the applied bias. Under -0.26 V, the boosted intensity of $\boldsymbol{\nu}_{as}$(P-O) indicates that the ligand structure remains in the monodentate configuration. However, a greater accumulation of surface charge compared to that under -0.06 V results in a larger separation between the detached O atoms and the Ag surface driven by repulsion. This separation decreases upon gradual retraction of the bias (decrease of the overpotential), explaining the decrease in the intensity of the $\boldsymbol{\nu}_{as}$(P-O) mode when we retract the bias to 0.14 V and 0.54 V, as illustrated in Figure 2.7g-h and Figure 2.7 i.

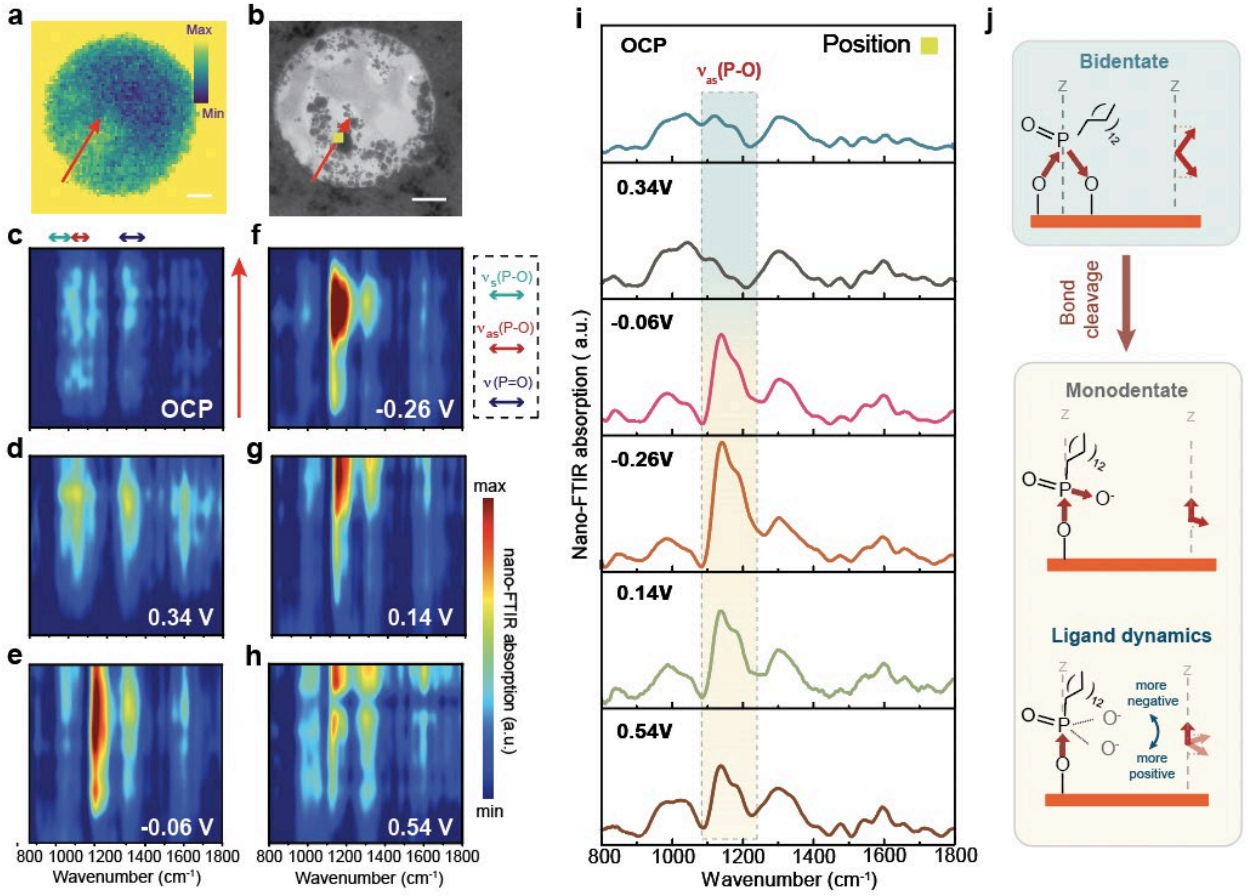

Figure 2.7. Spatially resolved bidentate to monodentate transformation and structural dynamics. a, Images of the total scattered optical amplitude from the suspended graphene with NPs and its surrounding area. The intensity increases when the tip is positioned on the top of the region outside the suspended graphene window because the gold film under the graphene scatters more IR light (scale bar, 100 nm). **b,** Corresponding TEM image of the same area after the nano-FTIR experiment (scale bar, 100nm). **c-h,** Color map representations of the nano-FTIR spectral intensities (arbitrary units in the color scale) from 800 to 1800 cm^{-1} over the Ag NPs under various biases. The ranges for stretching modes of P-O and P=O are indicated. The nano-FTIR profiles were acquired at positions along the red arrows in **a** and **b**. The electrochemical bias was applied in the following manner: OCP→ 0.34 V→ -0.06 V→ -0.26 V→ 0.14 V→ 0.54 V. Each nano-FTIR spectra is collected under a constant potential in 0.1 M $KHCO_3$ (pH 6.8) saturated with 1 atm CO_2. **i,** Stacked nano-FTIR spectra (left panel) under stepped bias collected at the position on the line scan marked by a soft green square in **b**. **j,** The mechanism of intensity variations of the ν_{as}(P-O) mode under different potentials. All the potentials in this figure are referenced to the reversible hydrogen electrode (RHE).

2.3.4 Final ligand detachment leading to NOLI formation

The *in situ* nano-FTIR measurement captures the bias-induced bond cleavage and structural dynamics of the ligands. The high spatial resolution uniquely allows a direct comparison of spectra originating from NPs of varying sizes and evolving statuses, which leads to the conclusion that the bidentate to monodentate transformation occurs universally across all NP surfaces, maintaining consistent ligand structural dynamics irrespective of NP sizes. However, within the bias window stabilizing the monodentate configuration, no evidence suggests the occurrence of CO_2 reduction, and the current nano-FTIR/graphene cell setup suffers from the fragility of the graphene membrane under greater bias (beyond -0.26 V). To circumvent this problem and to capture the final ligand state supporting CO_2 reduction, we use surface enhanced Raman (SERS) to follow the evolution of the molecular structure within NOLI up to more negative bias compared to those currently possible with nano-FTIR. This enables tracking changes of ligand species through the onset of full detachment. The Raman scattering experiments employ a focused laser beam that passes through the electrolyte and is focused on the electrode surface (Figure 2.8a**).** However, SERS is not polarized and hence there is no preferential orientation axis like in nano-FTIR.

The initial state of the ligand on Ag NPs (Figure 2.8b), in electrolyte, is characterized by three main Raman peaks at 540 cm^{-1}, 711 cm^{-1}, and 780 cm^{-1} within the spectral range between 400 and 900 cm^{-1} (Figure 2.8b). The peak at 540 cm^{-1} is assigned to O-P-O wagging (out-of-plane bending) mode of the ligand head group bound to Ag surface, supporting a bidentate ligand configuration on the as-prepared NPs. The C-P stretching mode is located at 780 cm^{-1}, with a shoulder peak at 711 cm^{-1} which is assigned to alkyl C-C bending [92-94]. Upon initial biasing, the O-P-O wagging mode disappears. As predicted and shown in other works, this type of mode can be highly dependent on the binding configuration and even surface geometry, given that the prominent structural change due to the detachment of an O atom can contribute to distinct active modes, supporting that a change in ligand configuration is occurring upon initial biasing [92,93,95]. Meanwhile, the continued appearance of C-P stretches confirms the ligand is still detectable near the surface. Together, this compellingly demonstrates the detachment of first Ag-O bonds and supports the results from nano-FTIR.

Under the same conditions, a dominant peak emerges at 530 cm^{-1}, which belongs to the P-O bending modes (i.e., $\boldsymbol{\delta}$(O-P-O), or $\boldsymbol{\delta}$(C-PO_3)) [95,99]. This mode exhibits a red shift of 10 cm^{-1} compared with the wagging mode of the initial state, which arises from a distinct ligand configuration following the second Ag-O detachment occurring between -0.40 and -0.65 V [92-94]. Under higher bias (-0.40 V and greater, Figure. 2.8b), the sharp peak at 710 cm^{-1} is assigned to CO_3^{2-} bending mode and accompanied by the depletion of the bicarbonate CO-H mode (1042 cm^{-1}). This confirms a change in the pH near the surface that occurs at the onset of CO_2 reduction in the NOLI, in agreement with the onset of Faradaic currents observed by linear sweep voltammetry (LSV) (Figure. 2.8d). As expected, the second detachment prompts interlayer formation, causing substantial changes within the local electrochemical environment, and the onset of efficient CO_2 reduction marked by a change in the reactive species present [80].

Utilizing the C-H_x region, containing asymmetric and symmetric stretching modes (2800 – 3000 cm^{-1}), the bias-induced behavior of the alkyl chains is captured. A peak at 2821 cm^{-1} emerges starting from - 0.40 V (Figure. 2.8c), which remains unreported in many spectroscopic studies focused on alkyl chains and their assemblies[100-102]. Furthermore, the bias-dependent behavior of this mode is reversible, as the peak disappears when the bias is retracted (Figure. 2.8c). Based on

these observations, we propose this peak represents a C-H stretching mode which originates from the presence of solvent molecules situated between alkyl chains. This proposition stems from the understanding that while the ligand layer remains in proximity to the NP after detachment, applying greater bias expands the spatial region that an individual ligand can explore as it is electrostatically repelled from the surface. This process increases the likelihood of water intercalation between the ligand chains and these water molecules would potentially weaken the C-H stretch mode.

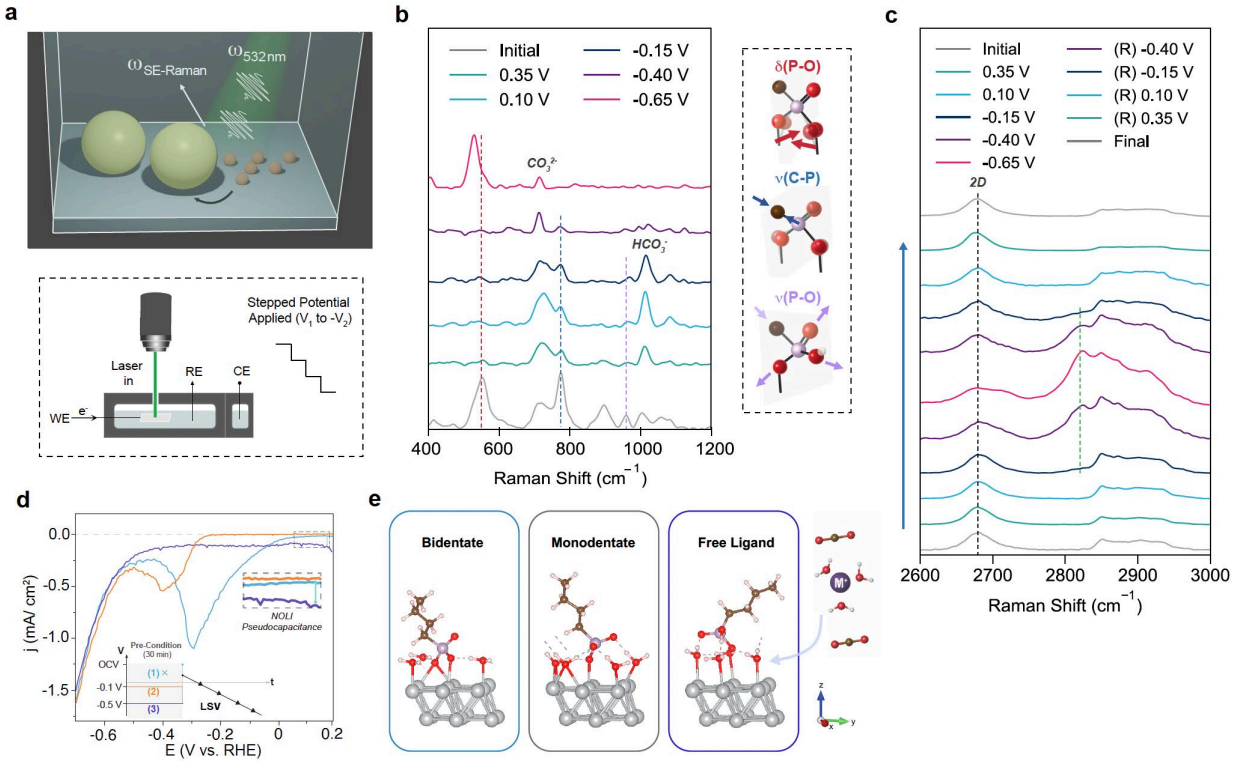

Figure 2.8. Bias-induced second bond cleavage towards formation of the catalytic interlayer. **a,** Simplified schematic of *in situ* Raman spectro-electrochemical set-up conducted in a customized cell. A roughened Ag substrate is used to further boost scattering enhancement and one layer of graphene is transferred onto the surface. Ag NPs are then drop casted onto graphene capped electrodes. **b,** *in situ* Raman spectra from the Ag NPs on the graphene/SERS electrode in 0.1 M $KHCO_3$ (pH 6.8). Illustrations show O-P-O wagging, C-P stretching, and P-O symmetric stretching modes with the C_{14} alkyl chain represented for simplicity by one C atom (brown). Each of these modes is indicated by a dashed line in the left spectra. The remaining peaks at 1007 and 1064 cm^{-1} are assigned to bicarbonate CO-H bend and carbonate symmetric stretching modes, respectively, and carbonate bending at 710 cm^{-1}, from the electrolyte [103]. **c,** *in situ* Raman spectra in the C-H_x region. In the range of 2850 and 2950 cm^{-1}, methylene (-CH_2) and methyl (-CH_3) symmetric and asymmetric stretches appear. The peak at 2825 cm^{-1} appears at greater applied biasing conditions (green dashed line). The presence of a high-quality layer of graphene is confirmed by the presence of graphene's 2D mode around 2680 cm^{-1} (Supplementary Figure 14) [104]. All Raman peak intensities are normalized to this mode. Potentials in **b** and **c** are referenced to

the reversible hydrogen electrode (RHE). **d,** LSV from 0.2 V to -0.7 V of as-prepared Ag NPs without holding (blue) and after holding at -0.1 V (orange), or -0.5 V (purple) for 30 mins. **e,** Optimized structures obtained through DFT calculations (0 V vs. Standard Hydrogen Electrode).

2.3.5 NOLI formation mechanism

In summary, the formation mechanism of the NOLI structure is elucidated through a combination of *in situ* nano-FTIR, *in situ* SERS, and density functional theory (DFT) calculations, which together allow direct monitoring of ligand dynamics under electrochemical bias. Nano-FTIR measurements reveal the initial stages of ligand restructuring with nanometer spatial resolution. Upon application of a cathodic potential, the phosphonic acid ligands bound to the Ag nanoparticle surface undergo a transition from a bidentate to a monodentate binding configuration, corresponding to the cleavage of one Ag–O bond. This transformation increases the dipole moment associated with the P–O vibration and results in the pronounced intensity increase observed in the nano-FTIR spectra. At more negative potentials, SERS measurements capture the subsequent detachment of the remaining Ag–O bond, leading to the formation of free ligands that remain confined near the nanoparticle surface. Concomitantly, changes in the vibrational signatures of the alkyl chains indicate increased conformational flexibility and the intercalation of solvent molecules within the ligand layer. Together, these spectroscopic observations demonstrate that ligand dissociation occurs sequentially under electrochemical bias.

DFT calculations further support this mechanism by confirming the energetic feasibility of the stepwise bond cleavage and the stability of the resulting ligand-mediated interlayer. The combined experimental and theoretical results therefore reveal a dynamic formation process in which electrochemical bias drives progressive ligand detachment and structural reorganization. As illustrated in Figure 2.9, the NOLI interlayer emerges through a sequence of events:

1. Initial bidentate ligand binding on the nanoparticle surface;

2. Partial dissociation to a monodentate configuration under mild cathodic bias;

3. Complete detachment of the ligand head group at more negative potentials, producing a confined ligand layer adjacent to the nanoparticle surface.

This process generates a unique interfacial microenvironment in which ligands, solvent molecules, and electrolyte ions coexist in close proximity to the catalytic surface. The resulting confined environment modulates the local electric field and facilitates favorable non-covalent interactions among CO_2, cations, solvent molecules, and ligands.

These findings provide a molecular-level understanding of how the NOLI architecture forms under electrochemical conditions and establish a direct link between electrochemical bias, ligand dynamics, and microenvironment formation. Despite this mechanistic insight into NOLI formation, the manner in which this ligand-modulated interfacial structure promotes low-overpotential CO_2 reduction remains unclear. This question is addressed in the following section, where we investigate how the NOLI microenvironment influences cation solvation and reaction energetics.

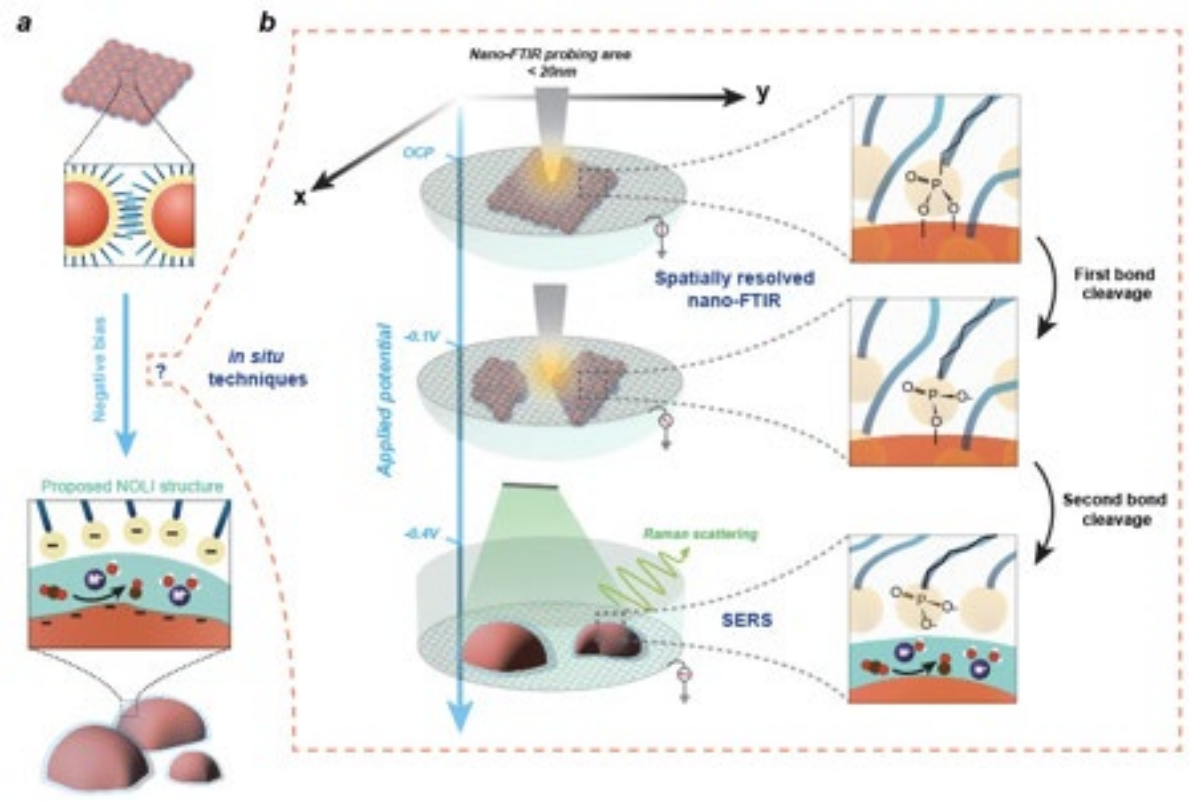

Figure 2.9. Real-time molecular picture of microenvironment formation probed by *in situ* nano-FTIR and SERS. a, The proposed initial and final states during NOLI formation. **b**, Probed NOLI formation mechanism. Under low overpotential, *in situ* nanometer-resolved nano-FTIR reveals the cleavage of one of the P-O-Ag bonds on the aggregating NPs. Meanwhile, the second P-O-Ag bond cleavage is observed by *in situ* SERS under high overpotentials. This combination uncovers a consecutive bond cleavage mechanism that promotes the formation of favorable noncovalent interactions between CO_2, cations, solvent, and ligands, which are responsible for the high catalytic activity of NOLI (C, brown; cation, purple; O, red; H, grey; ligand head group, yellow; ligand alkyl chains, blue; aqueous interlayer, cyan).

2.4 Ligand-assisted cation desolvation promotes CO_2R at low overpotential.

As demonstrated in Section 2.3, electrochemical restructuring of ligand-capped nanoparticles gives rise to the NOLI architecture. While these experiments reveal how the NOLI structure forms under electrochemical bias, they do not yet explain how this interfacial architecture promotes CO_2 reduction at unusually low overpotentials. Addressing this question requires understanding how

the NOLI framework modifies the electrochemical microenvironment surrounding the catalytic surface.

Beyond the ligand scaffold itself, the interfacial microenvironment involves multiple components—including electrolyte cations, anions, interfacial water molecules, and their interactions with reaction intermediates. The structure and dynamics of these species can strongly influence both the energetics and kinetics of CO_2 activation, particularly through solvation effects and ion–intermediate interactions. Probing these processes therefore requires techniques capable of resolving interfacial species under operating electrochemical conditions.

In this section, we employ a combination of *in situ* surface-enhanced infrared absorption spectroscopy (SEIRAS) and surface-sensitive total electron yield X-ray absorption spectroscopy (TEY-XAS) to directly probe the interfacial environment in NOLI systems. These measurements provide insight into cation solvation structure, ion accumulation within the ligand-defined pocket, and their interactions with CO_2 reduction intermediates. As will be shown, these phenomena collectively reveal how the NOLI architecture promotes CO_2 activation at low overpotentials. Moreover, the mechanistic insights gained here—particularly regarding cation desolvation and interfacial ion crowding—may extend beyond NOLI systems and provide a broader framework for understanding microenvironment effects in electrocatalysis.

2.4.1 Ligand-modulated ionic environment facilitates CO_2 activation.

To elucidate how the NOLI architecture promotes CO_2 reduction at low overpotentials, *in situ* ATR-SEIRAS measurements were performed using 0.1 M $CsHCO_3$ as the electrolyte. The schematic of the *in situ* ATR-SEIRAS cell is shown in Figure 2.10. Prior to spectral collection, the electrode was preconditioned by a linear sweep voltammetry (LSV) from open-circuit potential (OCV, around 0.6V_{RHE}) to –0.8 V_{RHE}, followed by stabilization at –0.8 V_{RHE} for at least 10 minutes. This preconditioning step induces ligand detachment and the aggregation of small Ag nanoparticles into larger polycrystalline domains, establishing the NOLI structure (Figure 2.4, 2.9)

After NOLI formation, the electrode was rested at OCV for 30 minutes under continuous CO_2 bubbling to remove surface-adsorbed species formed during preconditioning. The IR spectrum at this state was used as a reference for all subsequent spectra. Figure 2.11a and b present SEIRAS spectra of the fingerprint region (1200–2200 cm^{-1}) and water stretch region (3000–3800 cm^{-1}) under increasingly negative biases. A feature at 1372 cm^{-1} emerges around 0.4 V_{RHE}, reaches maximum intensity near 0.1 V_{RHE}, and then gradually decreases with further negative bias, disappearing entirely around –0.2 V_{RHE}, while shifting slightly to 1362 cm^{-1}. Following the disappearance of this feature, a new peak around 1846 cm^{-1} appears, accompanied by an increasingly negative band at 1232 cm^{-1}. Based on our previous work[79], the 1232 cm^{-1} band is assigned to the ν(P=O) vibration of tetradecylphosphonic acid (TDPA) ligands, where the negative signal indicates ligands moving further away from the Ag surface.

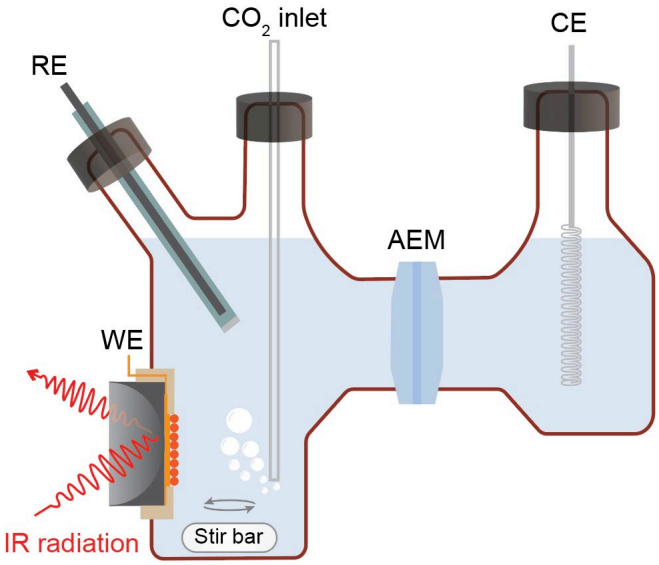

Figure 2.10. Schematic of the *in situ* ATR-SEIRAS electrochemical cell. The working electrode (WE) is mounted on the side wall of the cell. An anion exchange membrane (AEM) separates the working and counter electrode compartments. CO_2 is continuously bubbled into the working compartment, while a magnetic stir bar provides agitation to enhance mass transport. RE and CE denote the reference and counter electrodes, respectively.

Additionally, a peak around 1990 cm^{-1} is observed from –0.4 V_{RHE} to –0.8 V_{RHE}, shifting to lower wavenumbers as the bias becomes more negative. By –0.8 V, the 1846 cm^{-1} and 1990 cm^{-1} features shift to 1804 cm^{-1} and 1966 cm^{-1}, respectively. The observed Stark shifting behavior strongly suggests that these modes correspond to surface-adsorbed species. We assign these two modes to bridge-adsorbed (*CO_B) and linearly adsorbed (*CO_L) CO species, respectively, which aligns well with literature reported IR frequencies of CO adsorbed on Ag surfaces[105-107]. Notably, bridge-bonded *CO is typically favored at low CO coverage on Ag, while *CO_L becomes dominant at higher coverage[108], consistent with our observation that the 1846 cm^{-1} feature appears first at lower overpotentials. This behavior rules out the possibility of *CO adsorbed on Pt—a common source of contamination in SEIRAS—since Pt favors atop-bound CO at low coverages[109-111]. Although both bridge- and linear-bound CO species are observed, CO-induced site blocking is unlikely under the present conditions. CO is generated only *in situ* at very low partial pressures (~6×10^{-4} atm), far below the regime where competitive CO/CO_2 adsorption has been reported[112].

The nature of the 1372 cm^{-1} feature was further investigated. Given the potential-dependent shift of this vibrational mode, it is most likely associated with a surface-bound species. While vibrational modes associated with (bi)carbonate species are commonly observed in this spectral region[113], such an assignment appears unlikely in our system. Adsorbed *HCO_3^-/*CO_3^{2-} would be expected to detach under increasingly negative potentials, leading to a progressively negative peak rather than the observed buildup and decay. To probe whether this feature involves hydrogen, ATR-SEIRAS measurements were repeated in 0.1 M $CsDCO_3$ (in D_2O), as vibrational modes involving hydrogen typically experience redshift when hydrogen is replaced by deuterium[57]. No significant shift was observed in the D_2O spectra (Figure 2.11 c), indicating that the 1362 cm^{-1} mode does not

involve hydrogen. Given that the appearance and disappearance of this feature coincide with the emergence of *CO adsorption, we propose that the 1362 cm^{-1} band corresponds to the symmetric O–C–O stretch (ν_s(O–C–O)) of an adsorbed CO_2 intermediate. The asymmetric stretch, typically expected around 1500 cm^{-1}, is not observed due to the surface selection rules of SEIRAS[57,114,115]. Importantly, adsorption of CO_2 on metal surfaces requires activation of the linear molecule through bending, which lifts the degeneracy of the $2\pi_u$ LUMO and enables hybridization with metal states. This interaction necessarily involves partial electron transfer from the metal into the CO_2 antibonding orbital, yielding a bent adsorbate with partial negative charge[54,56]. Therefore, the observed 1372 cm^{-1} feature is less likely to correspond to a charge-neutral adsorbed CO_2 species. Instead, we assign it to (partially) reduced CO_2, denoted $*CO_2^-$ or activated CO_2 in the following discussion.

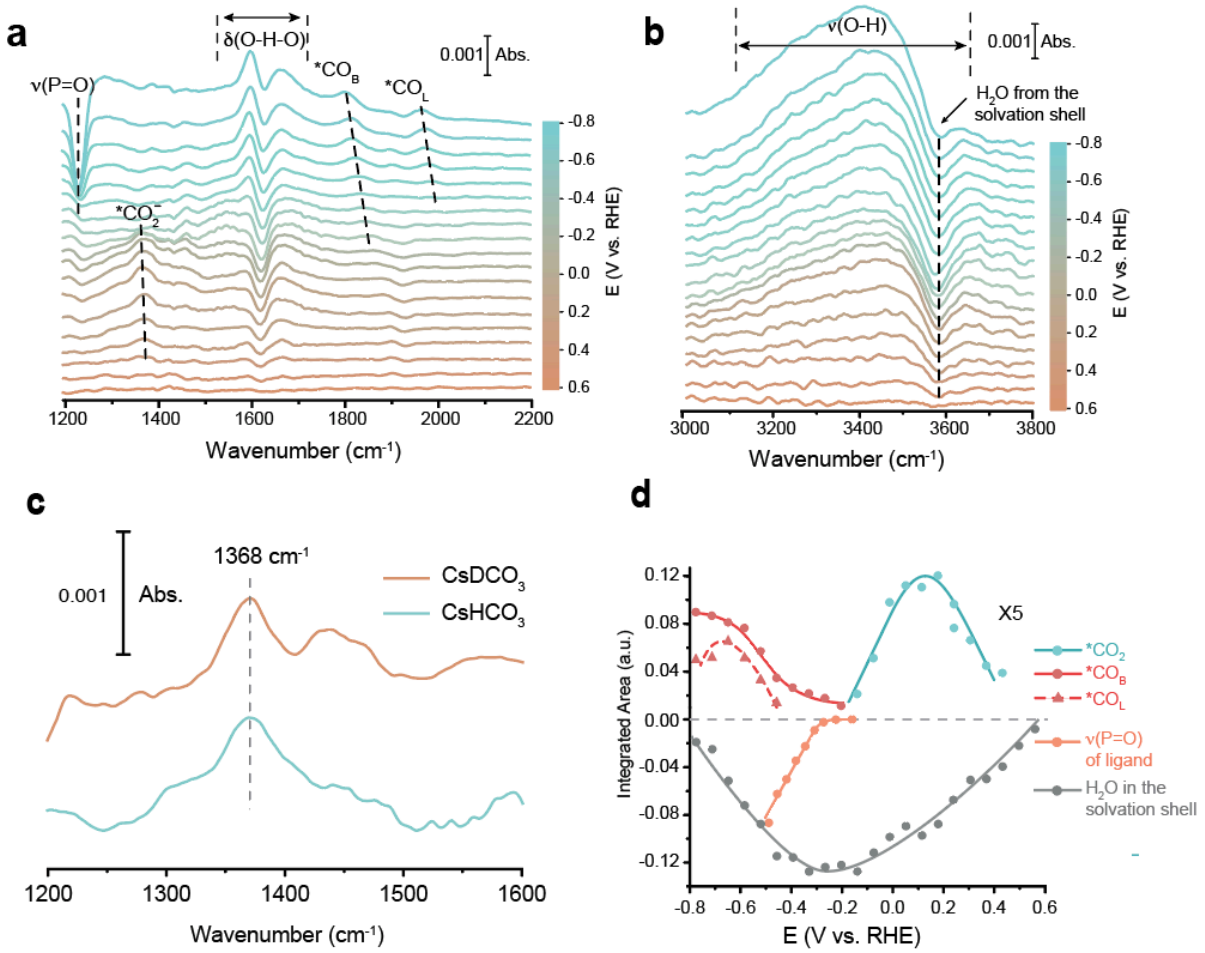

Figure 2.11 ***In situ*** **ATR-SEIRAS spectra of Ag NOLI**. **a-b** *In situ* ATR-SEIRAS spectra collected from 1200–2200 cm^{-1} (**a**) and 3000–3800 cm^{-1} (**b**) regions for Ag NOLI. Spectra were acquired under applied potentials ranging from 0.6 V_{RHE} to –0.8 V_{RHE} in CO_2-bubbled 0.1 M $CsHCO_3$, referenced to a spectrum collected at 0.6 V_{RHE}. **c**, Comparison of ATR-SEIRAS spectra of Ag NOLI in H_2O and D_2O. Spectra were collected at 0.2 V_{RHE} in 0.1 M $CsHCO_3$ (for H_2O) and 0.1 M $CsDCO_3$ (for D_2O), with the reference spectrum acquired at OCV after 30 minutes of

continuous CO_2 bubbling. **d**, Integrated absorbance of interfacial species identified in panels **c** and **d** as a function of potential. Positive areas are magnified fivefold for clarity.

In addition to carbon-related intermediates, changes in water-related modes were also observed. In the fingerprint region (Figure 2.11a), the H–O–H bending mode shows a negative feature around 1620 cm^{-1} that becomes more prominent under negative biases. New features at 1600 cm^{-1} and 1660 cm^{-1} gradually build up as the potential becomes more negative. In the OH stretching region (Figure 2.11b), the negative band at 3580 cm^{-1} becomes more intense at moderate biases and then partially recovers at higher negative potentials, accompanied by intensity increases at 3200–3400 cm^{-1}. The synchronous evolution of the 1620 and 3580 cm^{-1} features suggests they belong to the same water species. Therefore, these bands are assigned to water molecules tightly associated with the solvation shell of cations, which is consistent with multiple spectroscopic studies on interfacial water structure[70,72,116].

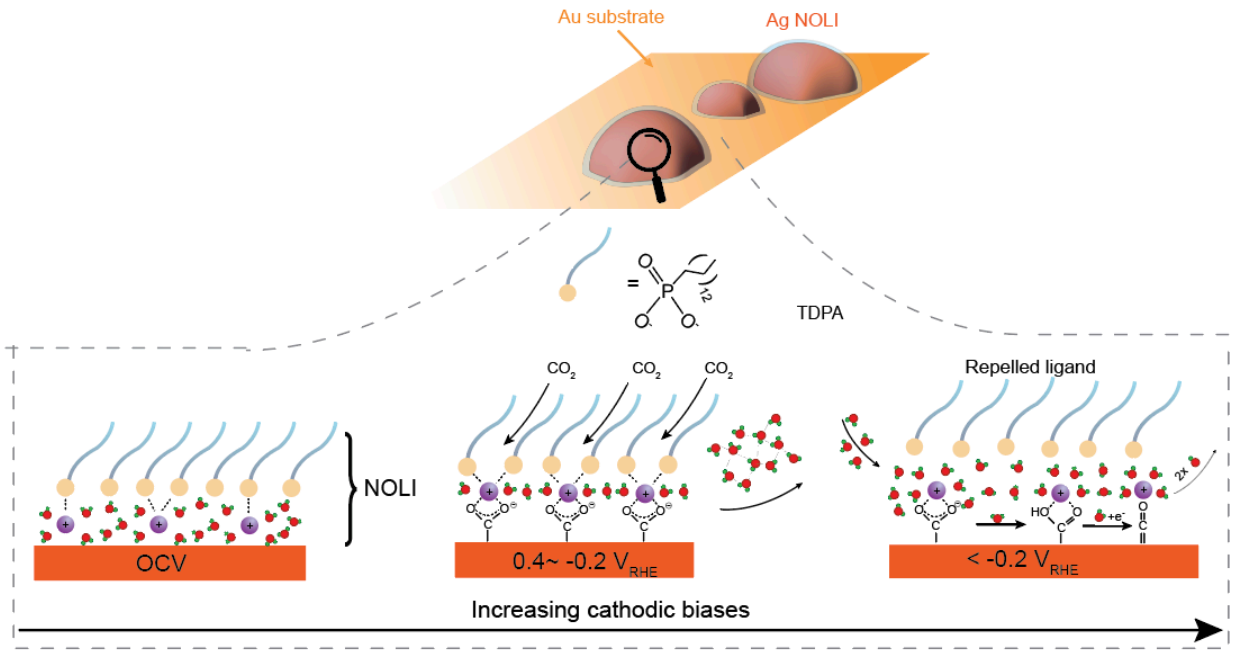

Figure 2.12. A schematic of interfacial processes occurring at different biases for Ag NOLI. The TDPA ligand is depicted as a light-yellow ball (phosphonic acid headgroup) linked to a cyan chain (14-carbon alkyl chain). Cs^+ ions are shown as purple spheres with a central plus sign. Water molecules are represented by a red sphere (oxygen) and two green spheres (hydrogen). For clarity, species outside the ligand layer and minor components (e.g., anions) are omitted.

The integrated band intensities of the vibrational modes detected in Figure 2.11a and b at different applied potentials are summarized in Figure 2.11d. In addition, the interfacial processes probed by *in situ* SEIRAS are proposed as a schematic in Figure 2.12. In the potential window from OCV to –0.2 V_{RHE}, the increasing negative area associated with H_2O in the cation solvation shell with increasingly negative potentials indicates progressive cation desolvation, i.e., reduction of the

number of water molecules coordinated to the cation. Interestingly, activated *CO_2 is also observed within this same potential window, notably more positive than the potentials typically reported for *CO_2 activation on Cu[57,117]. The simultaneous occurrence of these two phenomena suggests that CO_2 activation at such low overpotentials is facilitated by desolvated cations. As illustrated schematically in Figure 2.12, within this potential range, *CO_2 molecules replace the H_2O molecules originally present in the cation solvation shell. The displaced water molecules reorganize into a bulk-like phase with a strong hydrogen-bond network, which explains the intensity increase observed between 3200–3400 cm^{-1} in Figure 2.11b—a spectral signature characteristic of strongly hydrogen-bonded, bulk-like water.

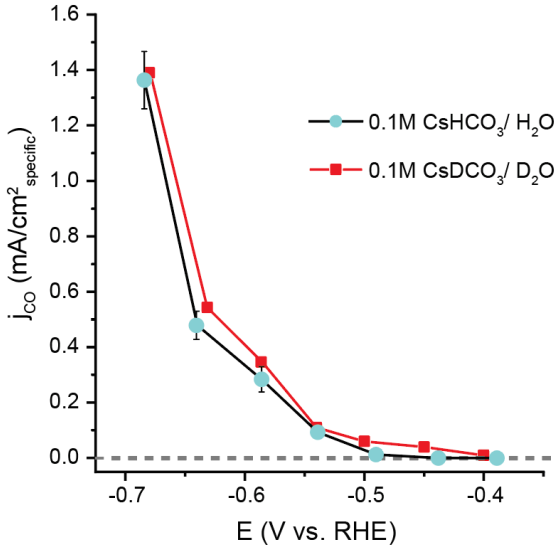

Figure 2.13. Specific CO partial current density as a function of potential for Ag NOLI measured in CO_2-saturated 0.1 M $CsHCO_3$ and 0.1 M $CsDCO_3$ electrolytes. The nearly identical trends indicate that proton transfer is not involved in the rate-limiting step of CO formation.

Notably, *CO species only appear when the applied potential becomes more negative than –0.2 V_{RHE}, coinciding with the disappearance of the *CO_2^- signal (Figure 2.11d). This observation suggests that the rate-determining step (RDS) for CO formation is the generation of *CO_2^- via the first electron-transfer activation step, rather than the subsequent conversion of *CO_2^- to *CO. Interestingly, the emergence of *CO also coincides with the recovery of water-related vibrational bands (Figure 2.11d), which might initially imply that protons or water molecules participate in the RDS. However, as shown in Figure 2.13, the CO partial current density (j_{CO}) is nearly identical in both deuterated and protic electrolytes, indicating that proton transfer does not contribute to the rate-determining step. Together, these findings support a mechanism in which CO_2 activation proceeds via an electron-transfer-coupled adsorption step facilitated by desolvated cations:

$$CO_2 + * + M^+ + e^- \rightarrow *CO_2^- \cdots M^+$$

which constitutes the RDS for CO formation. The observed recovery of water-related signals is therefore attributed to further ligand detachment at –0.2 V_{RHE} or more negative potentials, which

enables increased water access to the interfacial region, rather than indicating a direct role of water in the RDS of *CO formation.

To elucidate the origin of the promotion effect of CO_2 activation in the NOLI architecture, SEIRAS spectra were also collected for a ligand-free Ag film. As shown in Figure 2.14a and b, under negative bias, the negative band associated with H_2O stretching is nearly absent, indicating that the interfacial cations remain more solvated than in the NOLI system under equivalent potentials. Moreover, no discernible $*CO_2$-related features appear across the scanned potential range, likely due to lower $*CO_2^-$ surface coverage compared to Ag NOLI. Consequently, the onset potentials for both $*CO_B$ and $*CO_L$ species on the Ag film are at least 250 mV more negative than those observed in Ag NOLI. This comparison highlights that CO_2 activation is significantly facilitated by desolvated cations within the NOLI architecture.

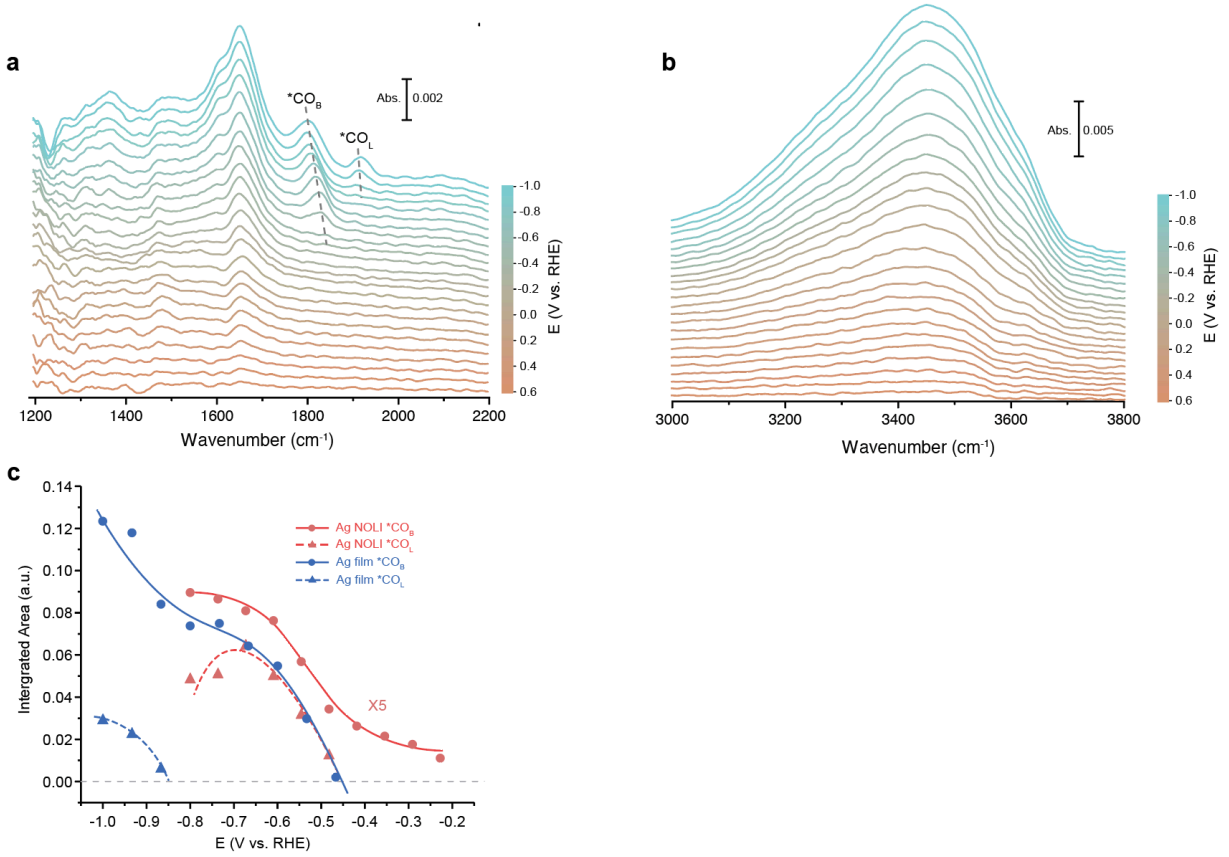

Figure 2.14. *In situ* ATR-SEIRAS spectra of a ligand-free Ag film in CO_2-saturated 0.1 M $CsHCO_3$. a, Spectra in the 1200–2200 cm^{-1} region and **b,** the 3000–3800 cm^{-1} region were collected during a linear sweep voltammetry scan from 0.6 V_{RHE} to –0.8 V_{RHE}, referenced to the spectrum at 0.6 V. **c**, Integrated intensities of $*CO_B$ and CO_L bands as a function of potential for both Ag film and Ag NOLI. Ag NOLI data are reproduced from Figure 2.11a for comparison.

Results from *in situ* SEIRAS measurements clearly reveal the promotional role of desolvated cations in facilitating $*CO_2$ activation in Ag NOLI catalysts. As discussed in Section 1.5.2, cation–intermediate interactions can influence electrochemical reactions through two distinct mechanisms:

a mean-field electrostatic effect, in which accumulated cations modify the interfacial electric field, or specific cation–intermediate interactions, where cations directly stabilize adsorbed reaction intermediates. To distinguish between these possibilities, we examined the Stark tuning behavior of adsorbed $*CO_L$ to assess the interfacial electric field of Ag NOLI. As shown in Figure 2.15, within the potential range where $*CO_2^-$ is observed (0.4 V_{RHE} to –0.2 V_{RHE}), the vibrational Stark tuning rate of $*CO_L$ is approximately 8 cm^{-1} V^{-1}, which is substantially smaller than the ~30 cm^{-1} V^{-1} typically reported for *CO on metal films[117-120]. This comparison indicates that the local electric field in this potential window is relatively modest and allows us to exclude mechanisms based solely on amplified interfacial electric fields. Instead, these results point toward a mechanism in which direct interactions between desolvated Cs^+ ions and adsorbed $*CO_2^-$ intermediates play a decisive role in promoting this activation—a hypothesis that will be further examined in the following sections.

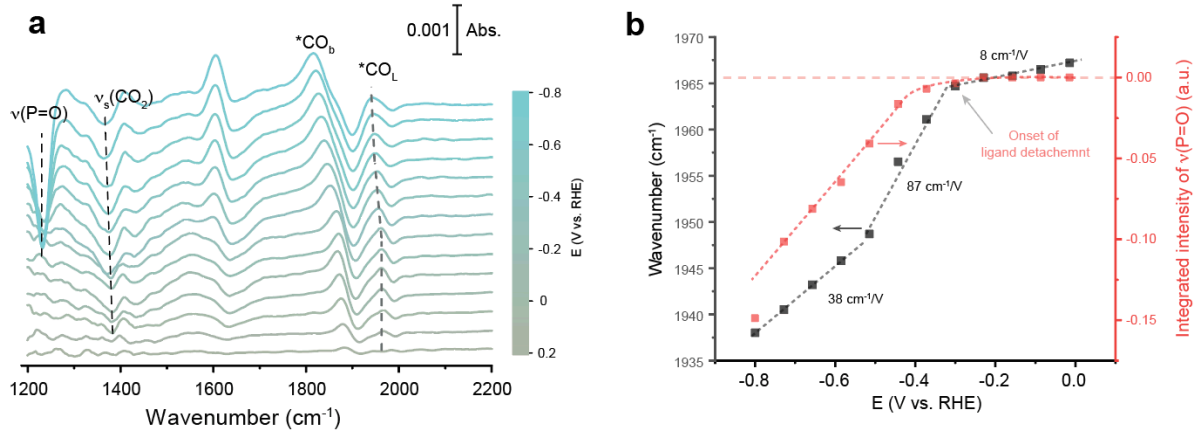

Figure 2.15 Stark tunning rate of Ag NOLI at different bias windows. **a,** *in situ* SEIRAS spectra of Ag NOLI collected from –0.2 V_{RHE} to –0.8 V_{RHE} in 0.1 M $CsHCO_3$. The reference spectrum was collected at 0.4 V_{RHE}. Spectra were recorded after preconditioning the electrodes by a linear sweep voltammetry (LSV) from open-circuit potential (OCV) to –0.8 V_{RHE}, followed by stabilization at –0.8 V_{RHE} for at least 10 minutes to ensure complete NOLI formation and establish a stable *CO coverage. **b**, Wavenumber of $*CO_L$ on Ag as a function of applied potential. Linear fits are indicated by black dashed lines, with the corresponding slopes annotated. In b, red points indicate the integrated intensity of ν(P=O), with the red dashed line serving as a visual guide.

2.4.2 Interactions within the water-deficient NOLI pocket

To elucidate the interactions between desolvated Cs^+ and interfacial species in Ag-NOLI, *in situ* X-ray absorption spectroscopy (XAS) was employed. Interface-sensitive information was obtained using total electron yield (TEY) detection. Figure. 2.16a schematically illustrates the liquid flow cell configuration used for the XAS measurements in this study. In this liquid-cell geometry, X-ray absorption at the solid–liquid interface creates a core hole. Core-hole relaxation generates Auger electrons, whose kinetic energies are determined by atomic energy levels. These Auger

electrons undergo inelastic scattering in the surrounding aqueous medium and generate cascades of low-energy secondary electrons[121]. Owing to the short mean free path of these electrons in aqueous media, only those generated within a few nanometers of the electrode can reach the conductive surface and be collected as a photoinduced current before recombining with ionized species in the electrolyte[122,123]. This photoinduced current (the TEY signal) follows the X-ray absorption cross section and is used to reconstruct the XAS spectra.

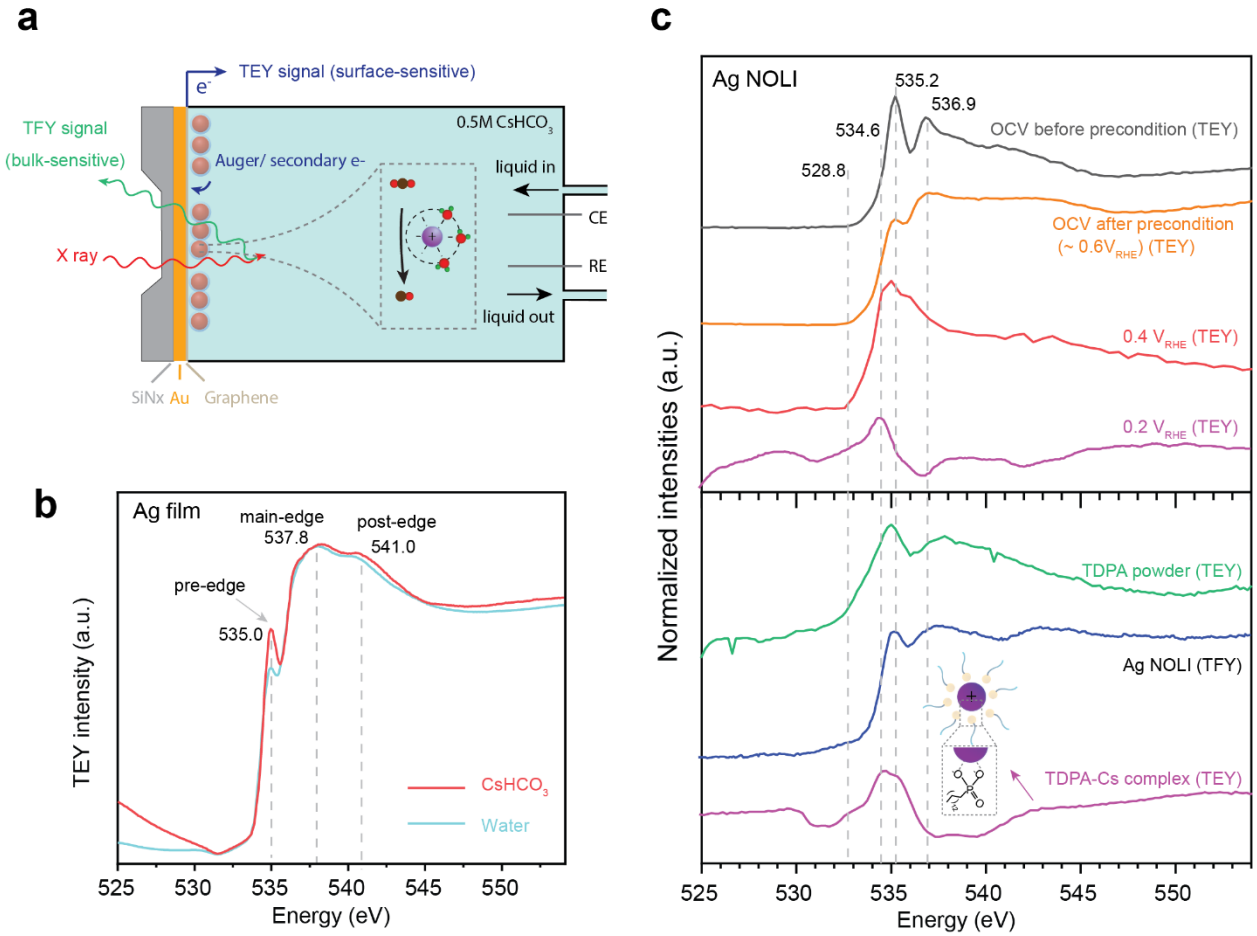

Figure 2.16: O K-edge spectra measured by TEY-XAS. **a**, Schematic of the custom-built liquid flow X-ray cell. A silicon nitride window is coated with thin layers of chromium and gold to ensure good electrical conductivity. Three layers of graphene are subsequently deposited onto the gold to prevent electronic interference from the metal substrate. The catalyst is then drop-cast or coated onto the graphene surface. Measurements are performed under continuous liquid flow, with a 3 M Ag/AgCl electrode and a platinum wire serving as the reference and counter electrodes, respectively. **b–c**, Electron yield O K-edge spectra of (**b**) Ag film in H_2O and CO_2-saturated 0.5 M $CsHCO_3$, (**c**) Ag NOLI at different applied potentials in CO_2-saturated 0.5 M $CsHCO_3$, and reference samples. The reference spectra include TDPA powder (green trace) and Cs–TDPA complexes dissolved in ethanol (red trace, with solvent background subtracted).

We first focus on the oxygen K-edge XAS spectra, as it is well-established for characterizing aqueous systems[124,125]. In condensed phases, water typically exhibits three distinct spectral features:

a pre-edge near 535.0 eV, a main edge near 537.5 eV, and a post-edge near 541.0 eV. The pre-edge intensity scales with the asymmetry in local molecular environment, while the post-edge scales with the number of H-bonds[126-129]. For example, liquid water displays a strong pre-edge and subtle post-edge, while ice shows a more subtle pre-edge and more pronounced post-edge. As shown in Figure. 2.16b, the interfacial water structure near a thin silver film exhibits minimal changes from pure water to 0.5 M $CsHCO_3$; only a slight increase in the pre-edge intensity is observed, likely due to the structure-breaking nature of Cs^+ cations[58]. In contrast, Ag NOLI displays markedly different behavior (Figure. 2.16c). Before preconditioning, when ligands are covalently attached to the Ag surface, water is excluded from the surface by the hydrophobic alkyl chains of the ligands. In this initial state, the phosphonic acid headgroup is expected to be the only oxygen-containing species detectable near the surface. Indeed, the absence of interfacial water at OCV is evident from the spectrum, which shows a strong peak at 535.2 eV and a weaker second peak at 536.9 eV, an intensity trend that is opposite to that of water. We assign this spectrum to TDPA molecules chemisorbed onto the Ag nanoparticle surface via a bidentate configuration[79]. Dry TDPA powder exhibits a similar spectrum; minor differences can be ascribed to the different protonation state of the headgroup[130].

After applying a bias of –0.8 V_{RHE} for 10 minutes to induce NOLI formation and then returning to OCV (around 0.6 V_{RHE}), the oxygen K-edge XAS spectrum changes drastically to resemble that of water, indicating the formation of an aqueous pocket at the interface (Figure. 2.16c) after preconditioning. Upon applying a potential of 0.4 V_{RHE} —close to the onset of $*CO_2^-$ adsorption as shown in Figure 2.11d—the O K-edge spectrum undergoes another dramatic shift, reverting to a shape similar to that of pure TDPA. Almost no intensity remains near water's main and post-edge features, indicating that a significant amount of the water previously confined within the NOLI pockets at OCV has been expelled further from the surface at 0.4 V_{RHE}, leading to the formation of a highly water-deficient environment populated by desolvated Cs^+ cations. This observation is consistent with SEIRAS measurements, where the OH stretching bands show negative features under 0.4 V_{RHE}. The highly ionic environment decreases the Debye length and rapidly screens the negative charge at the interface, allowing the ligands to settle closer to the surface. Compared to chemisorbed TDPA (the OCV spectrum before precondition), the peak maximum at 0.4 V_{RHE} appears slightly red-shifted. A similar red-shift has been observed in first-principles XAS simulations for the protonation of sulfate species[131], leading us to propose that protonation of the phosphonic acid headgroup following ligand detachment is responsible for the red-shift observed here[79], although contributions from interactions with other interfacial species cannot be ruled out.

When applying an even more negative bias of 0.2 V_{RHE}, a more water-deficient spectrum is obtained. Interestingly, the peak maximum continues to red-shift, and a new broad pre-peak emerges at ~528.8 eV—a feature that is absent in both pure TDPA and pure water spectra. To further investigate this signature, we prepared a Cs-TDPA compound where oxygen atoms of the phosphonic acid headgroup are interacting with a Cs cation (Figure. 2.16c). The spectrum of this compound matches well with that of the 0.2 V_{RHE} spectrum, with a pronounced shoulder around 528.8 eV (Figure. 2.16c), This finding suggests a direct interaction between the TDPA head group and Cs^+ at 0.2 V_{RHE}.

Together, the *in situ* XAS and ATR-SEIRAS results demonstrate that under moderate bias, the NOLI pocket becomes a highly confined, water-deficient interfacial environment dominated by desolvated cations, detached ligands, and surface intermediates. In this microenvironment, Cs^+ not

only sheds its hydration shell but also directly interacts with detached ligands. However, O K-edge spectra alone do not provide direct information on Cs–intermediate interactions. To probe these interactions, we next turned to *in situ* XAS at the Cs M-edge.

2.4.3 Interpretation of Cs M edge spectra

Recent work has demonstrated that *in situ* XAS at alkali-metal edges can directly capture electronic structure changes of cations induced by interactions with adsorbed reaction intermediates[63], motivating the use of Cs M-edge XAS to directly interrogate Cs–intermediate coupling under operando CO_2 reduction conditions. To develop a fundamental understanding of the behavior of the largely unexplored Cs M-edges, we first measured several relevant reference samples. Figure. 2.17a presents the Cs M_4 and M_5 edges of solid-state Cs_2CO_3, $CsHCO_3$, and CsI. These absorption features arise from electronic transitions from the 3d core level to the unoccupied 4f orbitals, with the two main absorption edges resulting from spin–orbit coupling of the 3d core hole. Interestingly, additional satellite features are observed at relatively higher energies—specifically at ~742.5 eV and ~757.0 eV. The intensity of these satellite features is highest in Cs_2CO_3, weaker in $CsHCO_3$, and barely visible in CsI.

A similar trend has been reported by Osaka et al., who observed prominent satellite structures in vermiculite (a mineral containing Cs and O), but much weaker features in cesium halides[132]. They attributed the appearance of these satellites to the formation of delocalized 4f orbitals via hybridization between Cs 4f and anion orbitals. While Cs 4f orbitals exhibit minimal overlap with halide orbitals, they strongly interact with O 2p orbitals, explaining the more pronounced tail structures in oxygen-containing compounds. Notably, comparable behavior has also been observed in M-edge spectra of lanthanide oxides, where similar satellite features arise from hybridization between lanthanide 4f orbitals and O 2p orbitals[133]. Together, these findings suggest that the satellite intensities in our Cs M-edge spectra reflect the degree of orbital mixing between Cs 4f and neighboring anion orbitals. In addition, they also indicate that beyond the pure electrostatic effect, Cs and O form a partial covalent bond in $CsHCO_3$ and Cs_2CO_3.

Although the M-edge tail structure provides insight into the local coordination environment of the unoccupied 4f orbitals, the 4f orbitals in Cs^+ are largely empty in the ground state. To assess whether Cs M-edge features reflect broader ground-state interactions, we therefore combined density of states (DOS) calculation, Bader charge analysis, differential charge density ($\Delta\rho$), and electron localization function (ELF) calculations for Cs_2CO_3, $CsHCO_3$, and CsI. As shown in Figure. 2.17b, the density of states (DOS) reveals that Cs 5s and 5p orbitals lie within the energy ranges of –20 to –25 eV and –5 to –10 eV, respectively. In CsI, no orbital overlap is observed, and orbitals show no dispersion, indicating purely ionic interactions between Cs and I. In contrast, both Cs_2CO_3 and $CsHCO_3$ show clear overlap between Cs 5p and O 2p orbitals, with a significant dispersion of the Cs 5p DOS with a width of more than 2.5 eV, indicating partial covalent bonding between Cs and O.

This is further supported by Bader charge analysis, differential charge density and ELF in Figure 2.18: in CsI, the Cs Bader charge approaches its formal ionic value, indicating nearly complete charge separation. In $CsHCO_3$ the Cs positive charge is slightly reduced and even more so in Cs_2CO_3, evidencing partial electron density redistribution toward Cs. Carbonate and bicarbonate phases display directional electron depletion near O and accumulation along the Cs–O axis and

partially toward Cs, forming a polarized bridge region; CsI lacks any continuous accumulation between Cs and I, retaining spherical, isolated ionic basins. For ELF slices, along Cs–I, the inter-nuclear gap maintains a uniformly low ELF baseline (<0.30) with no mid-segment basin. In Cs_2CO_3 and $CsHCO_3$, after excluding near-nuclear regions, an extended intermediate ELF plateau (~0.30–0.35) develops along the Cs–O corridor; the corridor area fraction with ELF > 0.30 is markedly larger (Cs_2CO_3 ≈ 0.460; $CsHCO_3$ ≈ 0.419; CsI ≈ 0.000; Figure 2.16c). This plateau is well below the high ELF values (≈0.7–0.9) characteristic of strong covalent bonds, but it reveals directional polarization and weak p–p co-localization—a polarized partial-covalent character unique to Cs–O in these lattices. Taken together, the significant Cs 5p–O 2p DOS overlap and dispersion, the dipolar Δρ redistribution, the reduced (less ionic) Bader charge on Cs, and the intermediate ELF plateau collectively rationalize the presence of the M-edge satellite tail in Cs_2CO_3 and $CsHCO_3$, while the absence of all four signatures in CsI explains the lack of a comparable tail.

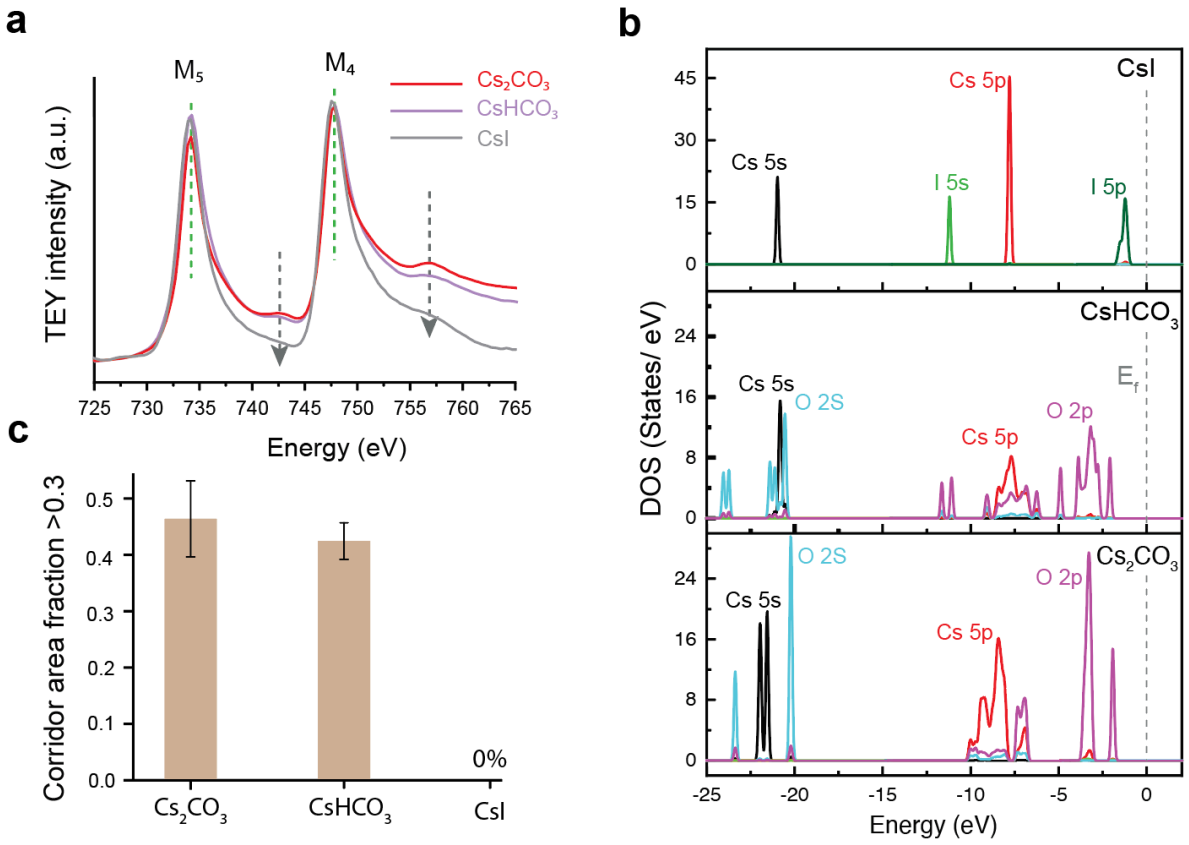

Figure 2.17. Cs–O interactions probed through Cs M-edge reference spectra. a, Cs M-edge spectra of solid-state Cs_2CO_3, $CsHCO_3$, and CsI. **b,** Projected density of states (PDOS) highlighting Cs 5s and 5p states and anion valence states: I 5s/5p in CsI (top), and O 2s/2p in $CsHCO_3$ (middle) and Cs_2CO_3 (bottom). The Fermi level is set to 0 eV. Carbonate phases show a significant orbital mixing between Cs 5p and O 2p states, whereas CsI exhibits well separated ionic manifolds. **c**, Corridor area fraction of Cs_2CO_3, $CsHCO_3$, and CsI.

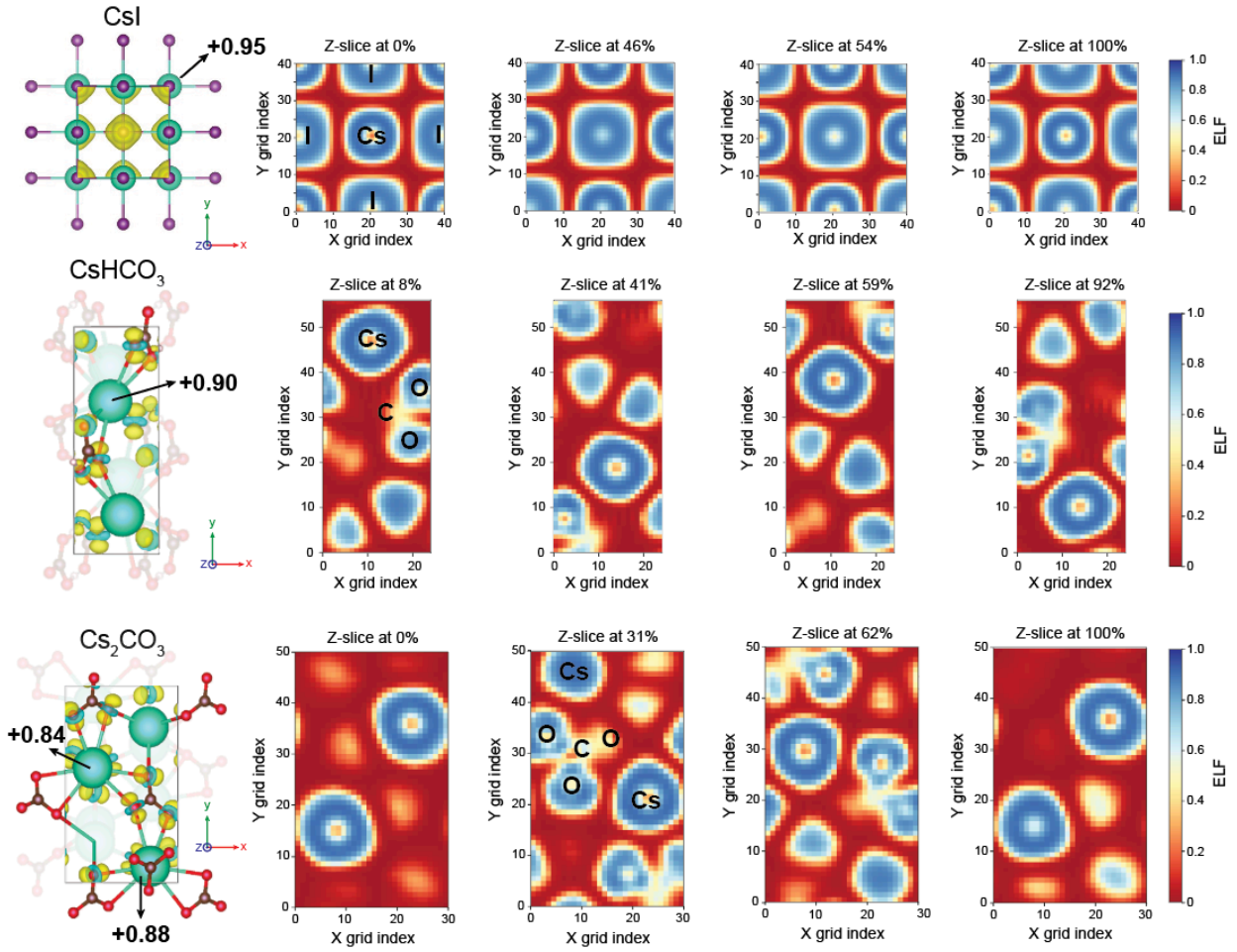

Figure 2.18, Bader charge analysis of solid-state Cs salts. Left: differential charge density ($\Delta\rho$ = ρ_total – $\Sigma\rho$_atomic) isosurfaces (positive accumulation / negative depletion) superimposed on the crystal structures (view along the x–y plane) for CsI, $CsHCO_3$, and Cs_2CO_3, including Bader charge value on Cs, revealing directional Cs–O polarization absent in Cs–I. Right: corresponding total charge density slices at four representative z positions, illustrating the emergence of intermediate inter-nuclear charge density corridors for Cs–O but not Cs–I. Atom colors: Cs (green), I (purple), O (red), C (brown), H (white).

The difference in tail intensity between $CsHCO_3$ and Cs_2CO_3 in the M-edge spectra correlates with the aggregate degree of polarized Cs–O bonding rather than a large increase in per-bond covalency. Bader charge analysis reveals that Cs ions in Cs_2CO_3 exhibit a slightly lower charge (+0.84 and +0.88) than the Cs ion in $CsHCO_3$ (+0.90), indicating more pronounced charge redistribution (partial electron back-polarization) for Cs_2CO_3. Atomic bond population analysis with the Crystal Orbital Hamiltonian Population (ICOHP) metrics further support this view: although the average per-bond ICOHP for "strong" Cs–O contacts (2.8–3.4 Å subset) is similar in the two phases (-0.170 vs -0.177 eV per bond, a negative ICOHP indicating a bonding interaction), Cs_2CO_3 hosts a

substantially larger number of such interactions (26 vs 16) in the unit cell, yielding a more negative cumulative ICOHP (–4.41 vs –2.83 eV). When all identified Cs–O contacts are included, the total ICOHP in Cs_2CO_3 (–5.54 eV over 60 bonds) also exceeds that in $CsHCO_3$ (–3.28 eV over 28 bonds), reflecting a denser network of weak-to-moderate polarized bonds. Taken together, these results indicate that the more extensive network of polarized partial-covalent Cs–O contacts in Cs_2CO_3—rather than a dramatic strengthening of any single bond—underpins its stronger M-edge satellite tail. Collectively, our experimental and computational results demonstrate that the intensity of satellite features in Cs M-edge spectra can serve as a sensitive probe of the strength and nature of interactions between Cs and its surrounding atoms.

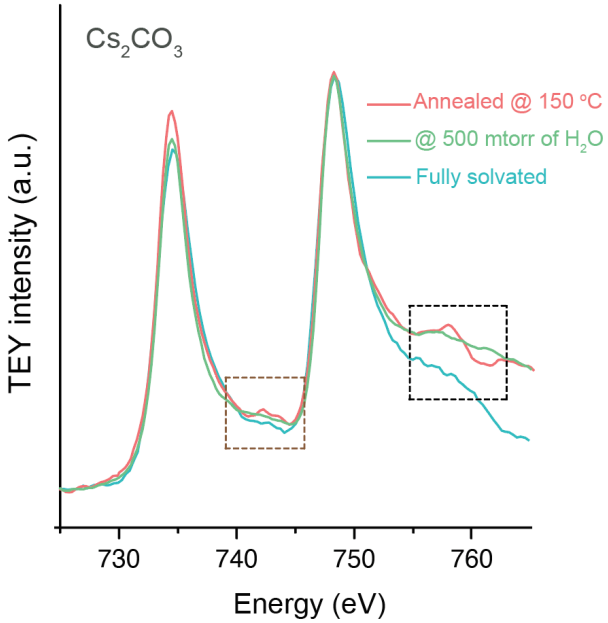

Figure 2.19. Cs M-edge spectra of Cs_2CO_3 measured under different water concentrations. Regions of 738–746 eV and 754–762 eV are highlighted, reflecting the evolution of satellite features with increasing water content.

To establish a baseline for interpreting *in situ* Cs M-edge spectra under electrochemical conditions—where cations are present in a solvated state—we further investigated the spectral evolution of Cs M-edges during the dissolution process. As shown in Figure 2.19, Cs_2CO_3 initially dried under vacuum calcination exhibits sharp satellite features at the previously identified energies, reflecting strong and well-defined Cs–O interactions in the crystalline lattice. However, upon gradual introduction of water vapor, these satellite features progressively broaden and eventually disappear at a water pressure of approximately 500 mTorr. The presence of water is expected to expand and/or distort the crystal lattice, leading to partial solvation. Once Cs^+ ions become fully solvated, a marked decrease in the tail intensity of the M-edge spectra is observed, indicating significantly weakened interactions between Cs^+ and its surrounding oxygen atoms. This weakening is consistent with the longer Cs–O distances in solvation shells compared to the short, directional Cs–O bonds in solid-state salts. These results confirm that M-edge satellite intensity is sensitive not only to the chemical identity of neighboring atoms, but also to the local

solvation structure, providing a valuable reference point for interpreting *in situ* measurements under electrochemical conditions.

2.4.4 The Cs-O interaction in the NOLI pocket

Building on our understanding of Cs M-edge spectral features, we next investigated the interaction between Cs^+ and various interfacial species within the Ag NOLI pocket using *in situ* Cs M-edge XAS. As outlined in Figure 2.20a, Cs M-edge spectra were first collected at OCV, followed by catalyst preconditioning at –0.2 V_{RHE}. After preconditioning, the potential was returned to OCV, and Cs M-edge spectra were recorded every 20 minutes to monitor temporal changes. It is important to note that directly measuring Cs M-edge TEY signals under –0.2 V_{RHE} is challenging. The large Faradaic current—typically on the order of microamperes in our setup—overwhelms the TEY signal, which is typically in the nanoampere range. Therefore, while the post-bias spectra may not perfectly capture the –0.2 V_{RHE} condition, their time-resolved evolution still offers valuable insights into interfacial Cs^+ behavior during catalysis. This is especially informative in the NOLI system, where the floating ligand layer restricts the rapid relaxation of the electric double layer once the bias is removed.

Before preconditioning, when the surfaces of Ag nanoparticles are chemisorbed with TDPA ligands, the Cs M-edge signal is weak in TEY mode, as shown in Figure 2.20b. This is because Cs^+ ions reside outside the ligand layer at this stage, and the electrons emitted from these ions cannot reach the electrode due to the short mean free path. After applying -0.2 V_{RHE}, an overall enhancement in the TEY signal is observed, indicating increased local Cs^+ concentration at the electrode interface. Concurrent O K-edge and SEIRAS measurements confirm reduced interfacial water content under bias, implying that Cs^+ ions at the interface are partially desolvated. Interestingly, at 0 minutes (i.e., immediately after returning to OCV), sharp satellite features emerge around 743 eV between the M_4 and M_5 edges, along with a broader tail feature centered at 757 eV. After 20 minutes, the 735–743 eV region becomes flattened, and the 757 eV feature diminishes significantly, continuing to fade by 40 minutes. Notably, these spectral changes are observed in TEY mode but absent in the bulk-sensitive TFY mode (Figure 2.20c), confirming that the spectral variations arise from the interfacial region rather than the bulk electrolyte.

The strong satellite features at 0 minutes reflect a pronounced interaction between Cs^+ and oxygen-containing species during catalysis. Within the NOLI pocket, several species could contribute to this interaction. First, Cs^+ may coordinate with the phosphonic acid groups of TDPA ligands, as supported by O K-edge data. Second, although Cs–H_2O interactions typically do not give rise to sharp satellite features, our prior work on graphene–electrolyte interfaces shows that at extremely high interfacial Cs^+ concentrations (~8 M), satellite features can emerge[134]. At such high local concentrations, even without applying bias, Cs^+ becomes partially desolvated and forms Cs-anion pairs. At the same time, the high concentration forces water molecules to approach closer to the Cs to compensate for the accumulated positive charge. The Cs-anion interaction and/or strengthened Cs–H_2O interactions can generate a noticeable satellite feature detectable by XAS[134]. Finally, given the applied bias and CO_2-saturated environment, the observed features could originate from direct interactions between desolvated Cs^+ and surface adsorbates, e.g. surface hydroxyl (*OH), which has been recently reported[70], or reaction intermediates, particularly $*CO_2^-$, as supported by SEIRAS data.

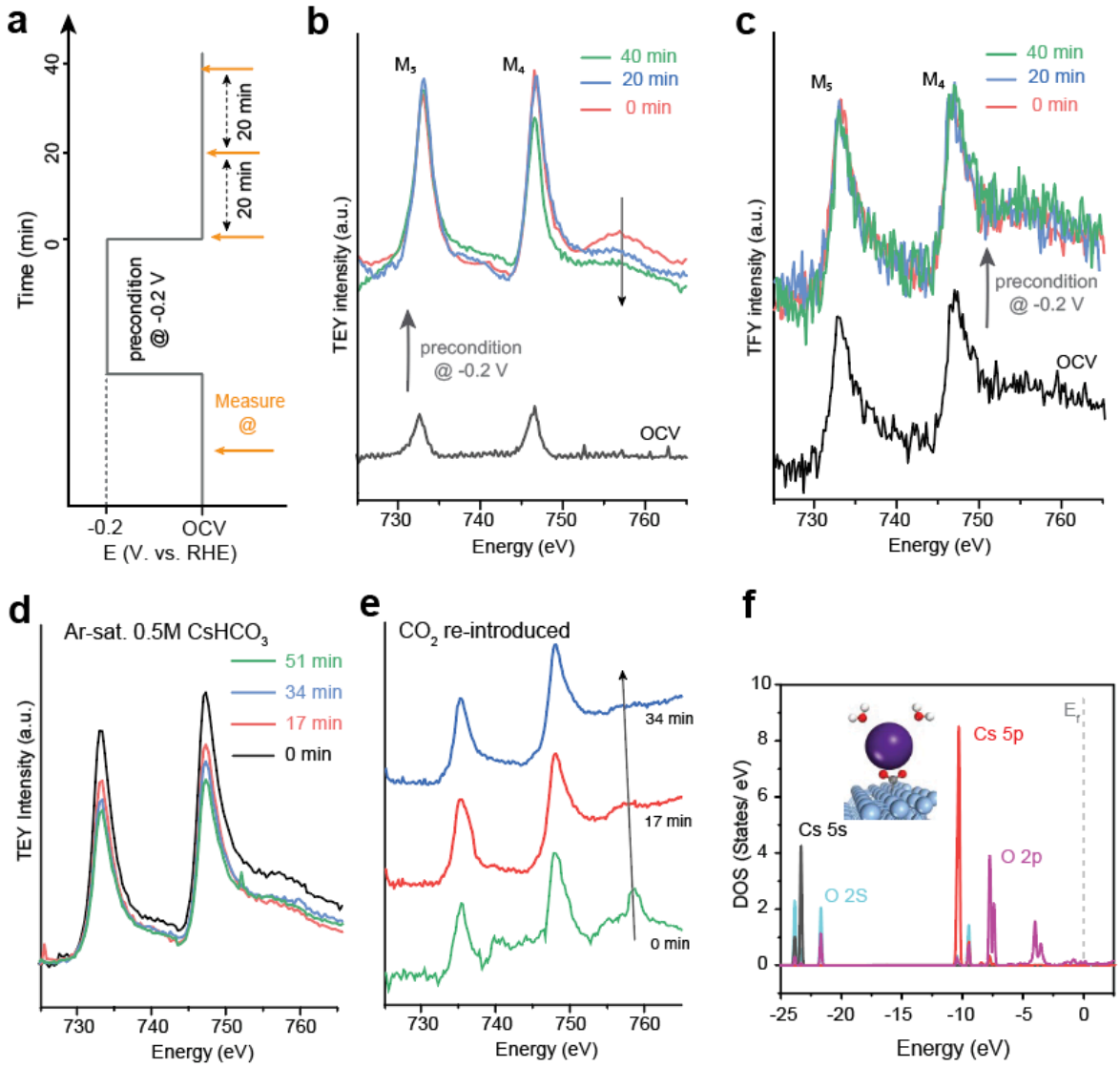

Figure 2.20. Cs–CO_2 interactions probed by *in situ* X-ray absorption spectroscopy (XAS). a, Schematic of the experimental protocol. XAS spectra were collected before preconditioning, and at 0 min, 20 min, and 40 min after preconditioning at –0.2 V_{RHE}. **b–c,** *In situ* Cs M-edge spectra acquired in (**b**) total electron yield (TEY) mode and (**c**) total fluorescence yield (TFY) mode in 0.5 M CO_2-saturated $CsHCO_3$., **d-e**, *In situ* Cs M-edge spectra collected in TEY mode under 0.5 M Ar-saturated $CsHCO_3$ electrolyte (**d**), followed by spectra obtained after reintroduction of CO_2 into the electrolyte (**e**). **f**, PDOS of an adsorbed *CO_2 stabilized by a partially desolvated Cs^+; O orbitals are selected exclusively from the two O atoms of adsorbed *CO_2.

To further elucidate the origin of the satellite features, we conducted *in situ* Cs M-edge measurements during an online electrolyte exchange from CO_2- to Ar-saturated conditions at OCV. After the Cs signal stabilized after electrolyte exchange, the same measurement protocol was

repeated: preconditioning at –0.2 V_{RHE} followed by spectral acquisition every 17 minutes. Under Ar, the Cs M-edge intensity did not recover to the level observed under CO_2, confirming that CO_2 is required to maintain a high interfacial Cs^+ concentration. As shown in Figure 2.20d, while a weak 757 eV satellite feature appeared at 0 minutes, its intensity was markedly lower than that under CO_2-saturated conditions. Upon reintroduction of CO_2, the satellite feature promptly recovered (Figure 2.20 e). Since Cs–ligand, Cs–HCO_3^-/Cs-CO_3^{2-}, and Cs–H_2O interactions remain largely unchanged between Ar and CO_2 conditions, these observations point to interactions with CO_2-derived surface intermediates as the origin of the satellite features. Alternative assignments—for instance, Cs–*OH interactions—can be ruled out, since under Ar conditions the coverage of *OH (if present) should be higher due to the absence of competitive adsorption of CO_2 intermediates, and would thus be expected to produce a stronger, not weaker, satellite signal. Instead, the observed trend is fully consistent with a direct interaction between desolvated Cs^+ and CO_2-derived intermediates, most likely adsorbed *CO_2^-. DFT calculations further support this conclusion. The DOS of adsorbed *CO_2^- stabilized by a partially desolvated Cs^+ (Figure 2.20f) shows significant orbital overlap between Cs 5p and O 2p states in the –6 to –12 eV region, as well as additional Cs 5s–O 2s overlap below –20 eV. S orbital overlapping is negligible in salt crystals like $CsHCO_3$ and Cs_2CO_3, suggesting an even stronger Cs–O interaction in the adsorbed *CO_2^-⋯ Cs^+ complex.

To mechanistically rationalize how desolvated Cs^+ promotes CO_2 activation, we generated seven idealized interfacial states (Figure 2.21a) that discretize a "desolvation coordinate" from Cs^+ with 6 explicit H_2O molecules, $Cs^+(6H_2O)$ (outer Helmholtz / diffuse layer–like environment)[134,135] to $Cs^+(1H_2O)$ (extreme near-surface coordination). These states are thermodynamic sampling points rather than a presumed kinetic pathway. We employed grand canonical DFT (GC-DFT) calculations and evaluated a grand free energy of CO_2 adsorption ($\Delta\Omega$) referenced to the clean Ag (111) surface with a solvated Cs^+, and the Gibbs free energy of solvated CO_2. We used hydrated $Cs^+(6H_2O)$ far from the interface as the reference point, where a physiosorbed, nearly linear CO_2 (O–C–O = 179.9°, average Cs–O = 4.56 Å) is observed. Slight disruption (lower symmetry) of the solvation shell ($6H_2O$) begins to bend the CO_2 (angle → 171.0°) at the Ag surface (Figure 2.21b). Progressive water removal (5→$1H_2O$) shortens Cs–O (of CO_2) from 3.51 → 2.83 Å and CO_2–Ag contact from 2.82 → 2.19 Å, while ICOHP(Cs–O) magnitudes become more negative (–0.11, –0.14, –0.18, –0.19, -0.20 eV for 5, 4, 3, 2, $1H_2O$ respectively; Figure 2.21c), evidencing an increasing partial covalent component in Cs-O bond. This enhanced interaction yields a more "activated" *CO_2 intermediate that is structurally predisposed for downstream protonation (Figure 2.12).

Potential-dependent $\Delta\Omega$ profiles (Figure 2.21d) show several crossovers: Above -0.1 V_{RHE}, $Cs^+(3H_2O)$ minimizes $\Delta\Omega$; between -0.1 V_{RHE} to –0.8 V_{RHE} a ($2H_2O$) state becomes competitive, and more negative than –0.8 V_{RHE} the ($1H_2O$) state is lowest. These results suggest that under increasingly reductive conditions, activated CO_2 is preferentially stabilized by Cs^+ with progressively higher degrees of desolvation. Since such desolvated cation–intermediate interactions are thermodynamically promoted by applied bias, we propose that they are not unique to ligand-defined NOLI interfaces but represents a general feature of electrochemical solid–liquid interfaces once cation desolvation can be sustained.

In conventional ligand-free metal electrodes operated in dilute aqueous electrolytes, cations are expected to remain largely solvated, limiting the magnitude and persistence of such specific interactions. This provides a natural explanation for why cation effects are commonly observed on

bare metal surfaces yet are typically more modest and highly sensitive to electrolyte identity and operating conditions. In contrast, the NOLI architecture stabilizes a locally ion-rich, water-deficient interfacial microenvironment, thereby amplifying the population of desolvated Cs^+ ions and rendering their direct interaction with $*CO_2^-$ experimentally observable and catalytically significant.

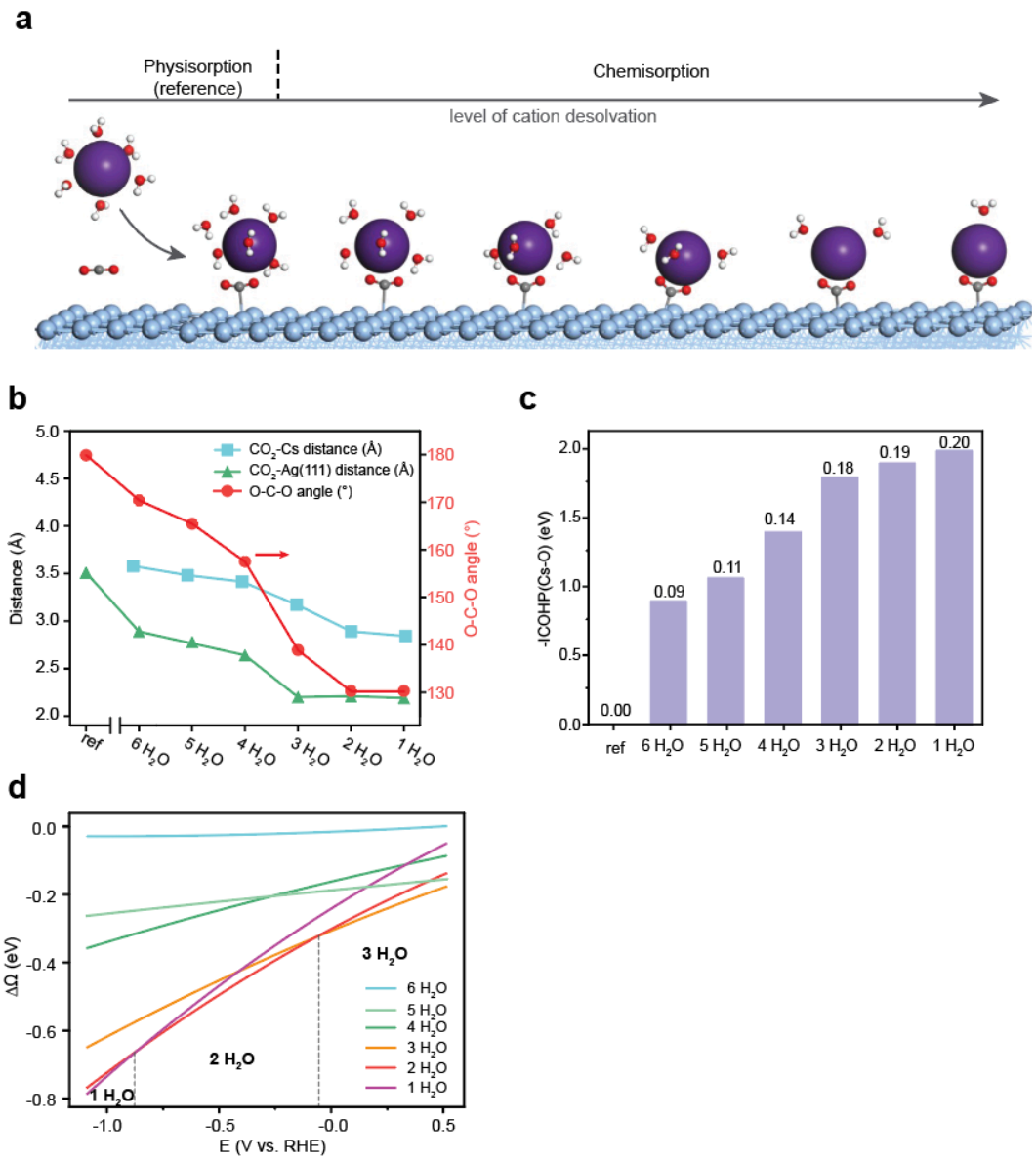

Figure 2.21 CO_2-Cs interactions calculated using GC-DFT. **a**, GC-DFT-optimized adsorption structures of CO_2 under varying degrees of Cs^+ desolvation. Color code: Cs (purple), O (red), C (gray), H (white). **b,** Structural descriptors including average Cs–O_CO_2 (light blue), Ag (111)–CO_2 (green) bond lengths and the O–C–O bond angle (red) of adsorbed CO_2 across the configurations in **a**. **c,** Negative integrated crystal orbital Hamilton population (–ICOHP) values reflecting the bond strength between Cs and CO_2 in the structures shown in **a**. **d,** Calculated

potential-dependent stability of different *CO_2–Cs structures in f with varying degrees of cation desolvation.

The spectroscopic and computational results presented in this section collectively reveal that the NOLI architecture fundamentally modifies the interfacial ionic environment. In particular, the ligand-defined confinement promotes cation enrichment and partial cation desolvation, enabling strong interactions between Cs^+ and CO_2-derived intermediates such as *CO_2^-. These findings establish a direct molecular-level connection between the interfacial microenvironment and the activation of CO_2. Building upon these mechanistic insights, the following section integrates the experimental observations into a unified model that explains the unusually low overpotential observed for CO_2 reduction in NOLI systems.

2.5 Mechanistic model for low-overpotential CO_2 reduction in NOLI systems

By combining multiple *in situ* spectroscopic techniques with theoretical calculations, the preceding sections have elucidated the dynamic interplay among ligands, electrolyte cations, interfacial water, and catalytic intermediates within the NOLI architecture. These observations together provide a coherent mechanistic picture that explains the enhanced catalytic performance of NOLI systems.

The formation of the NOLI structure originates from the collective behavior of surface ligands during electrochemical operation. As the applied bias induces nanoparticle coarsening, the ligands detach from the metal surface yet remain confined near the nanoparticle due to cooperative ligand–ligand interactions. This process generates a distinctive interfacial architecture consisting of a metal nanoparticle core, a confined aqueous layer, and an outer ligand scaffold. This ligand-defined interlayer significantly alters the local electrochemical microenvironment. The confined space between the nanoparticle surface and the ligand layer favors the accumulation of electrolyte cations while simultaneously reducing the local water activity. As a result, cations entering this region experience restricted solvation and become partially desolvated.

When CO_2 molecules diffuse into this interfacial pocket, the partially desolvated cations can interact directly with adsorbed CO_2 species. In particular, the formation of *CO_2^-–cation complexes stabilizes the activated CO_2 intermediate through partial covalent interactions between Cs and oxygen atoms of *CO_2^-. These interactions effectively lower the energetic barrier associated with the first electron-transfer step of CO_2 reduction. Because CO_2 activation is the rate-determining step for CO formation on Ag catalysts, stabilization of the *CO_2^- intermediate substantially decreases the overpotential required for CO_2 reduction. In this framework, the role of the ligand layer is not to directly participate in the catalytic reaction but rather to engineer the interfacial environment that enables strong cation–intermediate interactions. Within this architecture, the ligand layer acts as a structural scaffold that stabilizes a high local cation concentration, while cations themselves function as a “glue” that bridges the catalytic surface and

reaction intermediates. The degree of cation desolvation—and therefore the strength of cation–intermediate interactions—emerges as a key parameter controlling CO_2 activation.

Importantly, the NOLI structure represents only one possible strategy for achieving such an environment. More broadly, similar desolvation-enabled cation–intermediate interactions could be accessible in other confined or low-water-activity interfacial environments, such as highly concentrated electrolytes[72], ionic-liquid–containing media[136], and nanoporous or ionomer-containing electrodes[137,138], where ion crowding and restricted solvation are more likely to occur. Altogether, these insights underscore the importance of interfacial design—specifically, engineering ion-rich, water-deficient microenvironments—as a general strategy to harness desolvated cation–intermediate interactions for enhancing reactivity across a wide range of electrochemical transformations.

While the NOLI architecture provides a well-defined platform for uncovering the role of cation desolvation in CO_2 activation, the broader implications of this mechanism extend beyond ligand-modified Ag catalysts. In practical catalytic systems, particularly those based on Cu, the electrochemical interface is often far more complex and dynamic. Copper surfaces undergo substantial restructuring under reaction conditions and interact strongly with electrolyte species, leading to heterogeneous interfacial environments whose structure and composition remain poorly understood. These complexities raise important questions regarding how electrolyte ions, water molecules, and reaction intermediates organize near Cu surfaces and how such microenvironmental factors influence catalytic behavior. Addressing these questions requires experimental tools capable of probing electrochemical interfaces with both molecular specificity and spatial resolution under *operando* conditions. In the following chapter, we extend the microenvironment perspective developed for NOLI systems to Cu catalysts and investigate how ion distributions, interfacial water structure, and adsorbate interactions evolve at Cu–electrolyte interfaces during CO_2 electroreduction.

Chapter 3 Microenvironment Effects on Cu Catalysts

Portions of the content and figures in this chapter are reproduced with permission from:

Xiao Zhao#, Yu Shan #, Evan Carlson#, Ka Chon Ng, Tianle Wang, Alex Sachelarie, Stephaine G. Corder, Hans A. Bechtel, Michal Bajdich, Peidong Yang, Miquel B. Salmeron, *Nanometer-resolved Copper-electrolyte interface*. (2026, in preparation).

Maria V. Fonseca Guzman#, Yu Shan#, Tianle Wang#, Julian Feijoo, Nathan Liu, Jihoon Choi, Gabrielle Heuer, Andrew Liu, Peidong Yang, *A Lens into the Cu Nanograin by in situ Vibrational Spectroscopy*. (2026, in revision)

3.1 Preface

Copper remains the only monometallic catalyst capable of electrochemically converting CO_2 into multi-carbon (C_2^+) products at appreciable rates[6]. Because of this unique capability, Cu-based catalysts occupy a central position in the field of CO_2 electroreduction. However, as we discussed in previous sections, Cu catalysts typically suffer from poor selectivity and require large overpotentials to achieve practical current densities, which limits their potential for energy-efficient CO_2 conversion.

As demonstrated in Chapter 2, engineering the electrochemical microenvironment provides a powerful strategy to enhance catalytic performance at low overpotential beyond the intrinsic catalytic capability of catalysts. In NOLI, ligand-assisted cation desolvation and direct cation–intermediate interactions enable CO_2 reduction at unusually low overpotentials. Extending this microenvironment perspective to Cu catalysts represents an important step toward understanding how electrolyte structure influences more complex catalytic systems. However, such investigations are considerably more challenging for Cu, whose surfaces undergo substantial electrochemical restructuring and show stronger oxygen affinity[29], resulting in dynamic interfaces with poorly defined active sites.

In this chapter, we present initial efforts to probe the Cu–electrolyte interface using *in situ* vibrational spectroscopic techniques that provide complementary spatial resolution and chemical sensitivity. The first study employs nanometer-resolved nano-FTIR spectroscopy to investigate the interfacial structure of Cu catalysts in bicarbonate electrolytes, revealing pronounced spatial heterogeneity in anion distributions near nanoscale Cu features and providing insights into the organization of interfacial water on polycrystalline Cu surfaces. The second study combines Surface Enhanced Raman Spectroscopy (SERS) and Surface-Enhanced Infrared Absorption Spectroscopy (SEIRAS) to probe CO adsorption on Cu nanograin catalysts, where a characteristic twin-CO adsorption feature is observed with a pronounced dependence on electrolyte cations. Although these studies do not yet provide a unified mechanistic picture comparable to that established for NOLI catalysts in Chapter 2, they highlight the critical importance of spatially

resolved characterization for understanding the dynamic coupling between catalyst structure, electrolyte microenvironment, and reaction intermediates on Cu surfaces. Together, these results provide a foundation for understanding microenvironment effects on Cu catalysts and underscore the importance of probing electrochemical interfaces with both molecular specificity and nanometer spatial resolution.

3.2 Nanometer-resolved Cu-thin film-electrolyte interface

In this section, we resolve the molecular structure and evolution of the electrical double layer (EDL) surrounding Cu electrodes in a CO_2-saturated 0.1 M $KHCO_3$ electrolyte using *in situ* nano-FTIR spectroscopy. The spatial distribution of interfacial ions and the structure of interfacial water are tracked during the electrochemical transformation of the electrode, including the reduction of Cu_2O to metallic Cu and the restructuring of the initially continuous Cu film into nanoparticles. The observations in this section reveal an important governing principle: the chemical composition of the electrode surface primarily determines the structure of interfacial water, while other factors—including applied potential and electrolyte ions—mainly influence the orientation and ordering of the interfacial water network. In addition, the experimentally observed lateral ion gradients provide a direct nanoscale map of ion distributions within the electrical double layer, revealing pronounced in-plane heterogeneities in the electrochemical microenvironment. These results highlight that spatial variations in the microenvironment must be considered when designing catalytic interfaces targeting specific reaction pathways. Meanwhile, the experimental platform—also introduced in Section 2.2—provides unprecedented molecular-level insight into the dominant species at electrochemical interfaces and opens new opportunities for visualizing complex solid–liquid systems, ranging from aqueous batteries to biological interfaces.

3.2.1 Evolution of the Cu electrode under applied potential.

Our experimental setup employs an electrochemical nano-FTIR cell consisting of an array of ~1 μm diameter holes patterned in a SiNx membrane. The membrane is coated with an approximately 25 nm Au film to provide electrical contact and is capped with a single-layer graphene membrane that separates the electrolyte from the probing tip. Schematic drawings of one hole in the device are shown in Figure 3.1a–c; a similar experimental configuration was previously described in Section 2.2. A broadband, spatially coherent infrared beam from the synchrotron source at the Berkeley Advanced Light Source (ALS) is focused onto the apex of an atomic force microscope tip coated with a Pt–Ir alloy. Incident IR photons excite plasmonic oscillations of electrons within the tip, generating a strongly confined electromagnetic near field at the tip apex in the mid-infrared frequency range. Because this evanescent field decays exponentially away from the tip over a distance comparable to the tip radius, the resulting spectroscopic signal provides both topographic and chemical sensitivity with a lateral spatial resolution of approximately ~20 nm.[84,139].

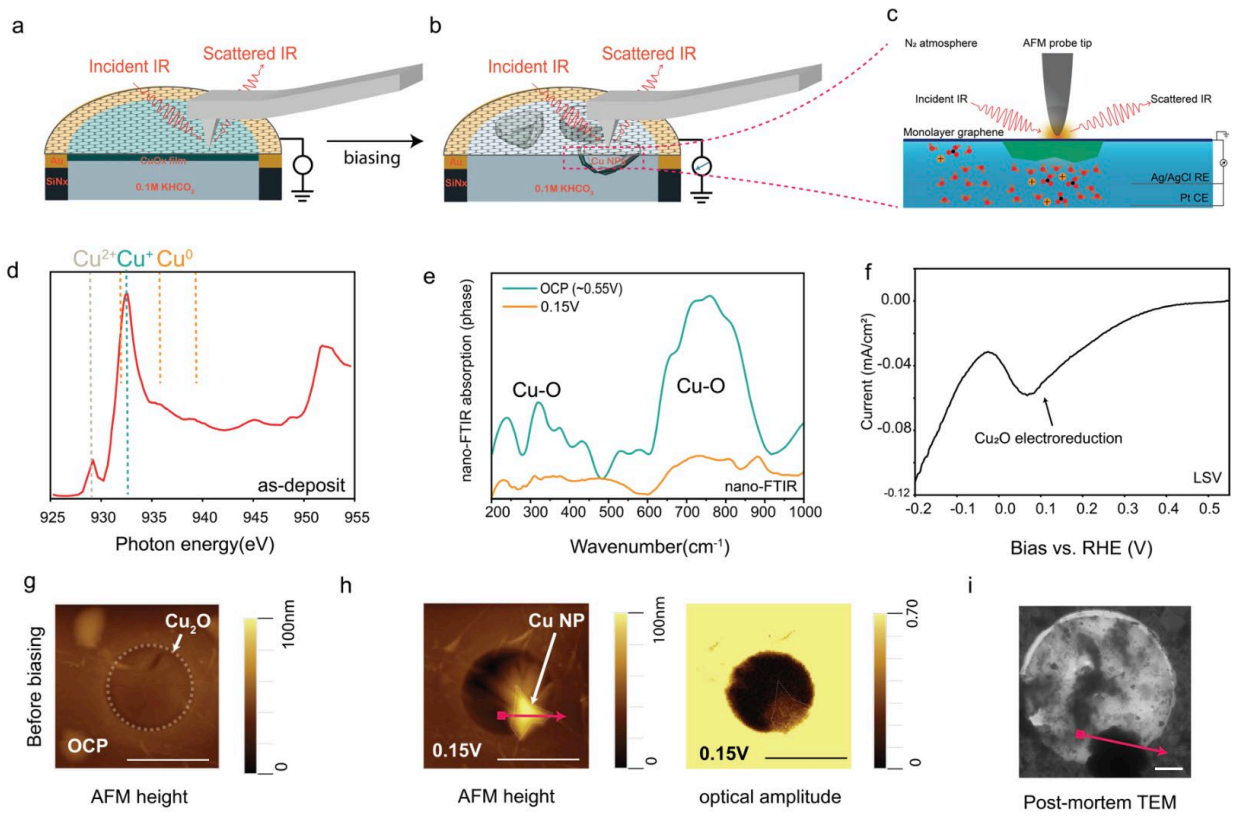

Figure 3.1 Experimental setup and electrochemical evolution of the Cu thin-film electrode. **a–c,** Schematic of the *in situ* nano-FTIR electrochemical cell. An AFM tip probes a monolayer graphene membrane sealing ~1 μm holes in a 100-nm-thick SiNx support. A thin Cu film deposited on graphene oxidizes to Cu_2O in air and is reduced under applied bias to form metallic Cu nanoparticles beneath the graphene. The cell contains CO_2-saturated 0.1 M $KHCO_3$ electrolyte and uses Ag/AgCl and Pt as reference (RE) and counter (CE) electrodes. **d,** *Ex situ* XANES spectrum of the as-deposited Cu film measured in total electron yield (TEY) mode (~3 nm probing depth), showing a Cu^+ feature at ~932.4 eV characteristic of Cu_2O. **e,** Nano-FTIR spectra (200–1000 cm^{-1}) of the Cu film at open-circuit potential (OCP, cyan) and at 0.15 V vs RHE (orange), showing reduction of Cu–O vibrational features. **f,** Linear sweep voltammogram of the Cu film in CO_2-saturated 0.1 M $KHCO_3$ showing Cu_2O reduction onset near ~0.2 V vs RHE. **g,** AFM topographic map of the graphene membrane acquired at OCP prior to nano-FTIR measurements (scale bar: 1 μm). **h,** Left: AFM topography of the same region. Right: reflected infrared intensity map showing a bright feature at the center corresponding to a Cu nanoparticle formed after reduction at 0.15 V. **i,** Post-nano-FTIR TEM image showing Cu nanoparticles formed through electrochemical reduction and aggregation of the initial Cu_2O film, with a scale bar of 200nm.

A 4 nm Cu film was sputtered onto the graphene surface. Upon exposure to air, the film oxidizes to copper oxide, predominantly Cu_2O, as confirmed by *ex situ* X-ray Absorption Near Edge Structure (XANES) measurements (Figure 3.1d). Nano-FTIR spectroscopy was then used to monitor the electrochemical reduction of the copper oxide layer *in situ* in a CO_2-saturated 0.1 M

$KHCO_3$ electrolyte. A representative nano-FTIR spectrum acquired at open-circuit potential (OCP, ~0.55 V vs RHE) and at 0.15 V vs RHE is shown in Figure 3.1e. The spectrum obtained at OCP exhibits characteristic Cu_2O vibrational features between 200–350 cm^{-1} together with a broad band spanning 650–850 cm^{-1}, corresponding to longitudinal and transverse optical phonon modes of Cu_2O[140,141].

When a bias of 0.15 V vs RHE is applied, the intensity of the Cu–O vibrational features decreases significantly, indicating the electrochemical reduction of Cu_2O to metallic Cu. This observation is consistent with the linear sweep voltammogram (LSV) shown in Figure 3.1f, which shows the onset of Cu_2O reduction near 0.2 V vs RHE. A small residual Cu–O signal remains at 0.15 V, likely originating from residual oxygen species at the surface or subsurface regions under this relatively mild potential. Importantly, the reduction of the Cu_2O film is accompanied by significant morphological restructuring. The initially continuous thin film aggregates into a Cu nanoparticle, as revealed by AFM topographic and optical amplitude images (Figure 3.1g–i). Unless otherwise noted, all electrochemical potentials reported here are referenced to the reversible hydrogen electrode (RHE).

3.2.2 Infrared nanospectroscopy of electrolyte species

Simultaneously with the reduction of Cu_2O, the evolution of interfacial water and carbonate species was monitored using nano-FTIR spectroscopy. Spectra were collected along a line scan across Cu nanoparticles following the trajectory indicated by the red arrows in Figure 3.1h and 3.1i. The spatial position of the AFM tip along this trajectory is indicated on the left axis of the corresponding plots, while the applied electrochemical potential is shown on the bottom axis. The resulting spectra are displayed in Figure 3.2 as heat maps representing the vibrational intensities associated with water and carbonate species. These maps include the O–H stretching and H–O–H bending modes of water together with the symmetric and asymmetric stretching modes of carbonate species (ν_s(O–C–O) and ν_{as}(O–C–O)). In these plots, the wavenumber is shown on the x-axis, while the absorption intensity—approximately proportional to the phase component of the nano-FTIR signal—is represented by the color scale. These spatially resolved measurements enable simultaneous monitoring of electrolyte species and electrode surface chemistry during the electrochemical transformation of the copper surface.

At 0.15 V, clear spatial inhomogeneities appear in the infrared profiles. Specifically, the intensity of the O–H stretching mode decreases on the Cu nanoparticles, while the intensities of ν_s(O–C–O), ν_{as}(O–C–O), and the H–O–H bending mode increase relative to those measured on bare graphene regions. The enhanced carbonate and bending-mode intensities likely arise from plasmonic infrared field enhancement within the nanogap formed between the tip and metallic copper or between neighboring Cu nanoparticles[142]. In contrast, the reduced intensity of the O–H stretching mode may reflect changes in the orientation of interfacial water molecules near the potential of zero charge (PZC) around 0.15 V. Because nano-FTIR selectively probes vibrational dipoles oriented perpendicular to the surface, a tilt of interfacial water molecules relative to the surface normal would reduce the observed signal.[84,143]. Meanwhile, the nano-FTIR spectra collected on the bare graphene support remain essentially unchanged compared to those obtained at OCP. Applying more negative potentials induces only minor additional changes in the spatial

distribution of these vibrational modes relative to those observed at 0.15 V. As the potential becomes increasingly negative, the intensity profile gradually becomes more uniform.

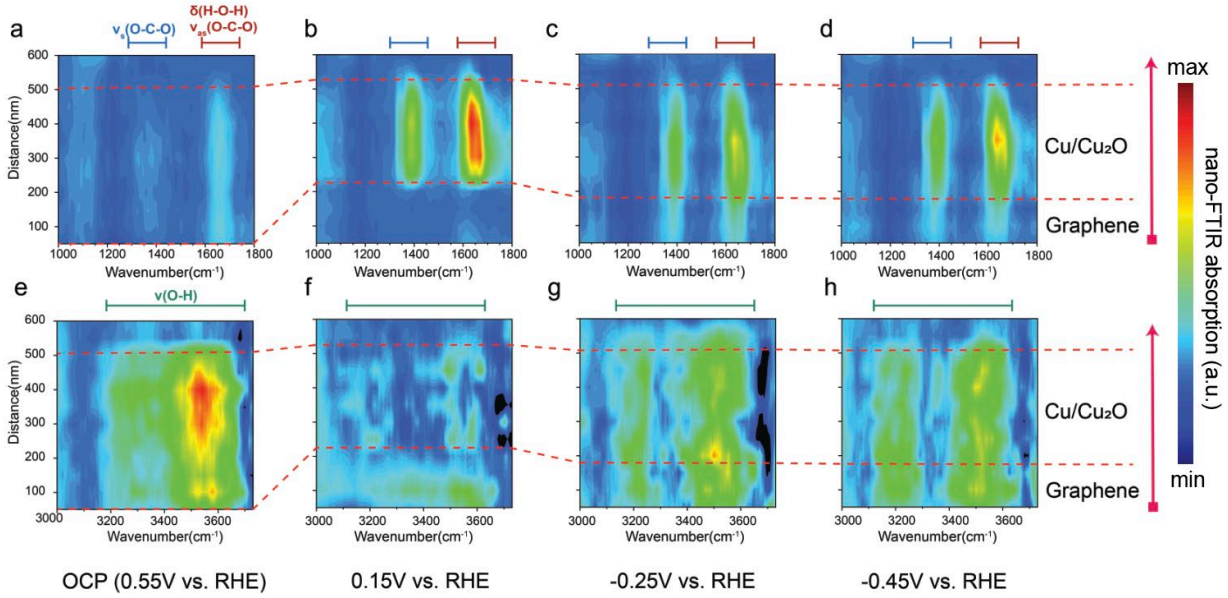

Figure 3.2 Spatially resolved nano-FTIR spectra across the Cu/Cu₂O–graphene interface under electrochemical bias. a–d, Nano-FTIR spectral maps in the 1000–1800 cm^{-1} region recorded at (**a**) open-circuit potential (OCP, ~+0.55 V vs RHE), (**b**) +0.15 V, (**c**) −0.25 V, and (**d**) −0.45 V. This spectral window contains the ν_s(O–C–O) bending mode of bicarbonate/carbonate species and the δ(H–O–H) bending mode of water. **e–h,** Nano-FTIR spectral maps in the 3000–3650 cm^{-1} region recorded at (**e**) OCP (~+0.55 V vs RHE), (**f**) +0.15 V, (**g**) −0.25 V, and (**h**) −0.45 V, corresponding to the O–H stretching modes of interfacial water. Nano-FTIR spectra were acquired as the AFM tip scanned across the Cu₂O/Cu nanoparticle and surrounding graphene along the red dashed lines shown in Figure. 3.1h, i. The vertical axis represents scan distance, and the horizontal axis represents infrared wavenumber. The color scale corresponds to the nano-FTIR absorption signal derived from the phase channel. The regions separated by the red dashed horizontal lines correspond to Cu₂O/Cu nanoparticles (upper region) and graphene (lower region).

3.2.3 Spatial distribution of ion near Cu/ Cu₂O particles

We now address the spatial distribution and local concentration of electrolyte anions near Cu₂O and Cu nanoparticles. This distribution plays a critical role in electrochemical reactions such as CO_2 reduction, where bicarbonate ions serve as both pH buffers and potential proton donors[144,145], as discussed previously in Section 1.5.4. However, the lateral distribution of ions at electrochemical interfaces has remained largely unexplored due to the limited spatial resolution of conventional optical techniques.

Here we demonstrate that nano-FTIR spectroscopy enables direct mapping of the local HCO_3^- concentration under different electrochemical biases. To quantify the local bicarbonate concentration, we developed a spectroscopic “reference ruler” based on the ratio between two

vibrational features[146]: the symmetric stretching mode of bicarbonate near 1350 cm^{-1}, which is unique to HCO_3^-, and the combined intensity of the water bending mode and the asymmetric bicarbonate stretching mode near 1650 cm^{-1}. The calibration was obtained using bulk-sensitive ATR-FTIR measurements of $KHCO_3$ solutions with concentrations ranging from 0 M (pure water) to saturation (~3.0 M), as shown in Figure 3.3a. As expected, the intensity of the symmetric bicarbonate stretching mode increases approximately linearly with concentration below ~2.5 M, while the peak near 1650 cm^{-1} shows weaker linearity due to contributions from both water bending and bicarbonate asymmetric stretching vibrations. The ratio between these two peaks as a function of concentration yields the calibration curve shown in Figure 3.3b, which serves as the reference ruler for converting nano-FTIR peak ratios into local electrolyte concentrations.

Using this calibration, nano-FTIR peak ratios measured at specific tip positions can be converted into local interfacial concentrations. An example of this conversion is illustrated by the dashed L-shaped red line in Figure 3.3b, which connects a measured nano-FTIR peak ratio to the corresponding electrolyte concentration. Colored markers on the calibration curve indicate measurements obtained at different electrode locations, including graphene, Cu nanoparticles, and oxide regions. From these measurements, spatial concentration maps and line profiles can be constructed. Figure 3.3c shows representative line profiles across a Cu nanoparticle and the surrounding graphene support. Two-dimensional concentration maps were also generated over larger regions of the interface, as shown in Figure 3.3d, where the bicarbonate concentration is represented by color intensity.

Remarkably, the measurements reveal substantial enrichment of bicarbonate ions at the interface. On the cuprous oxide film at OCP (Figure 3.3d, left panel), a uniformly distributed interfacial bicarbonate concentration of approximately 1.5 M is observed—nearly 15 times higher than the bulk concentration of 0.1 M. At 0.15 V, the ion distribution around metallic Cu nanoparticles exhibit pronounced spatial heterogeneity. While the bicarbonate concentration at the graphene–electrolyte interface remains largely unchanged compared to OCP, the concentration at the nanoparticle–electrolyte interface increases to approximately 2.0 M, indicating enhanced ion accumulation near the Cu surface. This enrichment may arise from the strong chemical affinity between Cu surfaces and electrolyte ions, a phenomenon frequently observed in SEIRAS studies[147]. Alternatively, enhanced electric fields near the Cu nanoparticles may attract both cations and anions into the electrical double layer.

Interestingly, the graphene support adjacent to Cu nanoparticles exhibits a depletion of bicarbonate ions, suggesting lateral migration of HCO_3^- toward the nanoparticles under this bias. Counterintuitively, increasing the cathodic bias further leads to continued accumulation of bicarbonate ions at the interface while simultaneously promoting ion enrichment on the graphene support, ultimately producing a more uniform distribution across the system. These observations indicate the interfacial ion distribution behaves beyond the prediction of GCS theory, but rather indicate a competition between chemical interactions and electrostatic repulsion within the electrical double layer. Chemical interactions appear to dominate under mild bias, whereas electrostatic effects associated with the potential drop across the double layer become dominant at larger negative potentials. Overall, the distinct ion aggregation behavior observed on copper relative to graphene—and the lateral depletion of bicarbonate ions near Cu nanoparticles—reveals pronounced nanoscale heterogeneity at electrochemical interfaces. This heterogeneity is expected to strongly influence the structure of interfacial water, which we discuss in the following section.

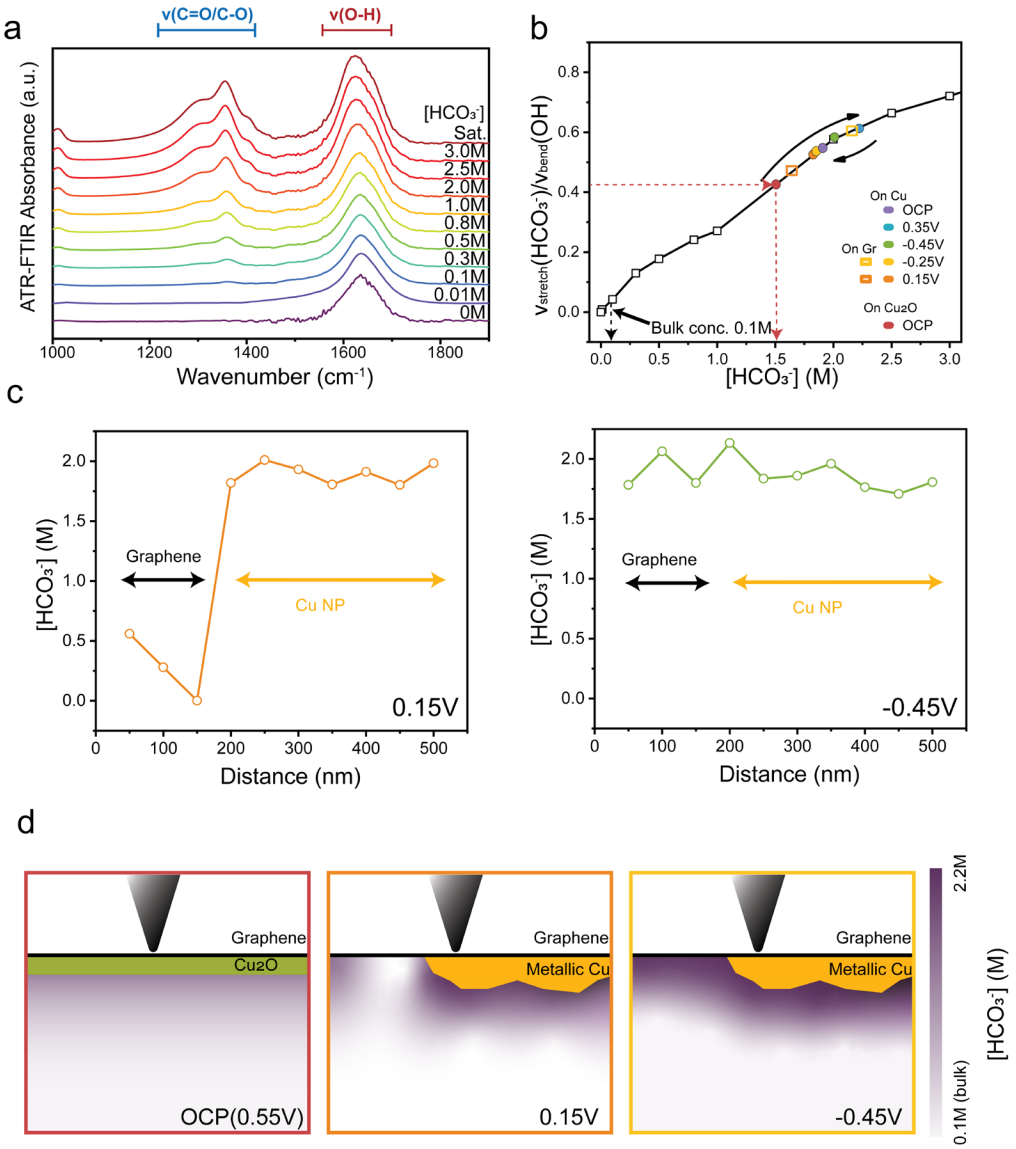

Figure 3.3 Determination of HCO_3^- concentration and spatial distribution at the Cu–electrolyte interface. a, Bulk ATR-FTIR spectra of CO_2-saturated $KHCO_3$ electrolytes (1 atm CO_2) with different bicarbonate concentrations ranging from 0 to 3.0 M. The spectra show the ν(C–O–C/O–C–O) vibration of HCO_3^- near ~1350 cm^{-1} and the water O–H bending / asymmetric HCO_3^- stretching modes near ~1650 cm^{-1}, which are used to quantify bicarbonate concentration. **b,** Calibration curve relating bicarbonate concentration to the intensity ratio $\nu(HCO_3^-)/\ \delta(H_2O)$, obtained from the bulk ATR-FTIR spectra in (**a**) (black open squares). The ratio measured by nano-FTIR at the Cu interface is plotted on the same graph to estimate local interfacial concentrations. Symbols indicate measurements acquired with the tip positioned on Cu nanoparticles under different potentials (filled circles), on graphene (open rectangles), and on Cu_2O at open-circuit conditions (red filled circles). **c**, Spatial line profiles of the estimated HCO_3^- concentration across graphene and a Cu nanoparticle obtained from nano-FTIR measurements. The left panel shows the concentration profile at 0.15 V vs RHE, and the right panel shows the profile at −0.45 V vs RHE. The horizontal axis represents the scan distance across the interface, with the graphene region and Cu nanoparticle region indicated by arrows. **d,** Schematic

representations of the inferred interfacial bicarbonate concentration distributions at different potentials: OCP (~0.55 V), 0.15 V, and −0.45 V. The purple color intensity represents the relative HCO_3^- concentration, referenced to the bulk electrolyte concentration (~0.1 M), as indicated by the color scale on the right.

3.2.4 Interfacial water structure around Cu and Cu_2O nanoparticles.

To gain molecular-level insight into the structure of interfacial water on Cu and Cu_2O electrodes, nano-FTIR measurements were combined with density functional theory (DFT) and ab-initio molecular dynamics (AIMD) simulations. The AIMD configurations shown in the lower panels of Figure 3.4f–h correspond to representative water structures whose calculated vibrational density of states (v-DOS) best reproduce the experimental nano-FTIR spectra of the O–H stretching region shown in Figure 3.4a, b. Three model systems were considered: Cu_2O (111) without applied charge, Cu (111) without net charge, and Cu (111) under negative potential.

The experimental O–H bending region of cuprous oxide under open-circuit conditions exhibits a single broad peak centered near 1650 cm^{-1} (Figure 3.4a). As increasingly negative potentials are applied, this feature splits into two peaks at approximately 1630 cm^{-1} and 1665 cm^{-1}, indicating the presence of water molecules experiencing different hydrogen-bonding strengths[148,149]. These two peaks merge again once the bias is removed. The O–H stretching region is significantly more sensitive to hydrogen-bond strength and therefore provides deeper insight into the local chemical environment of interfacial water. Under open-circuit conditions on cuprous oxide, several features appear around 3250 cm^{-1}, 3500 cm^{-1}, and 3650 cm^{-1}, which can be assigned to water molecules experiencing strong, intermediate, and weak hydrogen-bonding environments, respectively. The intense peak near 3500 cm^{-1} closely resembles that of bulk water and remains largely unchanged under applied bias, suggesting that it originates from water molecules located beyond the inner Helmholtz plane. The broad shoulder between 3200–3400 cm^{-1} corresponds to strongly hydrogen-bonded water molecules, often referred to as “ice-like” water. In contrast, the peak near 3650 cm^{-1}, which appears only on cuprous oxide under open-circuit conditions and disappears once the surface is reduced to metallic copper, likely arises from weakly hydrogen-bonded interfacial water molecules[148,150-152].

The coexistence of water molecules with different hydrogen-bonding strengths is reproduced in AIMD simulations (Figure 3.4c, f). On the Cu_2O (111) surface, water molecules in the first layer form a disrupted hydrogen-bond network caused by a slight lattice mismatch between the hexagonal water network and the oxygen lattice of the Cu_2O (111) surface. Similar structures have previously been reported in DFT simulations of single- and double-layer water as well as in low-temperature STM studies[153]. The corresponding simulated v-DOS spectrum (Figure 3.4c) exhibits a strong hydrogen-bonding shoulder between 3200–3400 cm^{-1}, a major peak near 3600 cm^{-1}, and an additional shoulder near 3770 cm^{-1}. A systematic blue shift of approximately 100 cm^{-1} is observed between the simulated v-DOS spectrum and the experimental nano-FTIR spectra.

A substantial change in the interfacial water structure occurs when the electrode surface is reduced to metallic copper under cathodic bias. Below approximately 0.15 V, a broad peak centered near 3200 cm^{-1} increases significantly in intensity, indicating the formation of more

strongly hydrogen-bonded water networks on the metallic Cu surface, while the weak-bonding feature near 3650 cm^{-1} disappears. AIMD simulations of water monolayers on Cu (111) further support this interpretation.

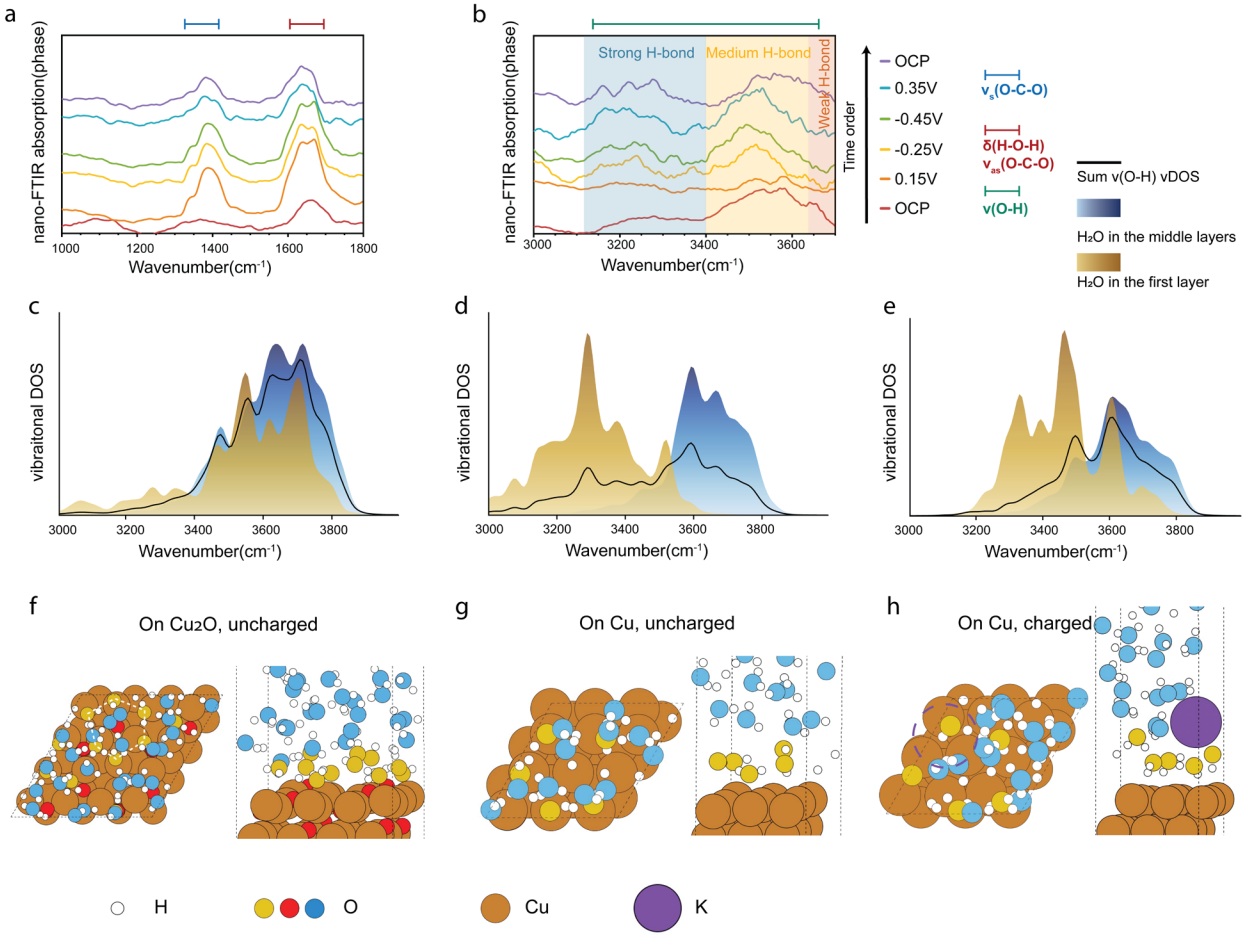

Figure 3.4 Nano-FTIR results and corresponding AIMD simulation of interfacial water structure on copper. **a**, Nano-FTIR spectra collected over a cuprous oxide nanoparticle in the 1000–1800 cm^{-1} region, containing the ν(O–C–O) vibration of bicarbonate and the δ(H–O–H) bending mode of water. **b**, Nano-FTIR spectra acquired at the same location in the 3000–3720 cm^{-1} region corresponding to the O–H stretching modes of interfacial water. Colored traces correspond to different applied potentials; the red spectrum at the bottom is the averaged spectrum of a cuprous oxide film at open-circuit potential (OCP). **c**, Calculated vibrational density of states (v-DOS) of water on uncharged Cu_2O (111). **d**, v-DOS of water on uncharged Cu (111). **e**, v-DOS of water on charged Cu (111) representing cathodic bias conditions. In **c-e**, the black line shows the total v-DOS of all water molecules, while yellow and blue shaded areas represent contributions from water molecules in the first interfacial layer and outer layers, respectively. **f**, AIMD-derived atomic configuration of the Cu_2O (111)/water interface. (g) Atomic configuration of the Cu (111)/water interface. **h**, Atomic configuration of the charged Cu (111)/water interface. In **f-h**, left panels show top views and right panels show side views of the interface. In the AIMD models, H, Cu, and K atoms are shown as white, brown, and purple spheres, respectively; oxygen atoms from interfacial water, outer water layers, and the Cu_2O lattice are shown in yellow, blue, and red. A

systematic ~100 cm^{-1} shift is observed between the calculated v-DOS spectra and the experimental nano-FTIR spectra.

In contrast to the disrupted hydrogen-bond network observed on Cu_2O (111), water molecules in the first molecular layer on Cu (111) form networks composed of structural units ranging from hexagonal to pentagonal rings on the surface (Figure 3.4d, g). Although the average hydrogen-bond strength in this first layer is slightly weaker than that on Cu_2O, a larger number of hydrogen bonds form overall, and the hydrogen-bonding environment becomes more homogeneous across the interfacial layer. This structural arrangement leads to the emergence of a single broad infrared feature centered near 3200 cm^{-1}, consistent with the enhanced vibrational intensity between 3200–3400 cm^{-1} observed in the calculated v-DOS spectrum (Figure 3.4d). Water molecules beyond the first layer remain relatively disordered and exhibit vibrational features similar to those of bulk water, with peaks near 3500 cm^{-1}.

To simulate electrochemical bias conditions, excess charge was introduced into the Cu electrode and compensated by K^+ ions located near the outer Helmholtz plane (OHP) or within the diffusion layer, corresponding to effective ion concentrations of approximately 1.5–2 M (Figure 3.4e, h). Under these conditions, the electric field increases the flexibility of the interfacial hydrogen-bond network and induces partial reorientation of water dipoles along the surface normal direction. However, the calculated v-DOS spectra show only minor changes compared with the uncharged system. This result suggests that the precise position of cations within the electrical double layer cannot be determined solely from the vibrational signatures of interfacial water.

Taken together, the combination of *in situ* nano-FTIR measurements and AIMD simulations provides a detailed molecular-level description of the Cu–bicarbonate electrolyte interface. Even at open-circuit potential, a remarkable ~15-fold enrichment of ions occurs at the native cuprous oxide surface, where interfacial water adopts a disrupted hydrogen-bond network. Upon applying cathodic bias, the oxide layer is reduced to metallic copper, triggering further ion accumulation and the formation of pronounced lateral ion depletion zones on the surrounding support. Concurrently, interfacial water reorganizes into a more ordered hydrogen-bond network on the metallic copper surface. At increasingly negative potentials, ion enrichment extends across the support, leading to a more spatially homogeneous electrochemical environment.

This section reveals the nanoscale structure and evolution of the Cu thin-film–electrolyte interface during electrochemical operation. Using operando nano-FTIR spectroscopy combined with AIMD simulations, we directly mapped the spatial distribution of electrolyte ions and the molecular structure of interfacial water during the reduction of Cu_2O to metallic Cu. The measurements reveal substantial ion enrichment at copper surfaces—reaching concentrations more than an order of magnitude higher than the bulk electrolyte—as well as pronounced lateral ion redistribution across the interface. Simultaneously, interfacial water undergoes significant structural reorganization, transitioning from a disrupted hydrogen-bond network on cuprous oxide to a more ordered hydrogen-bonded structure on metallic copper. These results demonstrate that electrochemical interfaces are intrinsically heterogeneous at the nanoscale and that both ion distributions and water structures are strongly coupled to electrode composition and applied potential.

While the Cu thin film provides a valuable model platform for probing these interfacial phenomena, two limitations motivate extending the investigation to more catalytically relevant

systems. First, the electrochemical potentials accessible in the nano-FTIR experiments are relatively limited, with the most negative bias reaching only −0.45 V vs. RHE, which remains more positive than typical operating potentials for CO_2 reduction on Cu. Consequently, the microenvironment observed here may not fully represent the conditions present during active catalysis. Second, although the Cu film serves as a well-defined model surface, its catalytic performance toward CO_2 reduction is relatively modest. To obtain more relevant insight into microenvironment–catalyst interactions, it is therefore desirable to directly examine catalysts that exhibit efficient CO_2 reduction at low overpotentials. In the following section, we investigate the microenvironment surrounding Cu nanograin catalyst, where CO_2 reduction proceeds at substantially lower overpotentials.

3.3 Electrochemical microenvironment and intermediates dynamics on Cu nanograin

Cu-based catalysts are uniquely capable of C–C coupling during electrochemical CO_2 reduction (CO_2R), yet further mechanistic understanding remains hampered by the lack of spectroscopically resolved descriptors that demonstrate how surface adsorbates emerge and evolve within their catalytic microenvironment. In this section, we correlate *in situ* surface-enhanced Raman spectroscopy (SERS) and surface-enhanced infrared absorption spectroscopy (SEIRAS) to resolve the potential-dependent dynamics during CO_2R on Cu nanograin catalysts. By building on previous benchmarking of low overpotential performance and nanograin structural evolution, we offer a diagnostic framework linking vibrational signatures to catalytic function, unveiling which species appear, persist, and turnover as the electrified surface and interfacial environment evolve under bias. The onset of linear CO is marked below -0.45 V, coincident with persistent adsorbed *OH/*O domains beyond the CO_2R onset. In this context, Cu nanograins serve as a platform to dissect contributions of adsorbate coverage. By carefully dissecting the potential dependence of emergent twin-defect/step CO stretch bands (P1-P2), alongside the prototypical terrace-site CO stretch band (P3), we provide important context for interpreting coupled spectroscopic trends driven by coverage effects and resolve this for the evidently complex nanograin morphology. Together, these observations highlight the intertwined roles of surface stabilization and interfacial flux in steering multicarbon product formation. By directly linking vibrational signatures to catalytic behavior, this section aims to bridge the gap between observation and control and help guide towards a predictive framework of fine-tuned activity for CO_2R.

3.3.1 Potential-dependent surface speciation prior to CO_2R

Characterization of pristine 6.7 nm Cu nanoparticles at open-circuit voltage (OCV) on SERS substrates reveals vibrational features consistent with partially oxidized Cu surfaces, including the Cu_2O T_2g mode near ~532 cm^{-1} and a CuO_x feature around ~628 cm^{-1} (Figure 3.5a)[154]. These

spectra correspond to the initial, non-equilibrated catalyst surface, where residual oxide layers and surface ligands limit electrolyte wetting and suppress coordination of carbonate species prior to the application of cathodic bias[155]. Upon cathodic polarization, the oxide-related bands progressively diminish and disappear by approximately −0.20 V vs. RHE, indicating electrochemical reduction of the surface to metallic Cu. While this reduction step establishes the metallic surface required for catalysis, the onset of CO_2 reduction cannot be attributed solely to the exposure of Cu^0. Instead, once the oxide layer is removed, the evolving chemical environment at the solid–liquid interface becomes the dominant factor governing the stabilization of adsorbates and the development of catalytic activity.

Prior to the onset of measurable CO_2 reduction, the SERS spectra reveal the formation of an interfacial adsorbate layer dominated by carbonate-derived species. As shown in Figure. 3.5a, several vibrational features emerge between −0.10 and −0.30 V vs. RHE, including bands near ~360 cm^{-1}, ~712 cm^{-1}, ~1070 cm^{-1}, and ~1525 cm^{-1}. These modes are assigned to carbonate and bicarbonate species originating from the 0.1 M $KHCO_3$ electrolyte. In particular, the correlated features near ~360 cm^{-1} and ~1525 cm^{-1} are attributed to surface-bound bidentate carbonate ($*O_2CO$) species coordinated to Cu sites[156-158]. In contrast, the ~1070 cm^{-1} band arises from interfacial carbonate species that are weakly associated with the surface or remain within the near-surface electrolyte layer. These observations indicate that both specifically adsorbed carbonate species and more weakly bound interfacial ions coexist within the electrochemical interface during early stages of polarization.

The distinct potential dependence of these bands reflects differences in their interaction with the electrode surface. The bidentate carbonate modes evolve systematically with applied bias, consistent with stronger coupling to the Cu surface and sensitivity to changes in the local electric field. By contrast, the ~1070 cm^{-1} symmetric stretch exhibits minimal Stark response, indicating weaker interaction with the metal surface. Additional spectral features observed near ~706–715 cm^{-1} and in the 800–1300 cm^{-1} region correspond to bending and deformation modes of carbonate and bicarbonate species, consistent with the coexistence of multiple carbonate coordination motifs at the interface. Together, these observations suggest that carbonate species form a heterogeneous interfacial layer whose structure evolves as the Cu surface undergoes electrochemical reduction and reconstruction.

The emergence of these carbonate-related features reflects the strong influence of electrolyte chemistry on the electrochemical microenvironment. Under CO_2 reduction conditions, the bicarbonate–carbonate buffering system dynamically regulates the interfacial supply of CO_2 through rapid acid–base equilibria and interconversion reactions[75]. Consequently, both CO_3^{2-} and HCO_3^- species are expected to populate the near-surface region, and their relative abundance evolves with applied potential. The persistence of carbonate-related vibrational modes across the early potential window therefore indicates that carbonate species form a transient adlayer during catalyst activation.

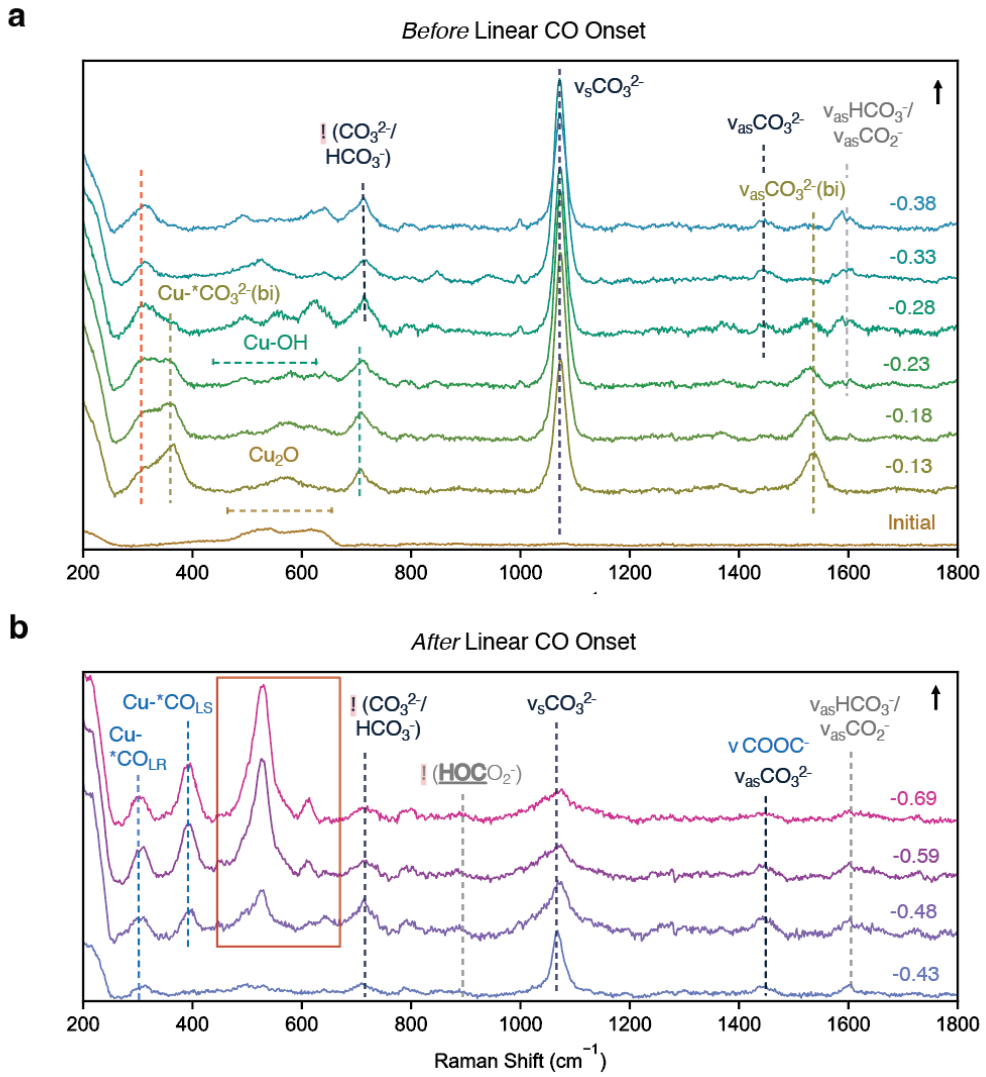

Figure 3.5. *in situ* SERS spectra of Cu nanocatalysts under stepped electrochemical biases. **a**, Spectra evolution before linear CO onset, depicting the reduction and reconstruction stages of Cu nanocatalyst. **b**, Spectra collected after linear CO onset, highlighting reaction-induced interactions among surface adsorbates. The modes contributing to the complex band at 435-625 cm^{-1} (red outline) are Cu-*OH (~525 cm^{-1}) and Cu-*O (~603 cm^{-1}) modes. Potentials are applied stepwise and potentiostatically. All measurements are performed in 0.1 M $KHCO_3$ with a 6 mL/min electrolyte flow and 14 sccm CO_2 bubbling rate. All spectra are collected using a 633 nm incident laser.

Importantly, the evolution of carbonate species coincides with structural transformations of the Cu surface. Rather than representing simple competitive adsorption with catalytic intermediates, these carbonate structures likely emerge from the interplay between electrolyte adsorption and surface reconstruction. As shown in Figure. 3.5b, the gradual reorganization of interfacial carbonate species accompanies the transition from partially oxidized Cu surfaces toward catalytically active metallic sites. Similar behavior has been observed in *in situ* STM and surface X-ray diffraction

studies, where carbonate adlayers evolve concurrently with structural transitions of Cu surfaces during electrochemical polarization[155,159,160]. Within this framework, carbonate species should be viewed as dynamic components of the electrochemical microenvironment that accompany catalyst activation.

The preferential stabilization of electrolyte anions during early cathodic polarization highlights the important role of electrolyte-derived species in shaping the interfacial environment. Compared with molecular CO_2, carbonate species are more readily stabilized at the Cu surface through electrostatic and coordination interactions. Their formation and gradual displacement during polarization therefore reflect the evolving balance between electrolyte adsorption, surface reconstruction, and the emergence of catalytic intermediates. These observations emphasize that the electrochemical microenvironment—defined by the coupled dynamics of surface structure, electrolyte species, and interfacial electric field—plays a central role in governing the early stages of CO_2 reduction on Cu catalysts.

3.3.2 Transition to active CO binding and its co-adsorbates

The carbonate-dominated interfacial environment described in Section 3.3.1 precedes the emergence of catalytic intermediates associated with CO_2 reduction. As cathodic bias increases beyond this regime, spectroscopic signatures reveal the gradual displacement of interfacial carbonate species and the appearance of CO-bound states characteristic of active CO_2 reduction. In nanostructured Cu catalysts, the accumulation of adsorbed CO intermediates (*CO) is more pronounced than on planar analogues due to the high density of undercoordinated surface atoms, enlarged electrochemically active surface area, and shorter migration length scales associated with nanograin architectures[161]. As shown in Figure 3.5b, distinct vibrational features corresponding to linear (atop-bound) CO emerge at intermediate potentials. These signals strengthen with increasingly negative bias, indicating the progressive formation and stabilization of *CO intermediates under catalytic conditions. The evolution of these spectral features reflects the transition from a carbonate-dominated interface to one populated by reactive intermediates associated with CO_2 reduction.

The low-frequency region provides additional insight into the dynamics of CO adsorption. As shown in Figure 3.6, vibrational modes corresponding to the Cu–*CO frustrated rotation (νCu–$*CO_{LR}$) and Cu–C(O) stretching (νCu–$*CO_{LS}$) evolve systematically with applied potential[162]. The relative intensity of these modes reflects changes in *CO surface coverage. Specifically, the ratio between the stretching and frustrated rotation modes increases with more negative bias, indicating hindered rotational motion of adsorbed CO at higher surface coverages. Similar behavior has been reported previously and attributed to steric crowding and lateral interactions among adsorbed CO molecules[163]. The evolution of this ratio therefore marks the transition into a regime of higher *CO coverage associated with active CO_2 reduction.

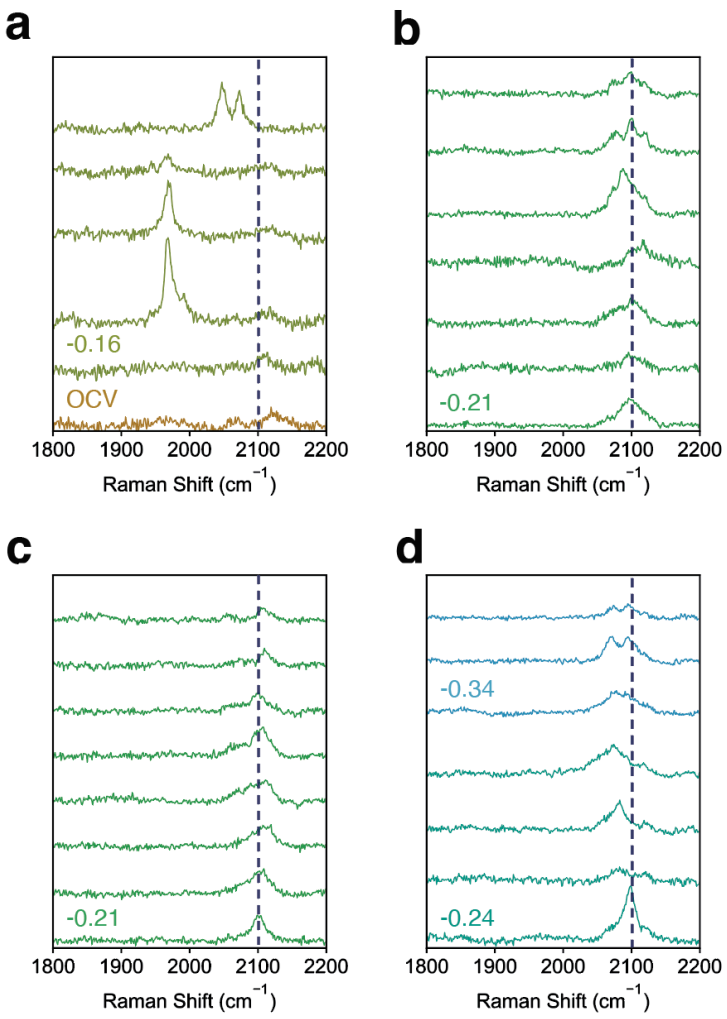

Figure 3.6. Time-resolved SERS spectra of the CO stretching region. Individual traces correspond to sequential measurements acquired approximately **(a)** 1 minute apart, reflecting the temporal evolution of surface intermediates during early catalyst restructuring, or **(b-d)** 3 minutes apart. **(b)** and **(c)** are recorded at the same applied potential but at different times during the experiment, capturing changes in surface state adsorbate population, and SERS fluctuation under otherwise identical electrochemical conditions.

Notably, once the onset of linear CO adsorption is reached, no evidence is observed for a transition from atop to bridge-bound CO configurations. The persistence of linear CO signatures throughout the potential range investigated indicates that atop CO serves as the dominant reactive intermediate under these conditions. This observation is consistent with previous studies of nanostructured Cu catalysts, where the presence of undercoordinated sites and grain boundaries stabilizes linear CO binding geometries[164]. The stabilization of these sites is therefore critical for sustaining catalytic turnover and highlights the importance of preserving the nanograin architecture of the catalyst.

While CO adsorption signals dominate the spectral response in this potential range, additional features appear in the low-frequency region that correspond to surface oxygen-containing co-adsorbates. In particular, a complex band near ~525 cm^{-1} becomes prominent as the potential reaches approximately −0.48 V to −0.98 V vs. RHE (Figure 3.5b). This feature is assigned primarily to Cu–*OH vibrations associated with surface-bound hydroxide species in a atop configuration. Isotopic substitution experiments further support this assignment. As shown in Figure 3.7, the ~525 cm^{-1} band exhibits measurable shifts upon exchange with D_2O, confirming that hydrogen-containing species contribute to this vibrational feature[157]. In contrast, a separate mode observed near ~603 cm^{-1} remains invariant under both $^{13}CO_2$ and D_2O exchange. This behavior indicates that the mode arises from lattice-bound oxygen species (*O) rather than hydroxyl groups. Vibrational frequencies in the 603–610 cm^{-1} range have been consistently attributed to Cu–O vibrations in previous spectroscopic studies across a broad pH range[154,165,166]. These observations therefore establish the coexistence of surface-bound *OH and *O species alongside adsorbed CO intermediates during catalytic operation.

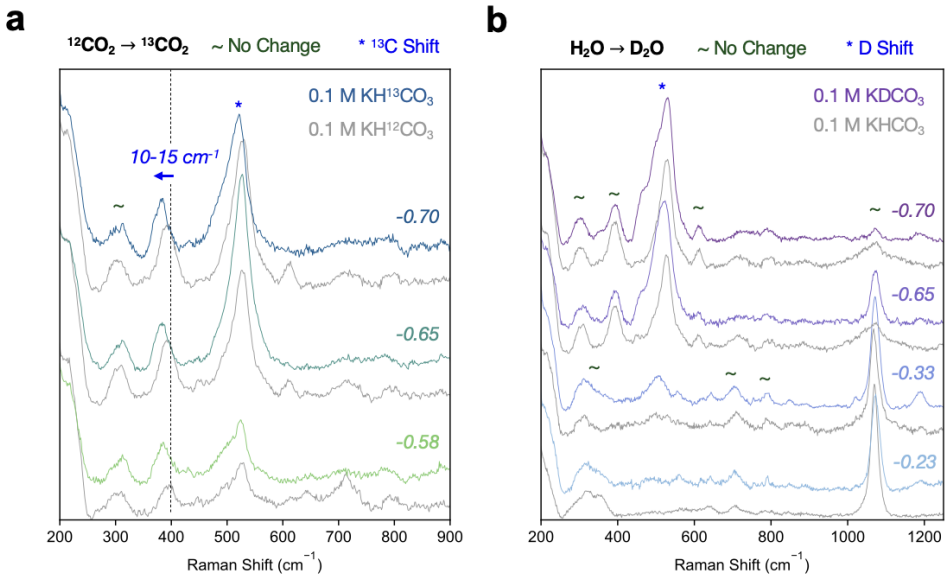

Figure 3.7. *in situ* SERS spectra of Cu nanocatalysts in isotopically labeled electrolytes. a, Spectra collected in 0.1M $KH^{13}CO_3$ (pH = 8.4), showing the expected blue shift of Cu-C mode upon $^{13}CO_2$ substitution. **b**, Spectra collected in 0.1 M $KDCO_3$ (D_2O, pH = 7.0). Spectra from the standard 0.1 M $KHCO_3$ electrolyte (replotted from **Figure 3.5b**) are overlaid for comparison. All spectra are collected using a 633 nm incident laser.

The presence of these oxygen-containing co-adsorbates has important implications for the electrochemical microenvironment at the Cu interface. Rather than acting as passive spectators, *OH and *O species can modify the electronic structure of surface Cu atoms and influence the stabilization of catalytic intermediates. In particular, oxy-species are capable of transient charge storage and redistribution, enabling them to function as coupled proton–electron reservoirs during

electrochemical turnover[167-169]. Through these interactions, surface oxygen species can modulate the electron density of nearby Cu sites and stabilize charged reaction intermediates involved in CO_2 reduction.

Beyond their electronic influence, oxy-species also affect the structure of the interfacial solvent environment. The presence of surface-bound *OH and *O perturbs the hydrogen-bonding network of interfacial water within the compact Stern layer, altering local proton activity and field screening near the electrode surface. These changes can influence adsorption energies and reaction barriers by modifying the electrostatic environment experienced by intermediates. For example, dipolar oxygen-containing species introduce local electric fields that reshape the potential profile across the interface and alter charge-transfer energetics[170,171]. Such field effects may contribute to the stabilization of charged intermediates and thereby influence catalytic selectivity.

Structurally, oxygen-containing species can also affect the dynamic reconstruction of Cu surfaces under cathodic bias. Nanograin catalysts contain a high density of defects, grain boundaries, and undercoordinated atoms, which are susceptible to restructuring during electrochemical operation. Adsorbed *O and *OH species can stabilize these low-coordination sites by increasing diffusion barriers and suppressing surface migration processes[172-174]. In this way, oxy-species may transiently stabilize defect-rich configurations that are favorable for catalytic activity.

The formation of these species is further facilitated by the evolving local chemical environment during CO_2 reduction. As CO_2 reduction proceeds, the generation of OH^- leads to an increase in local pH near the electrode surface. Under these conditions, surface oxygen species may persist even when bulk thermodynamics would predict their removal[154,175,176]. Consequently, the coexistence of *CO, *OH, and *O species observed in the SERS spectra reflects the dynamic interfacial environment established during catalytic turnover.

Taken together, these observations highlight the existence of co-adsorbates and their role in shaping the catalytic microenvironment of Cu nanograin catalysts. The simultaneous presence of *CO and oxygen-containing species indicates that catalytic intermediates evolve within a complex adsorbate network rather than on a clean metal surface. These co-adsorbates modify the electronic structure, electrostatic environment, and structural stability of the catalyst, thereby influencing both the spectroscopic response and the catalytic reaction landscape. Within this framework, the transition from carbonate adsorption to CO-bound intermediates represents not only the onset of CO_2 reduction but also the emergence of a dynamically coupled interfacial microenvironment that governs catalytic activity.

3.3.3 Interfacial field and coverage effects on CO vibrational signatures

To extend the mechanistic picture obtained from *operando* Raman measurements on Cu nanograins, surface-enhanced infrared absorption spectroscopy (SEIRAS) is employed as a complementary probe. While Raman excels at metal–adsorbate and lattice modes, SEIRAS selectively amplifies dipoles aligned normal to the metal surface and therefore excels at probing C–O, C–H, and other polar stretching modes[177,178]. In addition, SEIRAS offers superior temporal resolution, enabling direct tracking of the sub-second/second(s) response of surface intermediates to electrochemical perturbations[179]. Monolayer Cu nanograin films were loaded onto an SEIRAS-

active Au films. To activate Cu nanograins, two synchronized linear-sweep voltammetry (LSV) from 0 V to -1.0 V vs. RHE were performed (LSV 1 and 2), and SEIRAS spectra were collected during cathodic sweep (LSV 3), followed by an anodic sweep (LSV 4) and a subsequent cathodic sweep (LSV 5), with a reference spectrum collected at 0V.

Notably, CO adsorption on the Cu nanograins evolves into an unusual and multi-component C-O stretch lineshape at more negative potentials. Deconvolution of the atop-CO region requires three distinct spectral contributions (P1–P3): P1 at ~2083 cm^{-1}, P2 at ~2070 cm^{-1}, and P3 at ~2050 cm^{-1} (Figure 3.8a). Two of these bands correspond to well-established binding configurations on Cu surfaces[180-184]. P2 is related to step/edge-site adsorption, and P3 originates from terrace-site adsorption, both of which are commonly reported across common Cu catalysts and reproduced for Cu films[185-190]. Regarding the high-frequency P1 component, although one might be tempted to attribute this band to a new and distinctive CO adsorption site, one must consider the impacts of coverage of strong dipole adsorbates in fundamentally skewing the selection rule of SEIRAS. Figure 3.8b summarizes the bias-dependent evolution of the CO stretching modes under alternating LSV scans. Firstly, the reversibility of the twin P1/P2 pattern in cyclic sweeps indicates that their appearance is governed by *electrostatics and screening*, rather than by irreversible restructuring of the Cu surface.

Once the potential is driven more cathodically than –0.60 V, at which point the P1 feature becomes prominent, P1 and P2 exhibit strikingly similar behavior across all scans, displaying nearly identical bias-induced frequency shifts and comparable tuning rates. This strong correlation suggests that both components originate from CO molecules adsorbed at defect-rich sites, such as steps, edges, kinks, or grain boundaries, which share similar intrinsic vibrational frequencies. Importantly, although they arise from similar adsorption environments, P1 and P2 retain distinct vibrational frequencies and line shapes, consistent with subtle differences in local coordination or interfacial conditions.

To better understand whether the appearance of P1 involves coverage-dependent (dipole–dipole) effects, we next examined the intensity of the P1 feature under conditions expected to modulate surface coverage. Because the infrared intensity of *CO adsorbed at defect sites can be significantly amplified through dipole–dipole coupling[187,191], and because intermolecular dipole–dipole interactions scale with CO coverage, their contribution can be systematically probed through online gas-switching experiments[192,193]. Upon switching the feed gas from CO_2 to N_2, both P1 and P2 exhibit an immediate and synchronized red shift (Figure 3.8c), indicating that P1, like P2, is subject to dipole–dipole interactions among adsorbed *CO molecules. However, if strong dipole–dipole coupling were the dominant factor governing the spectral response, one would expect pronounced “intensity borrowing”, specifically an enhancement of the highest-frequency mode (P1) accompanied by a depletion of the lowest-frequency mode (P3). The absence of such intensity redistribution cannot be fully rationalized at present. Instead, we attribute the relatively weak dipole–dipole coupling on Cu nanograins to the presence of substantial co-adsorbates, such as *O and *OH species, between neighboring *CO molecules. These co-adsorbates, independently detected by SERS, likely disrupt coherent dipole coupling among adjacent *CO species and thereby suppress large shifts in vibrational intensity associated with selection-rule modifications.

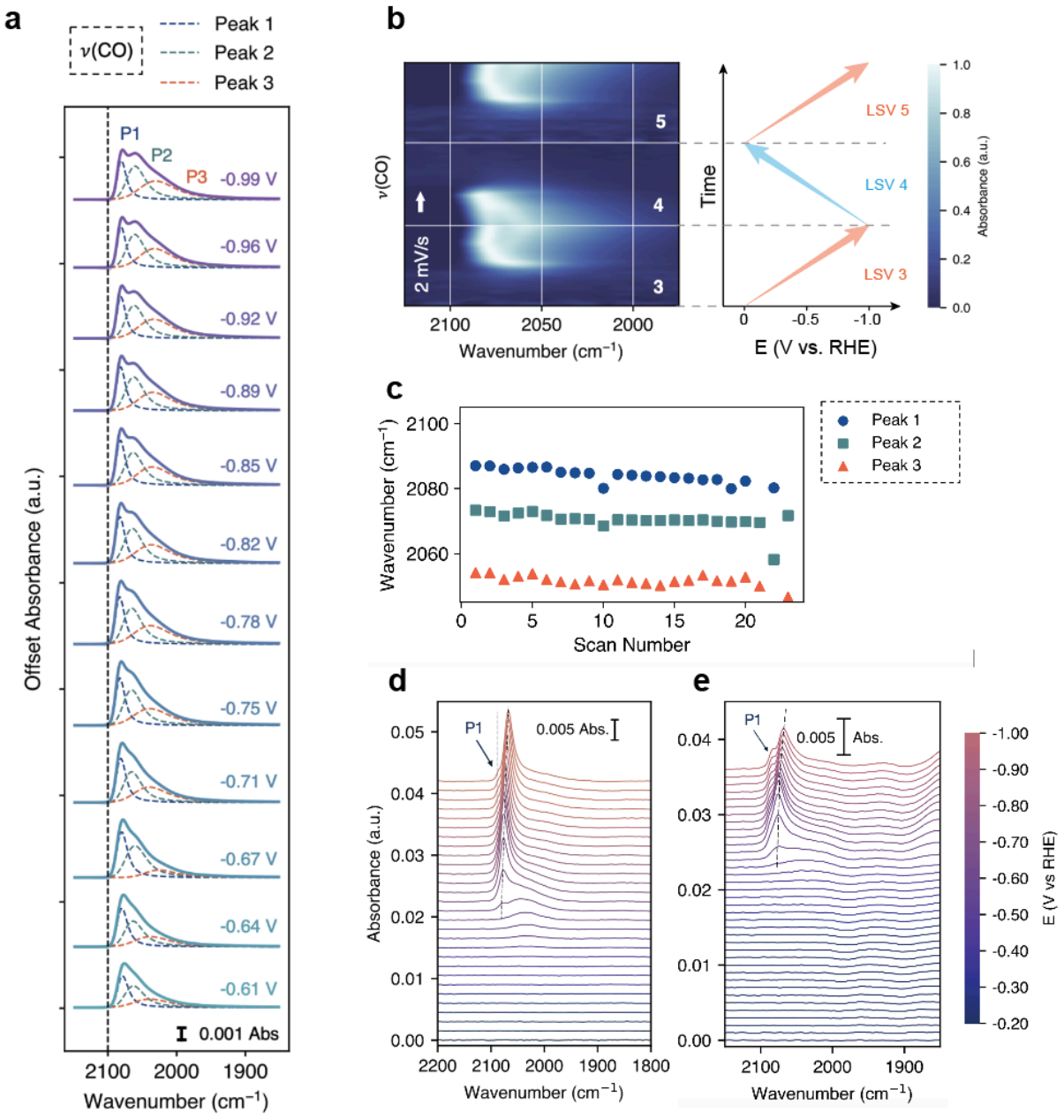

Figure 3.8. Potential-dependent evolution of the C–O stretching region on Cu nanograins probed by *in situ* SEIRAS. a, *In situ* SEIRAS spectra of Cu nanograins collected during LSV scan 3, showing deconvolution of the P1–P3 contributions in the C–O stretching region. Peak fitting was performed using a sum of skewed Voigt functions. **b,** Colormap representation illustrating the reversible emergence of twin peaks in the CO stretching region across LSV scans 3–5. Colormap intensities are normalized, where an intensity of 1.0 corresponds to the maximum CO absorbance of 0.0065 observed during these scans. **c,** Summary of peak-fitting results for the CO stretching region obtained from in situ SEIRAS spectra collected during chronoamperometry (CA) with on-stream gas switching from CO_2 to N_2. The gas switch occurs at scan number 0. **d,e,** *In situ* SEIRAS spectra of electroless-deposited Cu films in CO_2-saturated 0.1 M $KHCO_3$ (**d**) and 0.1 M $CsHCO_3$ (**e**) electrolytes.

SEIRAS experiments performed on electroless deposited Cu films in 0.1 M $KHCO_3$ and 0.1 M $CsHCO_3$ (Figure 3.8d, e) reproduce the characteristic evolution of *CO bands. Notably, the P1 feature is more pronounced in $CsHCO_3$ than in $KHCO_3$ electrolyte, suggesting that the relative prominence of P1 depends on electrolyte cation effects. Owing to its larger ionic radius, Cs^+ is known to produce stronger interfacial electric fields, which can help promote CO_2 adsorption, stabilize *CO and $OCCO^-$ intermediates[194,195]. This will usually lead to enhancements in CO coverage, and a strong promotion of C-C coupling[120,196]. Under Cs^+, bridged CO is observed along with atop CO, unlike in the Cu nanograins where only atop CO was captured. In the context of principal evidence of P1-P3 co-existence on Cu nanograins (in the case of 0.1 M $KHCO_3$), the observed enhancement of P1 in 0.1 M $CsHCO_3$ electrolyte on Cu film is therefore taken as consistent with a broader sensitivity of this feature to interfacial conditions, without implying a direct causal role of the cation. Importantly, this interpretation obviates the need to invoke a distinctive CO adsorption site unique to Cu nanograins. These observations mainly indicate that behavior of the P1–P3 CO stretches arise from interplay of coverage, field effects, and in relation to Cu interfacial chemistry. This is not to dismiss the importance or possibility of 'dual-site' or 'tandem' architectures is well established in heterogeneous catalysis, including in proposed dual site Cu^0-Cu^+ mechanisms,[187,197,198] supported Pt- and Ce- based catalysts[199-201], and other complex interfaces[202,203].

With these insights, several important questions remain open. For instance, what is the molecular-level correlation between the behavior of the P1/P2 components and CO_2 reduction reactivity? How is the emergence and evolution of P1 modulated by local electric-field distortions arising from electrical double-layer (EDL) reorganization, such as interfacial water orientation or cation-specific adsorption or interactions? What precise geometric or electronic metrics create the twin peak phenomena and more generally, how relevant is the motif across various pathways of Cu surface restructuring? While these questions cannot be fully addressed with the present dataset, the observations reported here nevertheless point to broader implications for future SEIRAS studies of nanostructured catalysts. These distinctions underscore how the effects of coverage to skew surface selection rules, rather than adsorption geometry and site structure alone, can govern the spectral signatures observed. As molecular orientation of oscillators is also complicated by the nanograin architecture, what is the operative role, if any, that co-adsorbates elucidated from Raman may have in orientational effects of intermediates in the surface adlayer relative to the local field.

For vibrational modes that can couple via constructive or destructive interference, typically involving identical oscillators with similar frequencies, SEIRAS band intensities should not be interpreted as a direct measurement of adsorbate population or suggesting unique underlying structures. Moreover, the vibrational lineshape itself encodes information about nanoparticle-nanoparticle interactions, evolution state, and double-layer polarization. These encoded parameters may, in principle, be systematically disentangled through carefully designed and systematic SEIRAS protocols if the behavior of P1-P3 across different conditions can be further quantified and grounded. Although further validation is required, this underscores the promise of treating vibrational line shapes not merely as spectral features, but as reporters of a convolution or multitude of orchestrated phenomena, including increasing coverage, co-adsorbate dipole-dipole and non-covalent interactions, electronic coupling, and the strength of interfacial fields can, in sum, contribute to the observables at operating catalytic interfaces.

Section 3.3 reveals how the electrochemical microenvironment of Cu nanograin catalysts evolves under operating conditions and governs the stabilization of CO_2 reduction intermediates. *Operando* SERS and SEIRAS measurements collectively show that the catalytic interface initially forms carbonate-derived surface adlayers at low overpotentials, followed by the emergence of linear atop-bound *CO as the dominant reaction intermediate during CO_2 reduction. These spectroscopic signatures indicate that electrolyte-derived species play a key role in gating the formation of stable *CO at relatively low overpotentials. In addition to *CO, persistent oxygen-containing co-adsorbates (*OH and *O) are detected at the Cu surface, suggesting that catalytic intermediates evolve within a complex adsorbate network rather than on a clean metal surface. Together, these observations highlight the dynamic interplay between electrolyte species, adsorbate coverage, and catalyst surface structure during the early stages of CO_2 reduction.

The nanograin architecture further introduces distinctive interfacial environments that modify the behavior of CO intermediates. *In situ* SEIRAS measurements reveal a multi-component C–O stretching response consisting of three contributions (P1–P3), corresponding to CO adsorbed at different surface environments. The emergence of a characteristic P1/P2 "twin" feature indicates that CO adsorption is strongly influenced by interfacial conditions, including surface coverage, electric-field effects, and interactions with co-adsorbates. Gas-switching experiments and electrolyte-dependent measurements demonstrate that dipole–dipole coupling among *CO molecules contributes to the observed spectral evolution, while the presence of surface oxy-species likely disrupts coherent coupling and modifies vibrational selection rules. These results suggest that the spectral line shapes of CO intermediates reflect not only adsorption geometry but also the broader electrochemical microenvironment.

Collectively, the findings in this section support a view of Cu nanograin catalysts as dynamically evolving interfaces in which surface coverage, co-adsorbate interactions, and interfacial electric fields jointly govern catalytic behavior. Rather than attributing CO_2 reduction activity to isolated adsorption sites alone, the results highlight the importance of nanoscale morphology, local pH, and electric-field confinement in shaping the stability and spectroscopic signatures of reaction intermediates. Within this framework, vibrational spectroscopy provides a powerful means of probing the coupled dynamics of adsorbates and interfacial structure, offering mechanistic insight into how electrochemical microenvironments influence catalytic pathways on Cu nanostructures.

3.4 Insights about electrochemical microenvironments on Cu catalysts

The investigations presented in Sections 3.2 and 3.3 provide complementary perspectives on the electrochemical microenvironment of Cu catalysts under CO_2 reduction conditions. Although these studies examine distinct systems—Cu thin films probed by nano-FTIR and Cu nanograin catalysts studied using SERS and SEIRAS—their combined observations reveal several common interfacial phenomena that appear intrinsic to Cu electrodes. In particular, both studies highlight

the roles of carbonate species, interfacial water organization, and catalyst activation in shaping the electrochemical microenvironment. These elements collectively determine the ionic composition, local electric field, and adsorbate environment at the Cu surface, thereby influencing the stability and interactions of CO_2 reduction intermediates.

A central observation emerging from both studies is the **strong affinity of carbonate species for Cu surfaces**. Nano-FTIR measurements on Cu thin films directly visualize substantial enrichment of bicarbonate ions near Cu nanoparticles relative to adjacent graphene regions, indicating that Cu surfaces locally concentrate electrolyte anions. Importantly, these measurements further reveal that this ion accumulation is spatially heterogeneous on the nanometer scale, with pronounced lateral gradients in carbonate concentration across the interface. Complementary SERS measurements on Cu nanograin catalysts independently detect the dynamics of carbonate-derived surface species during the early stages of electrochemical activation, further confirming that carbonate species participate directly in the Cu interfacial environment. Together, these results suggest that carbonate ions are not merely spectators in bicarbonate electrolytes but represent persistent components of the Cu–electrolyte interface. Their adsorption contributes to the local composition of the electrical double layer and may influence both interfacial electric fields and surface chemistry and morphology. Moreover, the observed enrichment of carbonate species in localized regions near Cu nanostructures suggests that nanoscale morphology can strongly modulate the interfacial electrolyte environment.

The importance of catalyst activation becomes evident when considering how the Cu interface evolves from its pristine state to the active catalytic surface. Both nano-FTIR and SERS measurements indicate that the earliest stages of electrochemical operation involve substantial transformations of the Cu surface. In the thin-film system, reduction of Cu_2O and subsequent nanoparticle formation are accompanied by dramatic redistribution of electrolyte ions and reorganization of interfacial water. In the nanograin system, carbonate-derived surface species initially occupy the interface and gradually give way to adsorbed CO intermediates as the potential becomes more negative. These observations emphasize that **the catalytic microenvironment is largely established during the activation process itself**. Structural transformations such as oxide reduction and surface reconstruction occur simultaneously with carbonate desorption and solvent reorganization, producing the complex interfacial environment in which catalysis proceeds. Consequently, **understanding the microenvironment of an operating Cu catalyst requires consideration not only of the steady-state interface but also of the pathway through which the catalyst evolves during activation**.

The restructuring of the Cu surface is closely coupled to changes in interfacial water structure. Nano-FTIR measurements reveal that the hydrogen-bond network of water near the interface undergoes significant reorganization as the electrode transitions from cuprous oxide to metallic Cu under cathodic bias. This reorganization alters both the orientation and hydrogen-bonding environment of interfacial water molecules, thereby modifying the dielectric properties and electric-field screening within the electrical double layer. Similar to the carbonate distribution, the structure of interfacial water is also spatially heterogeneous at the nanoscale, reflecting the strong influence of local surface morphology and ion accumulation on solvent organization. These observations highlight that the electrochemical microenvironment emerges from the coupled

arrangement of electrolyte ions and water molecules, which together define the interfacial environment experienced by catalytic intermediates.

Within this dynamically evolving microenvironment, the behavior of CO intermediates provides an important probe of interfacial interactions. SEIRAS measurements reveal characteristic features in the CO stretching region, including the appearance of the P1/P2 twin modes, indicating that the vibrational response of adsorbed CO is strongly influenced by its surrounding environment. Rather than reflecting adsorption on several distinct metal sites, these spectral signatures suggest that CO intermediates experience substantial interactions with neighboring species and the surrounding interfacial field. Consistent with this interpretation, SERS measurements reveal the presence of persistent co-adsorbates such as oxygen-containing species at the Cu surface. These co-adsorbates indicate that catalytic intermediates reside within a crowded adsorbate layer in which multiple species coexist and interact. Such environments can influence the local electronic structure of surface Cu atoms, modify solvent orientation and ion distribution, and potentially facilitate surface restructuring under reaction conditions. As a result, the **stabilization and reactivity of intermediates on Cu catalysts cannot be understood solely in terms of isolated adsorption geometries but must instead be considered within the broader context of a dynamically evolving adsorbate ensemble**.

Despite these insights, the relationship between these interfacial phenomena and catalytic performance remains only partially resolved. In particular, while carbonate adsorption, nanoscale ion accumulation, water restructuring, and adsorbate crowding clearly shape the Cu microenvironment, their direct connection to the unusually low overpotential CO_2 reduction reported for certain Cu systems remains an open question. Carbonate species and co-adsorbates may influence local electric fields, interacts with key intermediates, or alter proton-coupled reaction pathways; however, disentangling these contributions under operating conditions remains challenging. Addressing these questions will require further experimental and theoretical efforts capable of resolving the coupled evolution of catalyst structure, electrolyte organization, and adsorbate interactions during catalysis.

Taken together, the results of this chapter support a picture of Cu catalysts as dynamically evolving electrochemical interfaces in which surface reconstruction, electrolyte adsorption, water structure, and adsorbate interactions are intrinsically coupled. Carbonate species emerge as a particularly important component of this environment, influencing both the early activation process and the steady-state interfacial composition. More broadly, these findings emphasize that the microenvironment governing CO_2 reduction on Cu cannot be understood solely from the properties of the final catalytic surface. Instead, it reflects a history-dependent interface shaped by the activation pathway, nanoscale heterogeneity, and evolving adsorbate coverage during catalysis. Understanding and controlling these coupled interfacial processes will therefore be essential for establishing clearer connections between electrochemical microenvironments and catalytic performance in Cu-based CO_2 reduction systems.

Chapter 4 Summary and Outlook

4.1 Summary of key findings

Electrochemical conversion of carbon dioxide provides a promising strategy for transforming renewable electricity into chemical fuels and feedstocks while mitigating anthropogenic carbon emissions. However, a major limitation of CO_2 electroreduction is the large overpotential typically required to activate the thermodynamically stable CO_2 molecule or to couple surface-bound intermediates. Conventional catalyst design strategies have largely focused on tuning the intrinsic properties of catalytic active sites, such as surface composition, crystallographic facets, or electronic structure. While these approaches have yielded important advances, they often overlook the critical role of the electrochemical microenvironment at the catalyst–electrolyte interface.

As discussed in Chapter 1, electrochemical reactions occur within complex interfacial environments where ions, solvent molecules, and surface modifiers collectively influence reaction energetics and kinetics. These interfacial components determine local electric fields, solvation structures, and the stabilization of reactive intermediates. Consequently, the electrochemical microenvironment can strongly affect the activation barriers of elementary reaction steps and ultimately control catalytic performance. Despite its importance, the dynamic and heterogeneous nature of electrochemical interfaces has made direct experimental characterization under operating conditions challenging.

This thesis addresses this challenge by combining a suite of *in situ* and *operando* spectroscopic techniques with theoretical analysis to directly probe the structure and dynamics of electrochemical microenvironments during CO_2R. Two representative catalytic systems were investigated to illustrate distinct aspects of microenvironmental control: ligand-confined nanoparticle catalysts and nanostructured copper catalysts. Together, these studies reveal how interfacial architectures, ion distributions, and solvent structures collectively govern catalytic activity and reaction pathways.

The first major focus of this work, presented in Chapter 2, is the discovery and mechanistic understanding of the nanoparticle-ordered ligand interlayer (NOLI) catalytic architecture. In these systems, metal nanoparticles are initially capped with organic ligands that dynamically reorganize during electrochemical operation. Using nanometer-resolved *in situ* nano-FTIR spectroscopy, this work directly visualizes ligand dynamics under applied electrochemical bias. The measurements reveal that increasing cathodic potential induces progressive ligand detachment from the nanoparticle surface while maintaining a confined ligand scaffold near the catalyst. This process generates a unique interfacial architecture consisting of a metallic nanoparticle core, a confined aqueous interlayer, and an outer ligand framework.

The ligand-defined interlayer creates a distinct electrochemical microenvironment that differs fundamentally from conventional metal–electrolyte interfaces. The confined region between the nanoparticle surface and the ligand scaffold promotes the accumulation of electrolyte cations while simultaneously restricting the local water network. As a result, ions entering this region experience partial desolvation and enhanced interactions with surface intermediates. Through a combination of *in situ* vibrational spectroscopy and X-ray absorption spectroscopy, this work demonstrates that

the NOLI microenvironment facilitates stabilization of key intermediates involved in CO_2 activation.

A central mechanistic insight from Chapter 2 is that cation desolvation plays a critical role in enabling low-overpotential CO_2 reduction. *In situ* spectroscopic measurements reveal the presence of partially desolvated cations within the confined ligand layer, which interact directly with adsorbed CO_2 intermediates. Complementary theoretical calculations further show that these cations can stabilize the activated $*CO_2^-$ species, lowering the energy barrier for the initial electron transfer step. This mechanism differs from conventional descriptions in which cations influence CO_2R primarily through long-range electrostatic effects. Instead, the results support a cation-coupled electron transfer mechanism, where partially desolvated cations directly participate in stabilizing reaction intermediates through a partial covalent interaction.

These findings provide a mechanistic explanation for the experimentally observed low-overpotential CO_2 reduction activity of NOLI catalysts. By modulating ion solvation structures and local electric fields, the ligand-defined microenvironment effectively lowers the energetic barrier for CO_2 activation. This work therefore demonstrates that engineering the interfacial microenvironment can provide catalytic advantages beyond those achievable through conventional active-site design.

While Chapter 2 focuses on ligand-defined microenvironments in nanoparticle catalysts, Chapter 3 extends the investigation to nanostructured copper catalysts, which are uniquely capable of producing multi-carbon products from CO_2 electroreduction. Copper catalysts are known to undergo substantial structural and chemical transformations during electrochemical operation, resulting in highly heterogeneous interfaces that strongly influence catalytic behavior. However, the nanoscale structure of the Cu–electrolyte interface under reaction conditions has remained poorly understood.

To address this question, Chapter 3 employs *in situ* nano-FTIR spectroscopy to probe the spatial distribution of electrolyte species and solvent structures near copper surfaces during electrochemical reactions. These measurements reveal pronounced ion enrichment at copper surfaces, with bicarbonate anion concentrations exceeding bulk electrolyte levels by more than an order of magnitude. Importantly, this ion accumulation is spatially heterogeneous, occurring primarily at metallic copper regions formed during the electrochemical reduction of Cu_2O films. In contrast, adjacent inert surfaces show ion concentrations close to bulk values. These results demonstrate that electrochemical interfaces exhibit strong lateral heterogeneity, where ion distributions vary significantly across nanometer length scales.

The measurements also reveal substantial reorganization of interfacial water structures during the electrochemical transformation of copper oxide to metallic copper. Interfacial water evolves from a disrupted hydrogen-bond network on Cu_2O surfaces to a more ordered hydrogen-bonded structure on metallic copper. Because water molecules participate directly in proton transfer and intermediate stabilization, these structural changes can significantly influence reaction kinetics and selectivity during CO_2 reduction.

Further insights into microenvironment–intermediate interactions were obtained from studies of nanostructured Cu catalysts, which uniquely enable the formation of multi-carbon products in CO_2 electroreduction. While Section 3.2 revealed strong nanoscale heterogeneity in ion distributions and water structures at the Cu–electrolyte interface, Section 3.3 further examined how these

interfacial environments influence the formation and evolution of catalytic intermediates. *In situ* SERS and SEIRAS measurements revealed a complex interfacial chemical landscape in which carbonate species, adsorbed CO intermediates, and other surface-bound species coexist and dynamically evolve under reaction conditions. In particular, carbonate and bicarbonate species were found to accumulate at the Cu interface, indicating that electrolyte-derived species play an active role in shaping the local reaction environment. These observations highlight that CO_2 electroreduction on copper occurs within a crowded interfacial region where electrolyte ions, solvent molecules, and adsorbed intermediates interact strongly with one another.

Spectroscopic measurements of CO adsorption further revealed multiple distinct adsorption environments on Cu nanograin catalysts, reflecting the structural heterogeneity of defect-rich copper surfaces. Importantly, the spectral line shapes and frequency shifts of these CO modes were found to evolve systematically with applied potential and interfacial composition, indicating the involvement of dipole–dipole interactions among neighboring CO molecules and their interactions electrolyte species at the interface. These effects highlight that the spectroscopic signatures of intermediates on Cu catalysts reflect not only the properties of isolated adsorption sites but also the collective interactions among adsorbates and electrolyte species within the interfacial microenvironment.

Together with the nanoscale ion mapping results described in Section 3.2, these findings demonstrate that the Cu–electrolyte interface is a highly dynamic and chemically complex microenvironment in which ion accumulation, solvent restructuring, and intermediate interactions occur simultaneously. Rather than acting as isolated surface reactions, CO_2 reduction processes on copper are governed by the interplay between catalyst structure and the surrounding electrochemical environment. Understanding this coupled behavior provides important insights into how microenvironmental factors influence intermediate stabilization and reaction selectivity in multistep electrochemical reactions.

More broadly, this work highlights the importance of directly probing evolution of electrochemical interfaces during the activation process of catalysts and under their steady-state operating conditions. Advanced *in situ* spectroscopic techniques such as nano-FTIR, SEIRAS, and TEY-XAS provide powerful tools for revealing molecular-level processes that are otherwise inaccessible through conventional *ex situ* characterization methods. The insights gained from these studies establish new principles for the design of next-generation electrocatalysts, where engineering the electrochemical microenvironment provides a complementary strategy to traditional catalyst design.

In summary, this thesis demonstrates that rational control of interfacial microenvironments can enable low-overpotential CO_2 electroreduction and reveal new catalytic mechanisms at electrochemical interfaces. These findings provide a framework for understanding how nanoscale interfacial structures influence electrochemical reactions and highlight the broader potential of microenvironment engineering for advancing sustainable energy conversion technologies.

4.2 Outlook

The central theme of this thesis is that electrochemical microenvironments play a decisive role in enabling low-overpotential CO_2 reduction. As demonstrated in the preceding chapters, the catalyst–electrolyte interface is a highly dynamic and structured environment where ligands, electrolyte ions, solvent molecules, and adsorbed intermediates interact to shape catalytic energetics. In the NOLI system investigated in Chapter 2, a ligand-defined interlayer enables partial cation desolvation and promotes a cation-coupled electron transfer mechanism that lowers the activation barrier for CO_2 activation. In the nanostructured Cu catalysts studied in Chapter 3, nanoscale heterogeneity in ion distribution, solvent structure, and co-adsorbate interactions creates complex interfacial environments that govern intermediate stabilization and reaction pathways. These findings collectively demonstrate that catalytic activity and selectivity cannot be understood solely from the intrinsic properties of the catalyst surface but must instead be considered within the broader context of the surrounding electrochemical microenvironment. While these studies provide new insights into how microenvironmental factors influence CO_2 reduction, many fundamental questions remain unresolved. Addressing these questions will require both conceptual advances in understanding interfacial phenomena and the development of new experimental tools capable of probing these complex environments under realistic operating conditions.

4.2.1 Directions to advance microenvironment studies

This thesis has focused on the major components of the electrochemical microenvironment, including ligands, cations, anions, and solvent molecules. Based on their roles in the catalytic reaction, these components can be broadly categorized into two classes. The first class consists of species that **directly participate in elementary reaction steps**, such as cations involved in cation-coupled electron transfer (CCET) processes and protons involved in proton-coupled electron transfer (PCET) reactions. Because these species directly participate in the reaction mechanism, their local abundance, solvation structure, and interfacial configuration strongly influence reaction kinetics and overpotential. For example, in the NOLI catalytic system discussed in Chapter 2, the rate-determining step involves a cation-coupled electron transfer process. In this case, the solvation structure of the cation and its interaction with the CO_2 intermediate provide a direct mechanistic link between electrical double layer structure and catalytic activity. Changes in cation identity, hydration state, or interfacial concentration can therefore significantly alter the activation barrier for CO_2 reduction. Similarly, in the study of CO adsorption on Cu nanograin catalysts, the identity of electrolyte cations was found to influence the spectral line shapes and frequencies of CO intermediates, indicating strong interactions between cations and adsorbed species. These observations suggest that cation–intermediate interactions may be more widespread in electrocatalytic reactions than previously recognized, and that controlling cation solvation structures represents an important strategy for tuning catalytic energetics.

The second class of microenvironmental components consists of species that influence the reaction **indirectly by shaping the interfacial environment**. These components include ligands, surface modifiers, and anions, which may not directly participate in the elementary reaction step but instead modulate local ion distributions, solvent structure, and interfacial electric fields. These effects may be described as **environmental or indirect microenvironment effects,** since they influence the reaction by modifying the conditions under which reactive species operate. The

NOLI system provides a clear example of such environmental control. In this case, the organic ligand layer does not directly participate in the CO_2 reduction reaction but instead forms a confined scaffold that stabilizes partially desolvated cations and lowers local water activity. This interfacial architecture creates conditions that favor the CCET mechanism responsible for low-overpotential CO_2 reduction. Similarly, electrolyte anions often play an important role during the early stages of catalyst activation and surface restructuring. Although these species may not remain directly involved in the catalytic cycle, they can strongly influence the formation of the microenvironment that ultimately governs catalytic behavior. More broadly, many organic modifiers exhibit **dual functionality**, serving both as surface ligands and as active participants in the electrochemical microenvironment. As discussed in Chapter 1, some organic species can interact with cations, alter water activity, or influence proton availability near the catalyst surface. Likewise, electrolyte anions play important roles in buffering interfacial pH and regulating proton transport. These observations highlight the need to consider electrochemical interfaces as integrated systems, where multiple species collectively determine catalytic performance.

Given the central role of cation solvation and water structure in many electrochemical reactions, **direct experimental probing of these interfacial structures remains critically important**. In practice, however, the solvation structure of a cation cannot be studied independently from the surrounding solvent network. For example, cation solvation structures emerge from the interaction between cations and surrounding water molecules, while cation–intermediate interactions often involve partial reorganization of the solvation shell and redistribution of water molecules into the bulk electrolyte. Conversely, the structure and activity of interfacial water depend strongly on cation identity and concentration. These coupled interactions mean that understanding the behavior of one component of the microenvironment often requires simultaneous characterization of several others. To address this challenge, future studies will likely benefit from combining multiple complementary spectroscopic techniques. ***In situ* vibrational spectroscopies**, such as SEIRAS and SERS, provide detailed information about interfacial water structures, adsorbed intermediates, and co-adsorbate interactions. Meanwhile, **element-specific electronic spectroscopies with surface sensitivity**, such as total electron yield X-ray absorption spectroscopy (TEY-XAS), can directly probe changes in electronic structure associated with cation–intermediate interactions. Integrating these approaches can provide a more complete picture of how ions, solvent molecules, and reaction intermediates interact within the electrochemical microenvironment.

Another important direction for future research is the **simultaneous investigation of microenvironmental effects and catalyst surface structure**. Historically, studies of catalyst surfaces and electrolyte effects have often been treated separately. However, increasing evidence suggests that these two aspects are strongly coupled. First, the structure of the electrochemical microenvironment depends sensitively on catalyst morphology, including nanoparticle size, surface facets, and defect density. As demonstrated in Chapters 2 and 3, nanoscale structural heterogeneity can lead to significant variations in local ion concentration and solvent structure across catalyst surfaces. Second, electrolyte species themselves may actively influence catalyst restructuring and the formation of active sites. For example, cations have been shown to facilitate the dissolution and redeposition of surface atoms in certain electrochemical systems, a phenomenon related to cation-assisted cathodic corrosion[204-206]. Although this effect has received limited attention in CO_2 reduction research, it suggests that electrolyte ions may play an important role in the dynamic evolution of catalyst surfaces. Similarly, anions initially adsorbed on copper

surfaces may contribute to structural transformations during oxide reduction and subsequent desorption processes. These observations highlight the need for **operando techniques capable of probing catalyst structure to compensate studies on microenvironment**, such as *in situ* X-ray-based probes and advanced electron microscopy approaches including *operando* 4D-STEM.

Finally, the current understanding of microenvironment effects in CO_2 electroreduction remains largely qualitative. While many studies have described correlations between electrolyte composition and catalytic performance, relatively few have established **quantitative relationships between microenvironmental properties and reaction kinetics**. Developing such relationships will require more rigorous kinetic analysis combined with theoretical modeling. For example, kinetic models could incorporate parameters such as cation solvation energy, interfacial water activity, or electric field strength to quantitatively relate microenvironmental properties to reaction rates. The development of such models would represent an important step toward predictive control of electrocatalytic reactions through rational electrolyte design.

4.2.2 Directions to advance probing capabilities

In addition to improving conceptual understanding of electrochemical microenvironments, significant advances are also needed in experimental techniques for probing these complex interfaces. Although many spectroscopic methods have been successfully applied to CO_2 reduction systems, important limitations remain in terms of sensitivity, temporal resolution, spatial resolution, and compatibility with industrially relevant operating conditions.

One major challenge lies in the **detection of multi-carbon (C_{2^+}) reaction intermediates**. Although CO_2 electroreduction can produce a wide range of products, including ethylene, ethanol, and other C_{2^+} compounds, most experimentally observed surface species to date correspond to C_1 intermediates or electrolyte-derived adsorbates. As a result, the mechanistic pathways leading to carbon–carbon coupling remain highly debated. Detecting C_{2^+} intermediates is challenging for several reasons. These species are typically present at low surface coverage and often exist only transiently during the catalytic cycle. Furthermore, many proposed intermediates consist of multiple C_1 units, which produce vibrational signatures that overlap with those of simpler intermediates. Consequently, isotopic labeling alone is often insufficient for unambiguous identification. Addressing this challenge will require improved spectroelectrochemical platforms with enhanced sensitivity, as well as advanced theoretical simulations capable of accurately predicting vibrational spectra for complex intermediates.

Another important limitation is **time resolution**. Many key intermediates in CO_2 electroreduction form and disappear on timescales of milliseconds to seconds. Conventional vibrational spectroscopic techniques often operate on longer acquisition times, which can obscure transient processes and dynamic changes in the microenvironment. Developing spectroscopic methods with sub-second temporal resolution will therefore be essential for capturing the evolution of reaction intermediates and identifying rate-limiting steps in complex reaction networks.

Spatial resolution also represents an important frontier. Techniques such as SEIRAS and SERS provide excellent chemical sensitivity and interfacial selectivity but typically average signals over

areas several micrometers in diameter. Modern electrocatalysts, however, often consist of nanoscale particles or heterogeneous surfaces where catalytic activity varies significantly across individual sites. As demonstrated in this thesis, microenvironmental properties such as ion concentration and solvent structure can vary substantially over nanometer length scales. Consequently, probing electrochemical interfaces with spatial resolution below the size of individual catalyst particles is increasingly important. Recent developments in tip-enhanced vibrational spectroscopy, including tip-enhanced Raman spectroscopy (TERS) and atomic force microscopy-based infrared techniques such as AFM-IR and nano-FTIR, offer promising routes for overcoming the diffraction limit and achieving nanometer-scale chemical mapping. Early demonstrations of these techniques under electrochemical conditions have shown considerable potential[79,207], but practical applications remain limited by challenges related to electrochemical cell design, bias stability, and mass transport. Continued advances in spectroelectrochemical cell engineering will therefore be critical for enabling high-resolution operando measurements under realistic reaction conditions.

Finally, an important gap exists between the conditions typically used in fundamental spectroscopic studies and those encountered in industrial CO_2 electroreduction systems. Most *in situ* vibrational spectroscopic experiments are performed in H-cell configurations operating at relatively low current densities. In contrast, industrially relevant CO_2 electrolyzers often operate at current densities exceeding hundreds of milliamperes per square centimeter. Under these conditions, the electrochemical microenvironment may differ fundamentally due to changes in local pH, ion concentration gradients, gas evolution, and mass transport limitations. Bridging this gap will require the development of **spectroelectrochemical platforms compatible with high-current reactor architectures**, such as gas diffusion electrodes, flow cells, and membrane electrode assemblies. Such systems would allow direct observation of microenvironmental dynamics under commercially relevant conditions and may enable the detection of intermediates associated with downstream reaction pathways.

In summary, advancing the understanding of electrochemical microenvironments in CO_2 reduction will require progress on multiple fronts, including mechanistic studies of interfacial interactions, development of quantitative kinetic models, and the creation of new experimental tools capable of probing complex interfaces with high spatial and temporal resolution. Continued efforts in these areas will not only deepen our understanding of CO_2 electroreduction but may also enable the rational design of electrochemical systems with improved efficiency, selectivity, and scalability.

More broadly, the concept of microenvironment engineering may extend far beyond CO_2 electroreduction and provide a general strategy for controlling electrochemical reactions at solid–liquid interfaces. Many important energy conversion processes—including nitrogen reduction, oxygen reduction, water splitting, and electrochemical fuel synthesis—occur in similarly complex interfacial environments where ions, solvent molecules, and adsorbates interact dynamically with catalyst surfaces. In these systems, controlling the local electrochemical environment may be as important as designing the catalyst itself. Advances in spectroscopic techniques, theoretical modeling, and electrochemical reactor design are beginning to make it possible to observe and manipulate these environments with unprecedented precision. Continued progress in this direction could enable the rational design of catalysts and electrolytes that cooperatively stabilize key intermediates, minimize overpotentials, and steer reaction pathways toward desired products.

Ultimately, integrating catalyst design with deliberate control of the electrochemical microenvironment may open new opportunities for developing highly efficient and scalable electrochemical technologies for sustainable energy conversion.

References

1 Friedlingstein, P. *et al.* Global Carbon Budget 2024. *Earth Syst. Sci. Data* **17**, 965-1039 (2025).

2 International Energy Agency. Global Energy review 2025. (IEA, Paris, 2025).

3 IPCC. in *Climate Change 2023: Synthesis Report Contribution of Working Groups I, II and III to the Sixth Assessment Report of the Intergovernmental Panel on Climate Change* (ed H. Lee and J. Romero Core Writing Team) 35-115 (IPCC, 2023).

4 Hepburn, C. *et al.* The technological and economic prospects for CO_2 utilization and removal. *Nature* **575**, 87-97 (2019).

5 Artz, J. *et al.* Sustainable Conversion of Carbon Dioxide: An Integrated Review of Catalysis and Life Cycle Assessment. *Chemical Reviews* **118**, 434-504 (2018).

6 Nitopi, S. *et al.* Progress and Perspectives of Electrochemical CO_2 Reduction on Copper in Aqueous Electrolyte. *Chemical Reviews* **119**, 7610-7672 (2019).

7 Hori, Y. in *Modern Aspects of Electrochemistry* (eds Constantinos G. Vayenas, Ralph E. White, & Maria E. Gamboa-Aldeco) 89-189 (Springer New York, 2008).

8 Jouny, M., Luc, W. & Jiao, F. General Techno-Economic Analysis of CO_2 Electrolysis Systems. *Industrial & Engineering Chemistry Research* **57**, 2165-2177 (2018).

9 De Luna, P. *et al.* What would it take for renewably powered electrosynthesis to displace petrochemical processes? *Science* **364**, eaav3506 (2019).

10 Zimmermann, H. & Walzl, R. in *Ullmann's Encyclopedia of Industrial Chemistry* (2009).

11 Grasemann, M. & Laurenczy, G. Formic acid as a hydrogen source – recent developments and future trends. *Energy & Environmental Science* **5**, 8171-8181 (2012).

12 Leonzio, G., Hankin, A. & Shah, N. CO_2 electrochemical reduction: A state-of-the-art review with economic and environmental analyses. *Chemical Engineering Research and Design* **208**, 934-955 (2024).

13 Bard, A. J. & Faulkner, L. R. *Electrochemical Methods: Fundamentals and Applications*. (Wiley, 2000).

14 Resasco, J. & Bell, A. T. Electrocatalytic CO_2 Reduction to Fuels: Progress and Opportunities. *Trends in Chemistry* **2**, 825-836 (2020).

15 Hisatomi, T., Kubota, J. & Domen, K. Recent advances in semiconductors for photocatalytic and photoelectrochemical water splitting. *Chemical Society Reviews* **43**, 7520-7535 (2014).

16 Walter, M. G. *et al.* Solar Water Splitting Cells. *Chemical Reviews* **110**, 6446-6473 (2010).

17 Liu, K. *et al.* Electronic Effects Determine the Selectivity of Planar Au–Cu Bimetallic Thin Films for Electrochemical CO_2 Reduction. *ACS Applied Materials & Interfaces* **11**, 16546-16555 (2019).

18 Wang, X. *et al.* Breaking the volcano-plot limits for Pt-based electrocatalysts by selective tuning adsorption of multiple intermediates. *Journal of Materials Chemistry A* **7**, 13635-13640 (2019).

19 Wang, Y. *et al.* Catalyst synthesis under CO_2 electroreduction favours faceting and promotes renewable fuels electrosynthesis. *Nature Catalysis* **3**, 98-106 (2020).

20 Lei, Q. *et al.* Structural evolution and strain generation of derived-Cu catalysts during CO_2 electroreduction. *Nature Communications* **13**, 4857 (2022).

21 Kim, D., Kley, C. S., Li, Y. & Yang, P. Copper nanoparticle ensembles for selective electroreduction of CO_2 to C_2-C_3 products. *Proceedings of the National Academy of Sciences* **114**, 10560-10565 (2017).

22 Jung, Y. *et al.* Understanding Electrochemical CO_2 Reduction Selectivity of Cu Binary Alloys from Electronic Structure Descriptors. *Journal of the American Chemical Society* **147**, 39796-39804 (2025).

23 Li, J. *et al.* MOFs-based single/dual-atom catalysts: atomically active sites engineering for efficient CO_2 reduction. *Chemical Synthesis* **5**, 69 (2025).

24 Qiao, Y. & Seger, B. Recent advances in single crystal and facet dependency of copper electrodes on electrochemical CO_2 reduction. *Current Opinion in Chemical Engineering* **43**, 100999 (2024).

25 Takahashi, I., Koga, O., Hoshi, N. & Hori, Y. Electrochemical reduction of CO_2 at copper single crystal Cu(S)-[n(111)×(111)] and Cu(S)-[n(110)×(100)] electrodes. *Journal of Electroanalytical Chemistry* **533**, 135-143 (2002).

26 Dhakar, S. & Sharma, S. Facet Engineering of Copper for Product Specific CO_2 Electroreduction. *The Journal of Physical Chemistry C* **128**, 4862-4881 (2024).

27 Liu, C. *et al.* Local-strain-induced CO_2 adsorption geometries and electrochemical reduction pathway shift. *National Science Review* **11** (2024).

28 Adit Maark, T. & Nanda, B. R. K. Enhancing CO_2 Electroreduction by Tailoring Strain and Ligand Effects in Bimetallic Copper–Rhodium and Copper–Nickel Heterostructures. *The Journal of Physical Chemistry C* **121**, 4496-4504 (2017).

29 Yang, Y. *et al.* Operando studies reveal active Cu nanograins for CO_2 electroreduction. *Nature* **614**, 262-269 (2023).

30 Li, Y. *et al.* Electrochemically scrambled nanocrystals are catalytically active for CO_2-to-multicarbons. *Proceedings of the National Academy of Sciences* **117**, 9194-9201 (2020).

31 Gao, T. *et al.* Cation Exchange-Driven Grain Boundary-Rich Nanorings as Efficient CO_2 Reduction Electrocatalysts. *Angewandte Chemie International Edition* **64**, e202510973 (2025).

32 Wang, J. *et al.* Emerging frontiers of high-entropy materials for catalytic CO_2 reduction. *Inorganic Chemistry Frontiers* **13**, 2235-2266 (2026).

33 Xiao, L., Wang, Z. & Guan, J. Optimization strategies of high-entropy alloys for electrocatalytic applications. *Chemical Science* **14**, 12850-12868 (2023).

34 Sun, J. *et al.* Deciphering the structure–activity–selectivity relationship of high-entropy alloys for CO_2 reduction via interpretable machine learning. *Chemical Science* **16**, 21825-21835 (2025).

35 Scarpa, D. & Sarno, M. Single-Atom Catalysts for the Electro-Reduction of CO_2 to Syngas with a Tunable CO/H_2 Ratio: A Review. *Catalysts* **12**, 275 (2022).

36 Roth-Zawadzki, A. M., Nielsen, A. J., Tankard, R. E. & Kibsgaard, J. Dual and Triple Atom Electrocatalysts for Energy Conversion (CO_2RR, NRR, ORR, OER, and HER): Synthesis, Characterization, and Activity Evaluation. *ACS Catalysis* **14**, 1121-1145 (2024).

37 He, M., Jiang, C.-H., Yan, H.-M., Wang, G. & Wang, Y.-G. Unraveling the C–C Coupling Mechanism on Dual-Atom Catalysts for CO_2/CO Reduction Reaction: The Critical Role of CO Hydrogenation. *The Journal of Physical Chemistry Letters* **16**, 324-332 (2025).

38 Iyengar, P., Kolb, M. J., Pankhurst, J., Calle-Vallejo, F. & Buonsanti, R. Theory-Guided Enhancement of CO_2 Reduction to Ethanol on Ag–Cu Tandem Catalysts via Particle-Size Effects. *ACS Catalysis* **11**, 13330-13336 (2021).

39 Kuhl, K. P., Cave, E. R., Abram, D. N. & Jaramillo, T. F. New insights into the electrochemical reduction of carbon dioxide on metallic copper surfaces. *Energy & Environmental Science* **5**, 7050-7059 (2012).

40 Wen, C. F. *et al.* Highly Ethylene-Selective Electrocatalytic CO_2 Reduction Enabled by Isolated Cu−S Motifs in Metal–Organic Framework Based Precatalysts. *Angewandte Chemie International Edition* **61**, e202111700 (2022).

41 Albertini, P. P. *et al.* Active Sites under Electronic Effect Are More Sensitive to Microenvironment in CO_2 Electroreduction. *Journal of the American Chemical Society* **147**, 25517-25526 (2025).

42 Morales-Guio, C. G. *et al.* Improved CO_2 reduction activity towards C_{2+} alcohols on a tandem gold on copper electrocatalyst. *Nature Catalysis* **1**, 764-771 (2018).

43 Ren, D. *et al.* Selective Electrochemical Reduction of Carbon Dioxide to Ethylene and Ethanol on Copper(I) Oxide Catalysts. *ACS Catalysis* **5**, 2814-2821 (2015).

44 Nguyen, K.-L. C. *et al.* The Influence of Mesoscopic Surface Structure on the Electrocatalytic Selectivity of CO_2 Reduction with UHV-Prepared Cu(111) Single Crystals. *ACS Energy Letters* **9**, 644-652 (2024).

45 Yu, S., Louisia, S. & Yang, P. The Interactive Dynamics of Nanocatalyst Structure and Microenvironment during Electrochemical CO_2 Conversion. *JACS Au* **2**, 562-572 (2022).

46 Ringe, S. *et al.* Understanding cation effects in electrochemical CO_2 reduction. *Energy & Environmental Science* **12**, 3001-3014 (2019).

47 Wang, Y. *et al.* Molecular Modification Strategies for Enhancing CO_2 Electroreduction. *Molecules* **30**, 3038 (2025).

48 Chen, J. *et al.* Selective and stable CO_2 electroreduction at high rates via control of local H_2O/CO_2 ratio. *Nature Communications* **15**, 5893 (2024).

49 Li, F. *et al.* Molecular tuning of CO_2-to-ethylene conversion. *Nature* **577**, 509-513 (2020).

50 Chen, X. *et al.* Electrochemical CO_2-to-ethylene conversion on polyamine-incorporated Cu electrodes. *Nature Catalysis* **4**, 20-27 (2021).

51 Fan, J. *et al.* Immobilized Tetraalkylammonium Cations Enable Metal-free CO_2 Electroreduction in Acid and Pure Water. *Angewandte Chemie International Edition* **63**, e202317828 (2024).

52 Fan, M. *et al.* Cationic-group-functionalized electrocatalysts enable stable acidic CO_2 electrolysis. *Nature Catalysis* **6**, 763-772 (2023).

53 Hsu, Y.-S., Rathnayake, S. T. & Waegele, M. M. Cation effects in hydrogen evolution and CO_2-to-CO conversion: A critical perspective. *The Journal of Chemical Physics* **160** (2024).

54 Shin, S.-J. *et al.* A unifying mechanism for cation effect modulating C_1 and C_2 productions from CO_2 electroreduction. *Nature Communications* **13**, 5482 (2022).

55 Xu, Y., Zhao, K., Chang, X. & Xu, B. Emerging roles of cations in electrocatalytic reduction of CO_2 and CO. *Nature Energy* **11**, 387-399 (2026).

56 Monteiro, M. C. O. *et al.* Absence of CO_2 electroreduction on copper, gold and silver electrodes without metal cations in solution. *Nature Catalysis* **4**, 654-662 (2021).

57 Zhang, Z.-M. *et al.* Probing electrolyte effects on cation-enhanced CO_2 reduction on copper in acidic media. *Nature Catalysis* **7**, 807-817 (2024).

58 Singh, M. R., Kwon, Y., Lum, Y., Ager, J. W., III & Bell, A. T. Hydrolysis of Electrolyte Cations Enhances the Electrochemical Reduction of CO_2 over Ag and Cu. *Journal of the American Chemical Society* **138**, 13006-13012 (2016).

59 Ayemoba, O. & Cuesta, A. Spectroscopic Evidence of Size-Dependent Buffering of Interfacial pH by Cation Hydrolysis during CO_2 Electroreduction. *ACS Applied Materials & Interfaces* **9**, 27377-27382 (2017).

60 Song, Y. *et al.* Efficient CO_2-to-methanol electrocatalysis in acidic media via microenvironment-tuned cobalt phthalocyanine. *Nature Nanotechnology* **21**, 78-86 (2026).

61 Zhang, Q. *et al.* A covalent molecular design enabling efficient CO_2 reduction in strong acids. *Nature Synthesis* **3**, 1231-1242 (2024).

62 Monteiro, M. C. O., Dattila, F., López, N. & Koper, M. T. M. The Role of Cation Acidity on the Competition between Hydrogen Evolution and CO_2 Reduction on Gold Electrodes. *Journal of the American Chemical Society* **144**, 1589-1602 (2022).

63 Ji, S. G. *et al.* Alkali metal cations act as homogeneous cocatalysts for the oxygen reduction reaction in aqueous electrolytes. *Nature Catalysis* **7**, 1330-1338 (2024).

64 Xu, Y., Qiu, Y., Chang, X., Xiao, H. & Xu, B. Revealing the impact of microenvironment on gold-catalysed CO_2 electroreduction via Marcus–Hush–Chidsey kinetics. *Nature Chemistry* **18**, 544-551 (2026).

65 Zhang, H., Raciti, D. & Hall, A. S. Disordered interfacial H_2O promotes electrochemical C–C coupling. *Nature Chemistry* **17**, 1161-1168 (2025).

66 Yu, S. *et al.* CO_2-to-methanol electroconversion on a molecular cobalt catalyst facilitated by acidic cations. *Nature Catalysis* **7**, 1000-1009 (2024).

67 Hall, A. S. & Raciti, D. The role of interfacial water in promoting C–C coupling during CO_2 electroreduction. *Current Opinion in Electrochemistry* **52**, 101722 (2025).

68 Deng, B., Huang, M., Zhao, X., Mou, S. & Dong, F. Interfacial Electrolyte Effects on Electrocatalytic CO_2 Reduction. *ACS Catalysis* **12**, 331-362 (2022).

69 Zhao, Y. *et al.* In Situ Raman Spectroscopy Reveals the Multifunctional Role of Interfacial Water in CO_2-to-C_2 Electroreduction on Cu(hkl) Surfaces. *Journal of the American Chemical Society* **147**, 30230-30238 (2025).

70 Liu, Q. & Yang, W. Resolving non-covalent interactions between surface hydroxyl on Cu and interfacial water in alkaline CO electroreduction. *Nature Catalysis* **8**, 843-852 (2025).

71 Yang, Y. *et al.* Decoupling Product Selectivity in Electrocatalytic CO_2 Reduction by Steering the Interfacial Water Structure. *Journal of the American Chemical Society* **148**, 11284-11295 (2026).

72 Zhang, H., Gao, J., Raciti, D. & Hall, A. S. Promoting Cu-catalysed CO_2 electroreduction to multicarbon products by tuning the activity of H_2O. *Nature Catalysis* **6**, 807-817 (2023).

73 Zhang, J., Zhang, Z., Chen, T., Zhang, J. & Zhang, Y. Electrolyte Effect on Electrocatalytic CO_2 Reduction. *Nanomaterials* **15**, 648 (2025).

74 Wang, J. *et al.* Customizing CO_2 Electroreduction by Pulse-Induced Anion Enrichment. *Journal of the American Chemical Society* **145**, 26213-26221 (2023).

75 Yoo, J. M., Ingenmey, J., Salanne, M. & Lukatskaya, M. R. Anion Effect in Electrochemical CO_2 Reduction: From Spectators to Orchestrators. *Journal of the American Chemical Society* **146**, 31768-31777 (2024).

76 Garg, S. *et al.* Understanding the Effects of Anion Interactions with Ag Electrodes on Electrochemical CO_2 Reduction in Choline Halide Electrolytes. *ChemSusChem* **14**, 2601-2611 (2021).

77 Chen, C. S. *et al.* Stable and selective electrochemical reduction of carbon dioxide to ethylene on copper mesocrystals. *Catalysis Science & Technology* **5**, 161-168 (2015).

78 Roberts, F. S., Kuhl, K. P. & Nilsson, A. High Selectivity for Ethylene from Carbon Dioxide Reduction over Copper Nanocube Electrocatalysts. *Angewandte Chemie International Edition* **54**, 5179-5182 (2015).

79 Shan, Y. *et al.* Nanometre-resolved observation of electrochemical microenvironment formation at the nanoparticle–ligand interface. *Nature Catalysis* **7**, 422-431 (2024).

80 Kim, D. *et al.* Selective CO_2 electrocatalysis at the pseudocapacitive nanoparticle/ordered-ligand interlayer. *Nature Energy* **5**, 1032-1042 (2020).

81 Yu, S. *et al.* Nanoparticle Assembly Induced Ligand Interactions for Enhanced Electrocatalytic CO_2 Conversion. *Journal of the American Chemical Society* **143**, 19919-19927 (2021).

82 Bechtel, H. A., Johnson, S. C., Khatib, O., Muller, E. A. & Raschke, M. B. Synchrotron infrared nano-spectroscopy and -imaging. *Surf. Sci. Rep.* **75**, 100493 (2020).

83 Wu, C.-Y. *et al.* High-spatial-resolution mapping of catalytic reactions on single particles. *Nature* **541**, 511-515 (2017).

84 Bechtel, H. A., Muller, E. A., Olmon, R. L., Martin, M. C. & Raschke, M. B. Ultrabroadband infrared nanospectroscopic imaging. *Proceedings of the National Academy of Sciences* **111**, 7191-7196 (2014).

85 Muller, E. A., Pollard, B., Bechtel, H. A., Van Blerkom, P. & Raschke, M. B. Infrared vibrational nano-crystallography and nano-imaging. *Sci. Adv.* **2** (2016).

86 Amenabar, I. *et al.* Structural analysis and mapping of individual protein complexes by infrared nanospectroscopy. *Nat. Commun.* **4** (2013).

87 Zhao, X. *et al. In vitro* investigation of protein assembly by combined microscopy and infrared spectroscopy at the nanometer scale. *Proc. Natl Acad. Sci. USA* **119**, e2200019119 (2022).

88 Lu, Y.-H. *et al.* Ultrathin Free-Standing Oxide Membranes for Electron and Photon Spectroscopy Studies of Solid–Gas and Solid–Liquid Interfaces. *Nano Lett.* **20**, 6364-6371 (2020).

89 Lu, Y.-H. *et al.* Infrared Nanospectroscopy at the Graphene–Electrolyte Interface. *Nano Lett.* **19**, 5388-5393 (2019).

90 He, X., Larson, J. M., Bechtel, H. A. & Kostecki, R. In situ infrared nanospectroscopy of the local processes at the Li/polymer electrolyte interface. *Nat. Commun.* **13**, 1398 (2022).

91 Zenobi, M. C., Luengo, C. V., Avena, M. J. & Rueda, E. H. An ATR-FTIR study of different phosphonic acids in aqueous solution. *Spectrochim Acta A Mol Biomol Spectrosc* **70**, 270-276 (2008).

92 Luschtinetz, R., Seifert, G., Jaehne, E. & Adler, H.-J. P. Infrared Spectra of Alkylphosphonic Acid Bound to Aluminium Surfaces. *Macromol. Symp.* **254**, 248-253 (2007).

93 Geldof, D. *et al.* Binding modes of phosphonic acid derivatives adsorbed on TiO_2 surfaces: Assignments of experimental IR and NMR spectra based on DFT/PBC calculations. *Surf. Sci.* **655**, 31-38 (2017).

94 Lee, J. T., Hati, S., Fahey, M. M., Zaleski, J. M. & Sardar, R. Surface-Ligand-Controlled Enhancement of Carrier Density in Plasmonic Tungsten Oxide Nanocrystals:

Spectroscopic Observation of Trap-State Passivation via Multidentate Metal Phosphonate Bonding. *Chem. Mater.* **34**, 3053-3066 (2022).

95 Klähn, M. *et al.* IR Spectra of Phosphate Ions in Aqueous Solution: Predictions of a DFT/MM Approach Compared with Observations. *J. Phys. Chem. A* **108**, 6186-6194 (2004).

96 Skibinski, E. S., DeBenedetti, W. J. I. & Hines, M. A. Solution Deposition of Phenylphosphinic Acid Leads to Highly Ordered, Covalently Bound Monolayers on TiO_2 (110) Without Annealing. *J. Phys. Chem. C* **121**, 14213-14221 (2017).

97 Egerton, R. F. Radiation damage to organic and inorganic specimens in the TEM. *Micron* **119**, 72-87 (2019).

98 Leijten, Z. J. W. A., Keizer, A. D. A., de With, G. & Friedrich, H. Quantitative Analysis of Electron Beam Damage in Organic Thin Films. *J. Phys. Chem. C* **121**, 10552-10561 (2017).

99 Lackey, H. E., Nelson, G. L., Lines, A. M. & Bryan, S. A. Reimagining pH Measurement: Utilizing Raman Spectroscopy for Enhanced Accuracy in Phosphoric Acid Systems. *Anal. Chem.* **92**, 5882-5889 (2020).

100 Belding, L. *et al.* Conformation, and Charge Tunneling through Molecules in SAMs. *J. Am. Chem. Soc.* **143**, 3481-3493 (2021).

101 Bodo, E. *et al.* Interaction of a long alkyl chain protic ionic liquid and water. *Chem. Phys.* **140** (2014).

102 Lütgens, M., Chatzipapadopoulos, S. & Lochbrunner, S. Ultrafast CARS with Improved Spectral Resolution. *EPJ Web Conf* **41**, 05007 (2013).

103 Shan, W., Liu, R., Zhao, H. & Liu, J. Bicarbonate Rebalances the *COOH/*OCO^- Dual Pathways in CO_2 Electrocatalytic Reduction: In Situ Surface-Enhanced Raman Spectroscopic Evidence. *J. Phys. Chem. Lett.* **13**, 7296-7305 (2022).

104 Goldie, S. J., Bush, S., Cumming, J. A. & Coleman, K. S. A Statistical Approach to Raman Analysis of Graphene-Related Materials: Implications for Quality Control. *ACS Appl. Nano Mater.* **3**, 11229-11239 (2020).

105 Corson, E. R. *et al.* In Situ ATR–SEIRAS of Carbon Dioxide Reduction at a Plasmonic Silver Cathode. *Journal of the American Chemical Society* **142**, 11750-11762 (2020).

106 Oda, I., Ogasawara, H. & Ito, M. Carbon Monoxide Adsorption on Copper and Silver Electrodes during Carbon Dioxide Electroreduction Studied by Infrared Reflection Absorption Spectroscopy and Surface-Enhanced Raman Spectroscopy. *Langmuir* **12**, 1094-1097 (1996).

107 Ye, K. *et al.* Molecular level insights on the pulsed electrochemical CO_2 reduction. *Nature Communications* **15**, 9781 (2024).

108 Müslehiddinoğlu, J. & Vannice, M. A. CO adsorption on supported and promoted Ag epoxidation catalysts. *Journal of Catalysis* **213**, 305-320 (2003).

109 Ertl, G., Neumann, M. & Streit, K. M. Chemisorption of CO on the Pt(111) surface. *Surface Science* **64**, 393-410 (1977).

110 Gunasooriya, G. T. K. K. & Saeys, M. CO Adsorption on Pt(111): From Isolated Molecules to Ordered High-Coverage Structures. *ACS Catalysis* **8**, 10225-10233 (2018).

111 Steininger, H., Lehwald, S. & Ibach, H. On the adsorption of CO on Pt(111). *Surface Science* **123**, 264-282 (1982).

112 Cui, Z., Wong, A. J.-W., Janik, M. J. & Co, A. C. Negative Reaction Order for CO during CO2 Electroreduction on Au. *Journal of the American Chemical Society* **146**, 23872-23880 (2024).

113 Moradzaman, M. & Mul, G. Infrared Analysis of Interfacial Phenomena during Electrochemical Reduction of CO_2 over Polycrystalline Copper Electrodes. *ACS Catalysis* **10**, 8049-8057 (2020).

114 Miki, A., Ye, S. & Osawa, M. Surface-enhanced IR absorption on platinum nanoparticles: an application to real-time monitoring of electrocatalytic reactions. *Chemical Communications*, 1500-1501 (2002).

115 Zhu, S., Jiang, B., Cai, W.-B. & Shao, M. Direct Observation on Reaction Intermediates and the Role of Bicarbonate Anions in CO_2 Electrochemical Reduction Reaction on Cu Surfaces. *Journal of the American Chemical Society* **139**, 15664-15667 (2017).

116 Wang, Y.-H. *et al. In situ* Raman spectroscopy reveals the structure and dissociation of interfacial water. *Nature* **600**, 81-85 (2021).

117 Delmo, E. P. *et al.* In Situ Infrared Spectroscopic Evidence of Enhanced Electrochemical CO_2 Reduction and C–C Coupling on Oxide-Derived Copper. *Journal of the American Chemical Society* **146**, 1935-1945 (2024).

118 Diesen, E. *et al.* Rationalizing the "anomalous" electrochemical Stark shift of CO at Pt(111) through vibrational spectroscopy and density-functional theory calculations. *Surface Science* **754**, 122694 (2025).

119 Figueiredo, M. C., Hiltrop, D., Sundararaman, R., Schwarz, K. A. & Koper, M. T. M. Absence of diffuse double layer effect on the vibrational properties and oxidation of chemisorbed carbon monoxide on a Pt(111) electrode. *Electrochimica Acta* **281**, 127-132 (2018).

120 Gunathunge, C. M., Ovalle, V. J. & Waegele, M. M. Probing promoting effects of alkali cations on the reduction of CO at the aqueous electrolyte/copper interface. *Physical Chemistry Chemical Physics* **19**, 30166-30172 (2017).

121 Timoshenko, J. & Roldan Cuenya, B. In Situ/Operando Electrocatalyst Characterization by X-ray Absorption Spectroscopy. *Chemical Reviews* **121**, 882-961 (2021).

122 Frazer, B. H., Gilbert, B., Sonderegger, B. R. & De Stasio, G. The probing depth of total electron yield in the sub-keV range: TEY-XAS and X-PEEM. *Surface Science* **537**, 161-167 (2003).

123 Velasco-Velez, J.-J. *et al.* The structure of interfacial water on gold electrodes studied by x-ray absorption spectroscopy. *Science* **346**, 831-834 (2014).

124 Frati, F., Hunault, M. O. J. Y. & de Groot, F. M. F. Oxygen K-edge X-ray Absorption Spectra. *Chemical Reviews* **120**, 4056-4110 (2020).

125 Nilsson, A. *et al.* X-ray absorption spectroscopy and X-ray Raman scattering of water and ice; an experimental view. *Journal of Electron Spectroscopy and Related Phenomena* **177**, 99-129 (2010).

126 Guo, J. & Luo, Y. Molecular structure in water and solutions studied by photon-in/photon-out soft X-ray spectroscopy. *Journal of Electron Spectroscopy and Related Phenomena* **177**, 181-191 (2010).

127 Smith, J. W. & Saykally, R. J. Soft X-ray Absorption Spectroscopy of Liquids and Solutions. *Chemical Reviews* **117**, 13909-13934 (2017).

128 Lange, K. M., Hodeck, K. F., Schade, U. & Aziz, E. F. Nature of the Hydrogen Bond of Water in Solvents of Different Polarities. *The Journal of Physical Chemistry B* **114**, 16997-17001 (2010).

129 Nordlund, D. *et al.* Sensitivity of x-ray absorption spectroscopy to hydrogen bond topology. *Physical Review B* **80**, 233404 (2009).

130 Messer, B. M. *et al.* pH Dependence of the Electronic Structure of Glycine. *The Journal of Physical Chemistry B* **109**, 5375-5382 (2005).

131 Wu, C. H. *et al.* Molecular-Scale Structure of Electrode–Electrolyte Interfaces: The Case of Platinum in Aqueous Sulfuric Acid. *Journal of the American Chemical Society* **140**, 16237-16244 (2018).

132 Suzuki, C. *et al.* Evaluation of electronic state of Cs-adsorbed clay minerals by NEXAFS analysis using DFT calculations. *Journal of Physics and Chemistry of Solids* **127**, 169-177 (2019).

133 Minasian, S. G. *et al.* Quantitative Evidence for Lanthanide-Oxygen Orbital Mixing in CeO_2, PrO_2, and TbO_2. *Journal of the American Chemical Society* **139**, 18052-18064 (2017).

134 Falling L, J. M., Zhao X, Girotto G, Altoe V, van Spronsen M, et al. The Anomalous Behavior of Cesium in the Electrical Double Layer: an In-Situ X-ray Spectroscopy Study on Graphene. *ChemRxiv* (2024).

135 Marcus, Y. Effect of ions on the structure of water. *Pure and Applied Chemistry* **82**, 1889-1899 (2010).

136 Yang, D., Zhu, Q. & Han, B. Electroreduction of CO_2 in Ionic Liquid-Based Electrolytes. *The Innovation* **1**, 100016 (2020).

137 Liu, Z. *et al.* Sustainable and Efficient Bicarbonate Electrolysis via Enhanced CO_2 and Cation Availability on a Gas–Water Dual-Permeable Electrode. *Journal of the American Chemical Society* **148**, 2039-2047 (2026).

138 Ruan, S. *et al.* Ionomers modulate the microenvironment in electrocatalytic CO_2 reduction. *Chemical Science* **17**, 96-117 (2026).

139 Kaltenecker, K. J., Gölz, T., Bau, E. & Keilmann, F. Infrared-spectroscopic, dynamic near-field microscopy of living cells and nanoparticles in water. *Sci Rep-Uk* **11**, 1-12 (2021).

140 Valvo, M., Thyr, J. & Edvinsson, T. Defect‐Induced Raman Scattering in Cu_2O Nanostructures and Their Photocatalytic Performance. *ChemElectroChem* **10** (2023).

141 Ni, G. X. *et al.* Nanoscale Infrared Spectroscopy and Imaging of Catalytic Reactions in Cu_2O Crystals. *ACS Photonics* **7**, 576-580 (2020).

142 Shan, Y. *et al.* Nanometre-resolved observation of electrochemical microenvironment formation at the nanoparticle–ligand interface. *Nat Catal*, 1-10 (2024).

143 Zhao, X. *et al.* In vitro investigation of protein assembly by combined microscopy and infrared spectroscopy at the nanometer scale. *Proceedings of the National Academy of Sciences* **119** (2022).

144 Wu, Q., Yang, N., Xiao, M., Wang, W. & Cui, C. Bicarbonate-mediated proton transfer requires cations. *Nat Commun* **15** (2024).

145 Dunwell, M. *et al.* The Central Role of Bicarbonate in the Electrochemical Reduction of Carbon Dioxide on Gold. *J Am Chem Soc* **139**, 3774-3783 (2017).

146 Kaur, H., Rana, B., Tomar, D., Kaur, S. & Jena, K. C. 3-37 (Springer Singapore, 2021).

147 Delmo, E. P. *et al. In Situ* Infrared Spectroscopic Evidence of Enhanced Electrochemical CO_2 Reduction and C–C Coupling on Oxide-Derived Copper. *J Am Chem Soc* **146**, 1935-1945 (2024).

148 Seki, T. *et al.* The Bending Mode of Water: A Powerful Probe for Hydrogen Bond Structure of Aqueous Systems. *The Journal of Physical Chemistry Letters* **11**, 8459-8469 (2020).

149 Yu, C.-C. *et al.* Vibrational couplings and energy transfer pathways of water's bending mode. *Nat Commun* **11**, 5977 (2020).

150 Yang, S. *et al.* Nature of the Electrical Double Layer on Suspended Graphene Electrodes. *J. Am. Chem. Soc.* **144**, 13327-13333 (2022).

151 Skinner, J., Pieniazek, P. & Gruenbaum, S. Vibrational spectroscopy of water at interfaces. *Accounts Chem Res* **45**, 93-100 (2012).

152 Riplinger, C. & Carter, E. A. Cooperative Effects in Water Binding to Cuprous Oxide Surfaces. *The Journal of Physical Chemistry C* **119**, 9311-9323 (2015).

153 Möller, C. & Nilius, N. Water Adsorption on $Cu_2O(111)$ Surfaces: A Scanning Tunneling Microscopy Study. *The Journal of Physical Chemistry C* **121**, 20877-20881 (2017).

154 Herzog, A. *et al.* Operando Raman spectroscopy uncovers hydroxide and CO species enhance ethanol selectivity during pulsed CO_2 electroreduction. *Nature Communications* **15**, 3986 (2024).

155 Zhang, Y. *et al.* Low-coordinated copper facilitates the *CH_2CO affinity at enhanced rectifying interface of Cu/Cu_2O for efficient CO_2-to-multicarbon alcohols conversion. *Nature Communications* **15**, 5172 (2024).

156 Moradzaman, M. & Mul, G. In Situ Raman Study of Potential-Dependent Surface Adsorbed Carbonate, CO, OH, and C Species on Cu Electrodes During Electrochemical Reduction of CO_2. *ChemElectroChem* **8**, 1478-1485 (2021).

157 Kim, J. *et al.* Spatiotemporal active phase evolution for CO_2 electrocatalysis. *Joule* **8**, 3373-3385 (2024).

158 Henckel, D. A. *et al.* Potential Dependence of the Local pH in a CO_2 Reduction Electrolyzer. *ACS Catalysis* **11**, 255-263 (2021).

159 Amirbeigiarab, R. *et al.* Atomic-scale surface restructuring of copper electrodes under CO_2 electroreduction conditions. *Nature Catalysis* **6**, 837-846 (2023).

160 Munz, M., Poon, J., Frandsen, W., Cuenya, B. R. & Kley, C. S. Nanoscale Electron Transfer Variations at Electrocatalyst–Electrolyte Interfaces Resolved by in Situ Conductive Atomic Force Microscopy. *Journal of the American Chemical Society* **145**, 5242-5251 (2023).

161 Yang, Y. *et al.* Operando probing dynamic migration of copper carbonyl during electrocatalytic CO_2 reduction. *Nature Catalysis* **8**, 579-594 (2025).

162 An, H. *et al.* Spatiotemporal Mapping of Local Heterogeneities during Electrochemical Carbon Dioxide Reduction. *JACS Au* **3**, 1890-1901 (2023).

163 Zhan, C. *et al.* Revealing the CO Coverage-Driven C–C Coupling Mechanism for Electrochemical CO_2 Reduction on Cu_2O Nanocubes via Operando Raman Spectroscopy. *ACS Catalysis* **11**, 7694-7701 (2021).

164 Liu, Q. *et al.* Universal Formation, Dynamics, and Reactivities of *CO_{bridge} Accompanying Spontaneous Reconstruction of Cu during Electrochemical CO_2 or CO Reduction. *Journal of the American Chemical Society* **147**, 31497-31508 (2025).

165 Li, J. *et al.* Electrokinetic and in situ spectroscopic investigations of CO electrochemical reduction on copper. *Nature Communications* **12**, 3264 (2021).

166 Ma, H., Ibáñez-Alé, E., You, F., López, N. & Yeo, B. S. Electrochemical Formation of C_{2+} Products Steered by Bridge-Bonded *CO Confined by *OH Domains. *Journal of the American Chemical Society* **146**, 30183-30193 (2024).

167 García de Arquer, F. P. *et al.* CO_2 electrolysis to multicarbon products at activities greater than 1 A cm^{-2}. *Science* **367**, 661-666 (2020).

168 Magnussen, O. M. & Groß, A. Toward an Atomic-Scale Understanding of Electrochemical Interface Structure and Dynamics. *Journal of the American Chemical Society* **141**, 4777-4790 (2019).

169 Rossmeisl, J., Nørskov, J. K., Taylor, C. D., Janik, M. J. & Neurock, M. Calculated Phase Diagrams for the Electrochemical Oxidation and Reduction of Water over Pt(111). *The Journal of Physical Chemistry B* **110**, 21833-21839 (2006).

170 Baldenebro-López, J., Castorena-González, J., Flores-Holguín, N., Almaral-Sánchez, J. & Glossman-Mitnik, D. Computational Molecular Nanoscience Study of the Properties of Copper Complexes for Dye-Sensitized Solar Cells. *International Journal of Molecular Sciences* **13**, 16005-16019 (2012).

171 Chan, K. A few basic concepts in electrochemical carbon dioxide reduction. *Nature Communications* **11**, 5954 (2020).

172 Kok, J., Albertini, P. P., Leemans, J., Buonsanti, R. & Burdyny, T. Overcoming copper stability challenges in CO_2 electrolysis. *Nature Reviews Materials* **10**, 550-563 (2025).

173 Lian, Z., Dattila, F. & López, N. Stability and lifetime of diffusion-trapped oxygen in oxide-derived copper CO_2 reduction electrocatalysts. *Nature Catalysis* **7**, 401-411 (2024).

174 Poberžnik, M. & Kokalj, A. Surprising Lateral Interactions between Negatively Charged Adatoms on Metal Surfaces. *The Journal of Physical Chemistry Letters* **11**, 7122-7126 (2020).

175 Yang, K., Kas, R. & Smith, W. A. In Situ Infrared Spectroscopy Reveals Persistent Alkalinity near Electrode Surfaces during CO_2 Electroreduction. *Journal of the American Chemical Society* **141**, 15891-15900 (2019).

176 Yao, K. *et al.* In situ copper faceting enables efficient CO_2/CO electrolysis. *Nature Communications* **15**, 1749 (2024).

177 Surface-enhanced infrared absorption spectroscopy. *Nature Reviews Methods Primers* **3**, 71 (2023).

178 Wang, Y., Ding, J., Su, C., Shen, Z. & Liu, B. ATR-SEIRAS for Single-Atom Electrocatalysis. *Accounts of Chemical Research* **58**, 2282-2295 (2025).

179 Cuesta, A. ATR-SEIRAS for time-resolved studies of electrode–electrolyte interfaces. *Current Opinion in Electrochemistry* **35**, 101041 (2022).

180 Su, Z.-F., Sun, S.-G., Wu, C.-X. & Cai, Z.-P. Study of anomalous infrared properties of nanomaterials through effective medium theory. *The Journal of Chemical Physics* **129** (2008).

181 Wu, C.-X., Lin, H., Chen, Y.-J., Li, W.-X. & Sun, S.-G. Abnormal IR effects of Pt nanostructured surfaces upon CO chemisorption due to interaction and electron-hole damping. *The Journal of Chemical Physics* **121**, 1553-1556 (2004).

182 Priebe, A., Sinther, M., Fahsold, G. & Pucci, A. The correlation between film thickness and adsorbate line shape in surface enhanced infrared absorption. *The Journal of Chemical Physics* **119**, 4887-4890 (2003).

183 Pilling, M. J. *et al.* Anomalous inverse absorption features in the far-infrared RAIRS spectra of $SnCl_4$ on thin-film SnO_2 surfaces. *The Journal of Chemical Physics* **117**, 6780-6788 (2002).

184 Gebre, S. T. *et al.* Fano Resonance in CO_2 Reduction Catalyst Functionalized Quantum Dots. *Journal of the American Chemical Society* **147**, 10966-10973 (2025).

185 Gunathunge, C. M., Ovalle, V. J., Li, Y., Janik, M. J. & Waegele, M. M. Existence of an Electrochemically Inert CO Population on Cu Electrodes in Alkaline pH. *ACS Catalysis* **8**, 7507-7516 (2018).

186 Gunathunge, C. M. *et al.* Spectroscopic Observation of Reversible Surface Reconstruction of Copper Electrodes under CO_2 Reduction. *The Journal of Physical Chemistry C* **121**, 12337-12344 (2017).

187 Gunathunge, C. M., Li, J., Li, X., Hong, J. J. & Waegele, M. M. Revealing the Predominant Surface Facets of Rough Cu Electrodes under Electrochemical Conditions. *ACS Catalysis* **10**, 6908-6923 (2020).

188 Roiaz, M. *et al.* Roughening of Copper (100) at Elevated CO Pressure: Cu Adatom and Cluster Formation Enable CO Dissociation. *The Journal of Physical Chemistry C* **123**, 8112-8121 (2019).

189 Zhang, D. *et al.* Characterization of CO Adsorbed to Clean and Partially Oxidized Cu(211) and Cu(111). *The Journal of Physical Chemistry C* **127**, 24158-24167 (2023).

190 Matthews, J. E. *et al.* Operando Surface-Enhanced Infrared Spectroscopy Connects Interfacial Dynamics with Reaction Kinetics During Electrochemical CO_2 Reduction on Copper. *ACS Catalysis* **15**, 381-391 (2025).

191 Monai, M. A New Look at Catalyst Surfaces at Work: Introducing Mixed Isotope Operando Infrared Spectroscopy (MIOIRS). *ACS Catalysis* **15**, 1363-1386 (2025).

192 Ortega, A., Huffman, F. M. & Bradshaw, A. M. The adsorption of CO on Pd(100) studied by IR reflection absorption spectroscopy. *Surface Science* **119**, 79-94 (1982).

193 Hollins, P. The influence of surface defects on the infrared spectra of adsorbed species. *Surface Science Reports* **16**, 51-94 (1992).

194 Resasco, J. *et al.* Promoter Effects of Alkali Metal Cations on the Electrochemical Reduction of Carbon Dioxide. *Journal of the American Chemical Society* **139**, 11277-11287 (2017).

195 Resasco, J. A Universal Model of Cation Effects in Electrocatalysis. *JACS Au* **5**, 5253-5266 (2025).

196 Niu, Y., Tao, H., Liu, H., Li, J. & Lian, C. Cation Regulates Adsorption–Desorption Behaviors To Promote Electrochemical CO_2 Reduction Reaction. *ACS Catalysis* **16**, 3903-3913 (2026).

197 Yuan, X. *et al.* Controllable Cu^0-Cu^+ Sites for Electrocatalytic Reduction of Carbon Dioxide. *Angewandte Chemie* **133**, 15472-15475 (2021).

198 Sun, X. *et al.* Oscillatory redox behavior in oxides: Cyclic surface reconstruction and reactivity modulation via the Mars–van Krevelen mechanism. *Proceedings of the National Academy of Sciences* **122**, e2422711122 (2025).

199 Yang, J. *et al.* Formation of hydrided Pt-Ce-H sites in efficient, selective oxidation catalysts. *Science* **388**, 514-519 (2025).

200 Wang, H. *et al.* Migration and aggregation of Pt atoms on metal oxide-supported ceria nanodomes control reverse water gas shift reaction activity. *Communications Chemistry* **6**, 264 (2023).

201 Ding, K. *et al.* Identification of active sites in CO oxidation and water-gas shift over supported Pt catalysts. *Science* **350**, 189-192 (2015).

202 Tian, Z. *et al.* Surface Coordination Engineered Single-Atom Catalysts toward Biomass Tandem Conversion. *ACS Catalysis* **16**, 5520-5531 (2026).

203 Green, I. X., Tang, W., Neurock, M. & Yates, J. T. Spectroscopic Observation of Dual Catalytic Sites During Oxidation of CO on a Au/TiO_2 Catalyst. *Science* **333**, 736-739 (2011).

204 Wang, Y.-Q. *et al.* Alkali Metal Cations Induce Structural Evolution on Au(111) During Cathodic Polarization. *Journal of the American Chemical Society* **146**, 27713-27724 (2024).

205 Li, Z., Wang, L., Sun, L. & Yang, W. Dynamic Cation Enrichment during Pulsed CO_2 Electrolysis and the Cation-Promoted Multicarbon Formation. *Journal of the American Chemical Society* **146**, 23901-23908 (2024).

206 Hersbach, T. J. P. *et al.* Alkali Metal Cation Effects in Structuring Pt, Rh, and Au Surfaces through Cathodic Corrosion. *ACS Applied Materials & Interfaces* **10**, 39363-39379 (2018).

207 Zhu, Q. *et al.* The solvation environment of molecularly dispersed cobalt phthalocyanine determines methanol selectivity during electrocatalytic CO_2 reduction. *Nature Catalysis* **7**, 987-999 (2024).